Forward Muon Detection in H1
and
Hadronic Energy Flow in Deep Inelastic Scattering

Christopher D. Hilton

October 1993

A thesis submitted to the University of Manchester for the degree
of Doctor of Philosophy in the Department of Physics in the
Faculty of Science.

Contents

4

Summary and Conclusion 123

Abstract

The H1 experiment observes collisions between 26.7 GeV electrons and 820 GeV protons which are accelerated in the HERA storage ring at DESY in Hamburg. High energy muons at small angles to the incoming proton direction are detected in the forward muon detector, a drift chamber system incorporating its own toroidal magnet which allows it to make independent momentum measurements. This detector is described and its potential for use in the context of identifying J/ψ mesons via their decay to two muons is assessed using computer simulations. It is shown that the forward muon detector can be used to identify muons in the central tracking detectors of H1.

In the first year of operation, 1992, data corresponding to an integrated luminosity of about 25 nb^{-1} were collected including about 1000 neutral current deep inelastic scattering events. A measurement of the hadronic energy flow seen in H1 for these events is made and compared with monte carlo predictions based on various models of the perturbative QCD processes involved. None is found to satisfactorily reflect the data in the kinematic region of Bjorken x between 10^{-4} and 10^{-3}.

No portion of the work referred to in this thesis has been submitted in support of an application for another degree or qualification of this or any other institute of learning.

Introduction

The observation of collisions between electrons and protons provides information about the structure of the proton and the nature of the force which binds it. Distances down to about 10^{-18} m inside the proton can be probed using the Hadron Electron Ring Accelerator (HERA), the first electron–proton collider. Such a spatial resolution is achieved by virtue of the very high energy, about 50 TeV, which the probing electron has in the rest frame of the target proton, and is an order of magnitude smaller than at previous, fixed target experiments.

HERA is designed to produce head–on collisions between 30 GeV electrons and 820 GeV protons. The particles are accelerated to these energies in two separate beam–pipes contained within the same tunnel which has a circumference of 6.3 km. Only at four points are the counter–circulating beams brought together into a single pipe so that collisions may occur. The particle detector, H1, observes the products of the collisions at one of these points.

A design luminosity of $1.5 \times 10^{31} cm^{-2} s^{-1}$ with protons and electrons of 820 GeV and 30 GeV respectively will yield a total integrated luminosity of about $100 pb^{-1}$ per year at a centre of mass frame energy for collisions of 314 GeV. During the first year of operation, 1992, an integrated luminosity of about $32 nb^{-1}$ was delivered by HERA, equivalent to less than an hour of data collection at the design luminosity but nevertheless enough for some early physics studies. Whilst the protons have been accelerated to the design energy of 820 GeV, the energy of the electrons in 1992 and 1993 has been 26.7 GeV resulting in collisions at a centre of mass frame energy of 296 GeV. During the late summer of 1993 the luminosities achieved have been considerably greater than previously, frequently reaching peak values of about $10^{30} cm^{-2} s^{-1}$. By the end of 1993 an integrated luminosity of about $1 pb^{-1}$ will have been produced by HERA in the H1 interaction region.

This thesis is concerned with the H1 particle detector and its physics. In particular, a detailed study of the forward muon detector of H1 is presented which is based upon computer simulation. This apparatus is designed to detect and measure the momentum of high energy muons at small angles to the direction of the incoming protons. In addition, data taken from collisions in 1992 are used to make an early measurement of the hadronic energy flow in deep inelastic scattering events, utilising the calorimeters and forward and central tracking detectors of H1.

Chapters 1 and 2 provide the necessary background to the above mentioned studies, introducing the physics of electron–proton collisions at HERA and the H1 detector respectively. Chapter 3 is a description of the forward muon detector, including the methods of reconstructing muon tracks from the observed signals in the detector. This precedes an assessment of the potential performance of the forward muon detector in the context of the aspects of physics which it will be used to study, made in chapter 4. The chapter begins with a description of the computer simulation of the detector which is central to the study, and concludes by indicating the rôle that it can play in identifying the J/ψ–meson via its di–muon decay. In chapter 5 a measurement of the hadronic energy distribution in deep inelastic events is presented, which is sensitive to QCD radiative corrections to the basic electroweak process.

Chapter 1

Physics at HERA

Interactions between high energy electrons and protons are understood in terms of the standard model and the quark–parton model. A proton has structure, consisting of partons: quarks and gluons. Its constituents are bound by the strong force, described in quantum chromodynamics (QCD), which is mediated by gluons which couple to themselves and to quarks. Electrons can be viewed here as a source of bosons: photons, Z^0, $W^\pm$, which then probe the structure of the proton by interacting with its constituents.

The nature of the interaction with the proton is governed by the virtuality, Q^2, of the exchange boson; $Q^2 = -q.q$ where q is the 4–momentum of the boson or equivalently the 4–momentum transfer from the electron to the proton. In collisions between electrons at 30 GeV and protons at 820 GeV values of Q^2 up to about $10^5 GeV^2$ can be attained. For interactions in which Q^2 is greater than about $1 GeV^2$ the boson probes a distance smaller than the size of the proton, and interacts with its constituent quarks. At this scale the quarks within the proton appear free, not under the influence of the other proton constituents. In this sense, HERA acts as an electron–quark collider, the proton being the carrier of the quarks. Such interactions are called 'deep inelastic scattering', and studying them reveals much about the structure of the proton and the nature of the strong force. Interactions in which the boson is less virtual (in which case the boson is almost certainly a photon and the interaction is known as a 'photoproduction' event) are viewed somewhat differently. These are long distance interactions which do not, in general, involve coupling to a single quark in the proton. This is explained in more detail below.

The nature of calculations made within the framework of QCD also changes at a virtuality scale of the order of $1 GeV^2$ (equivalently a distance scale of about 1 fm). This is related to the running of the strong coupling constant, α_s, which decreases with increasing Q^2. At higher Q^2 ($> \approx 1 GeV^2$), the strong force coupling becomes weak enough such that the quarks appear free within the proton (asymptotic freedom), as implied in the previous paragraph. Precise calculations based on perturbative expansions in α_s, the strong coupling constant, are possible in this regime. Quantitative calculations at lower virtuality scales are much more difficult; perturbative expansions diverge. In general, phenomenologically inspired models are used to describe interactions (or the parts of interactions) which are not calculable in perturbative QCD. This increase in the strength of the strong force at larger distance scales is presumably related to the 'confinement' of quarks within hadrons.

1.1   Deep Inelastic Scattering

Figure 1.1 represents a deep inelastic scattering (DIS) event in which the incoming lepton and a quark in the proton interact via a mediating virtual boson. The kinematics of such collisions are usually defined in terms of four invariants (referring to the labels of figure 1.1):

$$Q^2 = -q^\mu q_\mu \; , \tag{1.1}$$

the momentum transfer variable or virtuality of the exchange boson;

$$y = \frac{P^\mu q_\mu}{P^\nu k_\nu} \; , \tag{1.2}$$

the fraction of energy taken by the boson from the incoming electron in the proton rest frame;

$$x = \frac{Q^2}{2P^\mu q_\mu} \; , \tag{1.3}$$

the proton momentum fraction of the struck quark in the infinite momentum frame of the proton and at high Q^2;

$$W^2 = P'^\mu P'_\mu \; , \tag{1.4}$$

the invariant mass squared of the hadronic final state.

These four quantities are not independent, being related in particular by the equations
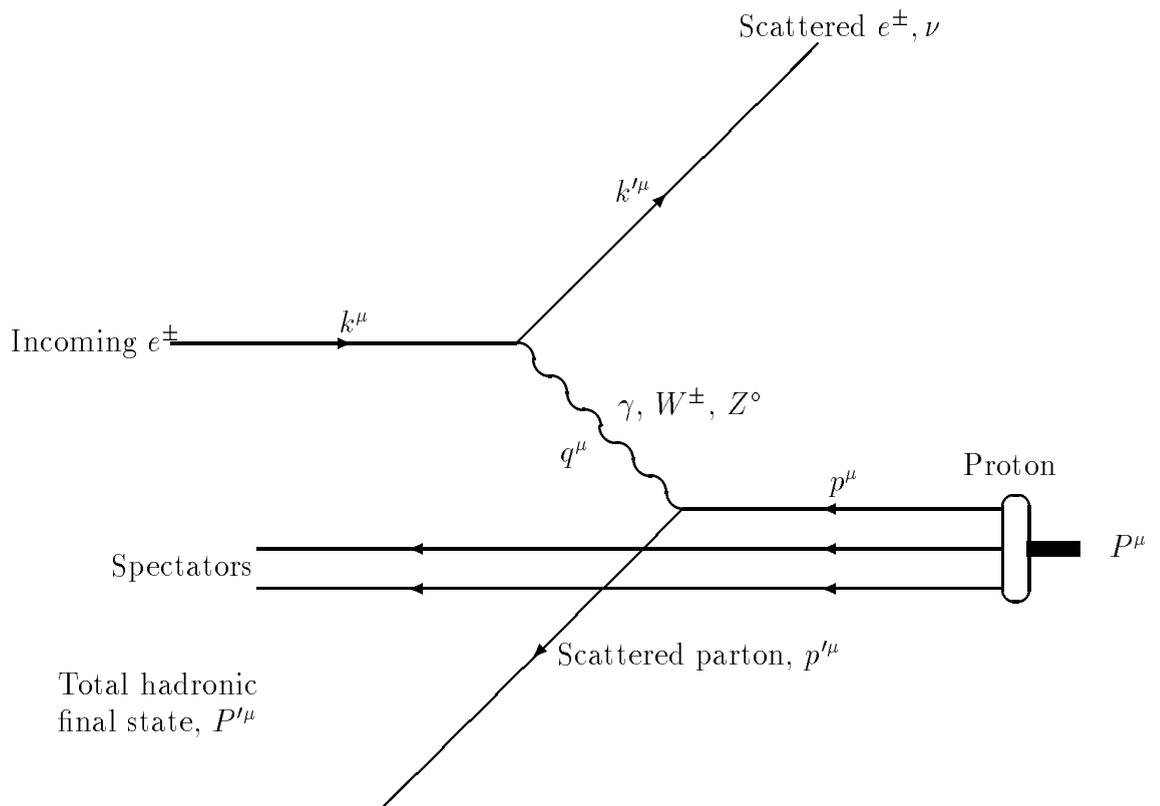
$$x = \frac{Q^2}{Q^2 + W^2} \tag{1.5}$$

Figure 1.1: Representation of a deep inelastic scattering event.

and

$$Q^2 = xys \tag{1.6}$$

where s is centre of mass energy squared of the lepton–proton system. Since the scaling variables x and y are restricted to values between 0 and 1 the maximum attainable value of Q^2 is s, thus it is the high energy available for the lepton–proton collisions which allows very small distance resolution. The kinematic region accessible at HERA is illustrated in figure 1.2, in which the region investigated by previous fixed–target experiments is also shown.

Figure 1.1 indicates the prospect of HERA providing collisions between positrons and protons, and polarised beams are also intended in the future. These will be useful in resolving the quark flavour content of the proton but the following discussion assumes electron–proton collisions.

The differential cross–section for neutral current deep inelastic scattering of electrons off protons is given by

$$\frac{d^2\sigma}{dxdQ^2} = \frac{4\pi\alpha^2}{xQ^4}\left(y^2xF_1(x,Q^2) + (1-y)F_2(x,Q^2) + (y - \frac{y^2}{2})F_3(x,Q^2)\right) \tag{1.7}$$

where α is the fine structure constant [7]. Proton structure is represented by the three structure functions: F_1, F_2 and F_3. The function F_3 is negligible unless Q is of the order of the mass of the Z^0 boson, as is the charged current cross–section since such interactions are mediated by $W^\pm$ bosons. Studies carried out with early H1 data, in particular that reported in chapter 5 of this thesis, have therefore concentrated on lower Q^2 events (generally $Q^2 <\approx 100 GeV^2$) which are assumed to be mediated by a virtual photon.

A measurement by H1 of the F_2 structure function at low x, a kinematic region unavailable to previous experiments, is presented in [8] based on collisions in 1992. Understanding of QCD is tested by comparing this result with predictions. The predictions, which are implemented in Monte Carlo (MC) programs, are attempts to model the content of the proton at Q^2 and x scales previously not attained by experiment by evolving the structure at known scales (higher x and lower Q^2) into the new kinematic region of HERA DIS collisions.

Qualitatively, the shorter distance probe of a high Q^2 photon is able to resolve short lived fluctuations of a quark within a proton. In QCD, the quarks radiate gluons and the gluons radiate gluons and form quark pairs. A long distance probe
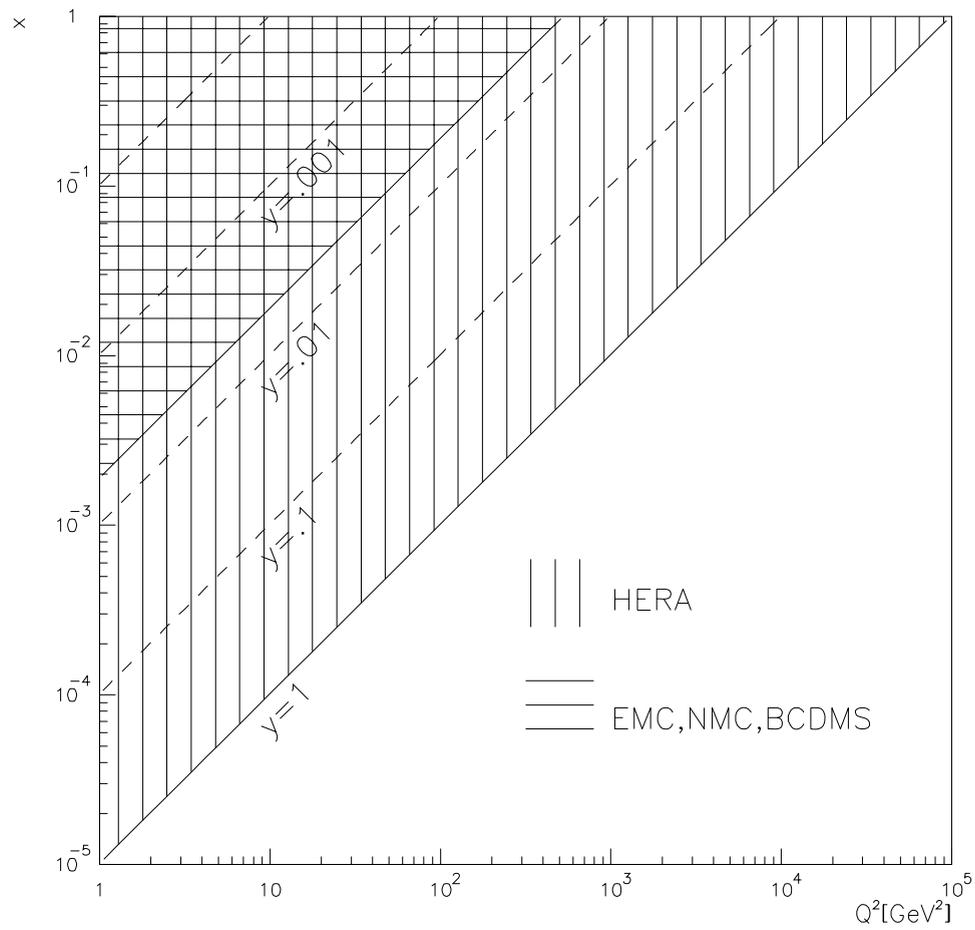
Figure 1.2: Kinematic region accessible at HERA, and that accessible to EMC [1, 2], BCDMS [3, 4] and NMC [5, 6].

does not see these fluctuations but only resolves a valence quark. Hence the structure of the proton appears different at different Q^2 scales — 'scaling' is violated. The proton structure at some starting scale, $Q_0^2 \approx 4 GeV^2$, is taken as a starting point for the evolution process which predicts the structure at a higher Q^2 scale. At the Q_0^2 scale the quark and gluon content is already constrained by experimental information. A parton in the proton becomes more virtual by emitting a further parton. The high–Q^2 probe can pick out a parton which has undergone successive branchings to become highly virtual. Each chain of branching partons can be calculated in the context of perturbative QCD since the evolving parton is assumed to be increasing in virtuality from the starting value of Q_0^2. By summing over all possible chains from Q_0^2 to Q^2 the structure of the proton at Q^2 is known. Similarly the proton structure can be evolved downwards in x.

In practice, the calculations outlined above need to be simplified by making certain approximations. For instance, in evolving in Q^2 a strict ordering of virtualities in the branching chains is assumed. Different predictions for the structure functions arise from different approximations in the evolution calculation, different gluon distributions in the proton at Q_0^2, and different assumptions about the gluon density in the proton as x becomes very small. The derivation of parton densities in the proton is discussed in more detail in [7].

It is clear from the above that predictions of F_2, which directly reflects the quark content of the proton (see, for example [9]), are dependent upon the implementation of perturbative QCD. Thus measurements of F_2 are a direct test of the theory and the understanding of it. The result of [8] is a clear rise in F_2 with decreasing x (figure 1.3), which is a signature of QCD processes occurring within the proton.

The distribution of energy in the hadronic final state of DIS events is also sensitive to different models of QCD radiation. Some of the current models of DIS interactions implement this radiation in the form of chains of parton branchings of the same form that is assumed in structure function evolution. In this picture, a particular DIS event picks out a particular fluctuation (branching chain). The sum of all such fluctuations leads to the evolved parton densities. Measurement of the hadronic final state is therefore a further test of perturbative QCD calculations and is linked to the structure function measurements.

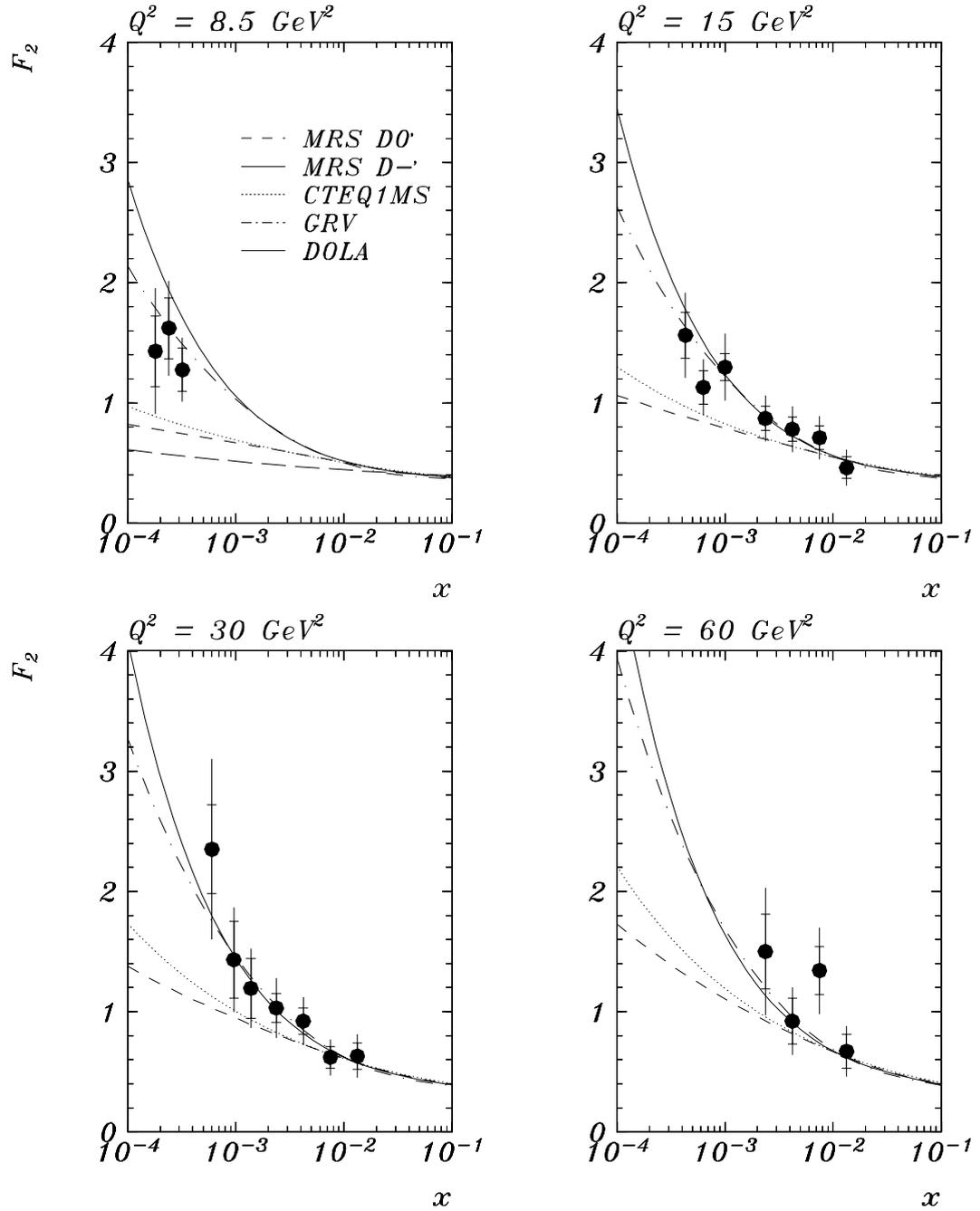The QCD emission of partons can also be observed as jets. In the basic deep

Figure 1.3: Measured $F_2(x, Q^2)$ for four Q^2 values at H1. Total errors (statistical $\oplus$ systematic) are shown, but all points have an additional 8% normalisation uncertainty. Some F_2 parametrisations are indicated. [8]

inelastic collision two jets are expected: a spectator jet formed by the proton remant and a current jet from the scattered quark. At HERA there is sufficient energy available for further clearly separated jets to arise from the QCD radiation of high energy partons [10]. The relative rates of events with particular jet configurations are sensitive to the strong coupling constant α_s.

Amongst the deep inelastic events seen at HERA in 1992, a selection was found in which no proton remnant or other energy deposit was found in the very forward region of the detector [11]. These are compatible with the idea of a hard diffractive process in which the proton radiates a colourless low momentum object and remains itself intact or almost intact. This object, sometimes known as a pomeron, is not described in perturbative QCD, but HERA offers the opportunity to probe its partonic structure with high–Q^2 bosons.

1.2   Photoproduction

The dominant contribution to the electron–proton cross–section at HERA comes from photoproduction events, that is, events in which an almost real photon is radiated from the electron and interacts with the proton. In this case the electron suffers only a very small degree of scattering and the photon is radiated almost collinear with the incoming electron. The physics of these events is that of photon–proton collisions; it is valid in this regime to include the radiation of the photon by the electron as an independent factor in the cross–section calculations (see, for example, [12]). Naturally there is no value of Q^2 which marks a sudden boundary between deep inelastic events and photoproduction events. Generally an event in which Q^2 is less than about $1 GeV^2$ would be considered photoproduction, though in H1 photoproduction events are often identified by the presence of the scattered electron in the 'electron tagger', which constrains Q^2 to be less than $10^{-2} GeV^2$.

Photoproduction events are generally divided into two classes according to the transverse momentum in the final state. Processes resulting in small average p_T, a few hundreds of MeV, are called 'soft'. Higher transverse momentum, 'hard' processes are a signature of some hard subprocess (the p_T–producing vertex or vertices) which are calculable in perturbative QCD. So that this is valid a study of QCD via hard scattering in photon–proton collisions would insist on a transverse momentum

of at least the order of 1 GeV.

Soft processes are described by the vector meson dominance model (VMD, or sometimes VDM), in which the photon becomes an off–shell vector meson which is put on shell by some small momentum transfer from the proton. The major contribution arises from the lightest vector mesons: ρ, ω and ϕ, but the description can be extended to, for instance, diffractive and elastic production of J/ψ–mesons.

It is possible to divide the hard processes into three categories: 'direct', 'resolved' and 'anomalous'. Examples of direct and resolved processes are shown in figure 1.4. The direct processes are those of photon–gluon fusion and QCD Compton in which the photon couples directly to a quark which effectively absorbs the photon. In resolved processes only a part of the photon takes part in the hard interaction leaving a photon remnant which may be identifiable, although it typically has rather low transverse momentum. Anomalous processes are those in which a parton with high p_T in the photon is involved in the interaction, and which therefore give rise to a tail of high p_T events which would not be expected if all the transverse momentum were presumed to come from the proton.

The distinction made between the processes above is somewhat arbitrary and the categories are often differently defined [13]. Anomalous processes could be regarded as high p_T versions of the VMD–type interaction. Indeed the VMD model must account for all the diagrams in the case of low transverse momentum in the final state. At higher orders than are shown in figure 1.4 the distinction between direct and resolved processes is also no longer clear.

The study of photoproduction events at HERA provides a further test of QCD both in the perturbative regime and non–perturbative regime via hard and soft processes respectively [14, 15]. It is also possible to measure the gluon content of the proton by identifying photon–gluon fusion events.

Measuring the total photon–proton cross–section at HERA provides a test of the understanding of these interactions since centre of mass system energies up to 314 GeV are reached in comparison to less than 18 GeV in previous experiments [16]. The cross–section is dominated by soft processes but the contribution from resolved processes is expected to become significant at higher energies. A more direct study of the topology of hard scattering events can be made by identifying jets [17] which therefore allows tests of perturbative QCD.
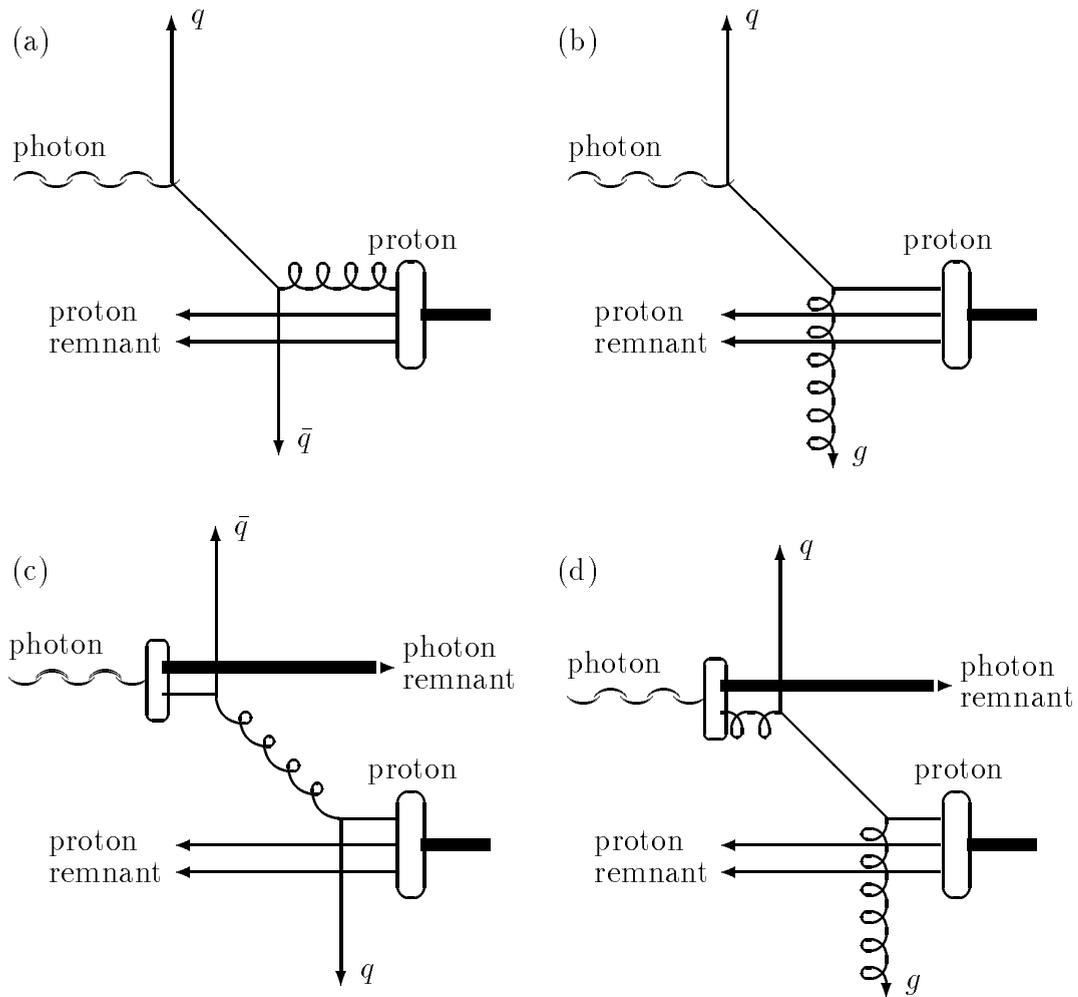
Figure 1.4: Some direct and resolved γp processes. (a) photon–gluon fusion; (b) QCD Compton; (c) and (d) examples of resolved processes.

Samples of photon–gluon fusion events can most easily be isolated in the production of heavy quarks, mostly $c\bar{c}$ pairs [18]. The small charm content of the proton means that, in certain kinematic regions, photon–gluon fusion becomes the dominant charm producing process. Production of J/ψ–mesons (a bound state of $c\bar{c}$) via photon–gluon fusion is a well understood and calculable process with a cross–section proportional to the gluon content of the proton. Moreover J/ψ–mesons are readily identifiable by their decays into muon or electron pairs. The study of J/ψ production via the photon–gluon fusion process will therefore allow measurement of the gluon structure function of the proton [19].

1.3 Physics with Muons

The most prolific physics sources of muons in H1 are $\gamma\gamma \rightarrow \mu^+\mu^-$ processes, charm quark decay ($c \rightarrow \mu\nu_\mu s$) and J/ψ decay ($J/\psi \rightarrow \mu^+\mu^-$).

Muon pair production by two photons, one from the electron and one from the proton, has a total cross–section of about 100 nb, but the muons are typically at low angles to the beam–pipe and have low momentum. The efficiency of detection of such muons is low, and this cross–section is reduced by a factor of about 1000 if the conditions on muon detection are a momentum of greater than 5 GeV and a direction within the angular acceptance of the detector. A measurement of the photon content of the proton could be made with these events [20].

Charm quarks are produced prolifically at HERA, the greatest contribution arising from the photon–gluon fusion process giving rise to a $c\bar{c}$ pair. The cross–section is estimated at about $0.6\mu b$. A method of identification of such events is to search for lepton pairs. The branching ratio for a charm quark to $l\nu_l s$ is about 20% (l is a muon or an electron), so that the cross–section for di–leptonic charm events is about 20 nb. Muons are generally of low momentum and within jets. After taking detector acceptance of such events into account the resulting cross–section is about 100 pb for the identification of $c\bar{c}$ events via di–leptonic decay [21].

J/ψ–mesons are produced at HERA with an estimated cross–section of about 10 nb, and decay to a $\mu^+\mu^-$ pair with a branching ratio of 6%. The cross–section is reduced to about 100 pb once angular and p_T cuts are applied to the decay muons so that they can be expected to be detected in H1 [19].

The gluon content of the proton can be measured by studying open charm and bound charm (J/ψ) production via the photon–gluon fusion mechanism.

A very small muon yield arises from the decay of W–bosons, the cross-section for the production of which is sensitive to the triple gauge $WW\gamma$ vertex. Approximately 100 W bosons only are expected with $100pb^{-1}$ integrated luminosity [22]. In addition new heavy fermions are sought with a muon amongst the decay products, for example a heavy neutrino decaying to $e\mu\nu_\mu$ [23]. Muons from both of these sources would typically be produced in the forward direction with very high momentum.

Charged kaons and pions often decay in the H1 calorimeters producing muons which are a background source to the above mentioned processes. Muons visible in the detector from these sources are produced with a cross–section of the order of 100 nb, which reduces to less than 1 nb if a p_T cut of 2 GeV is applied [24]. A momentum measurement for the decay muons will help recognition of such decays since the track left by the charged kaon or pion will not match the muon momentum [25].

Further background muons are cosmic muons and beam halo muons. Beam halo muons are a product of the collisions of stray protons with the material of the beam–pipe and follow parallel to the beam–pipe through the H1 detector [26]. Both cosmic and beam halo muons are useful for calibration of the detector and are easily recognisable.

Chapter 2

The H1 Detector

2.1 Introduction and Overview

H1 is a composite apparatus utilising several different particle detection techniques combined in such a way as to be able meet the task of analysing collisions between 30 GeV electrons and 820 GeV protons. The electrons and protons circulate in HERA in bunches separated by 96 ns, but an electron–proton collision only occurs approximately once every 10^5 times that bunches pass through one another in the H1 interaction region [27]. These collisions must be distinguished from the high background caused by conversion of synchrotron radiation from the electrons and events in which a proton collides with a gas particle in the 'vacuum' (beam–gas events) or with the beam–pipe (beam–wall).

The H1 detector is designed to surround the interaction region as completely as possible so that as few collision products as possible escape undetected. Essentially, this hermeticity is spoiled only by the beam–pipe itself which has an outer radius of about 192 mm.

The requirements of the H1 detector are determined by the physics to be studied and the background conditions. Rejection of interactions which are not electron–proton collisions is a high priority and the ability to reconstruct the interaction vertex point for an event is therefore important. Lepton identification and momentum measurement is needed for the study of the production of particles, for instance heavy quarks and new exotic particles, through their leptonic decays, and for the detection of the scattered electrons involved in neutral current deep inelastic scat-
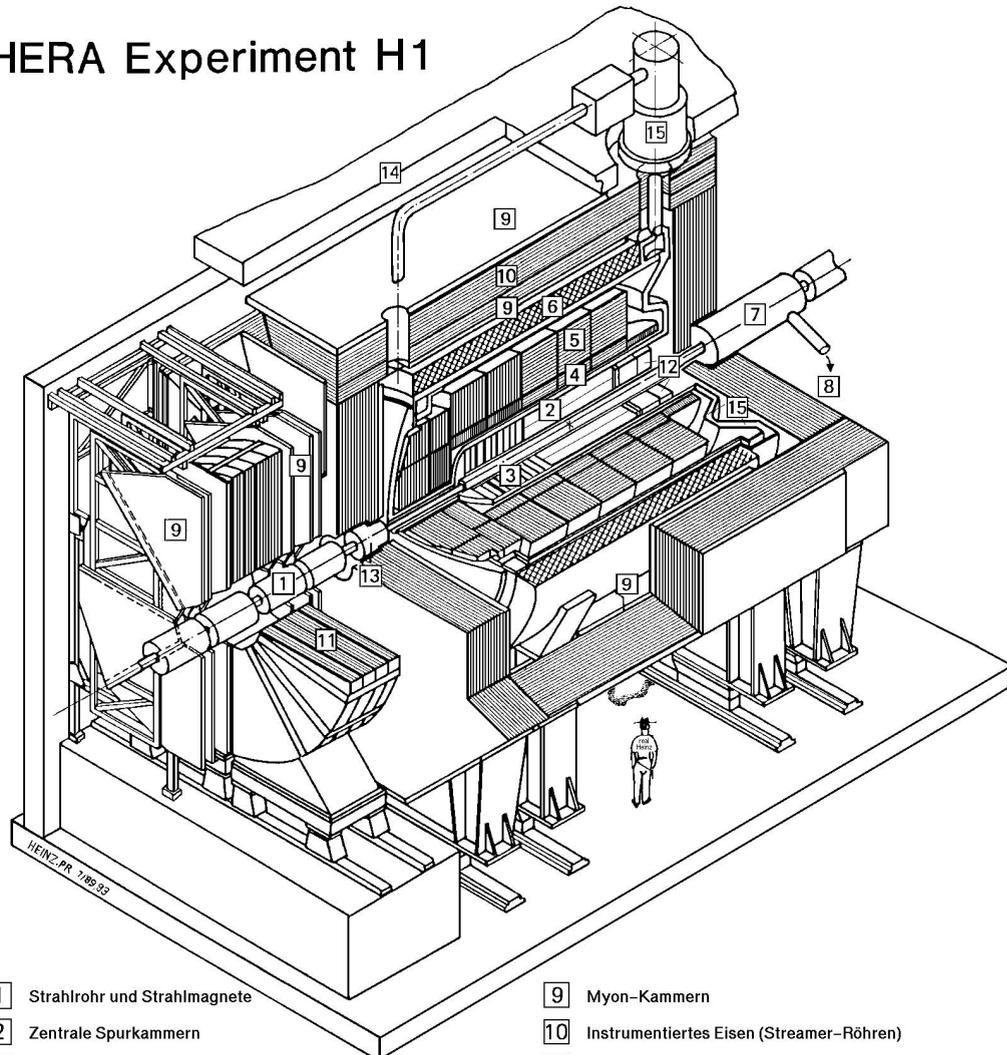
tering events. Measurement of energy flow requires good calorimetry which should be hermetic, especially as charged current deep inelastic events are recognised by missing transverse momentum corresponding to the unseen neutrino. The study of high density, high energy jets and the momentum measurement of leptons requires precision tracking of particles in a magnetic field around the interaction region.

In order to describe the detector standard coordinate systems are used. The z–axis is parallel to the beam pipe, has its origin at the nominal vertex point in the centre of H1 with the z coordinate increasing in the direction of the protons. Cylindrical polar coordinates, θ and ϕ are then used, θ being the polar coordinate such that $\theta = 0°$ corresponds to the proton direction and $\theta = 180°$ to the electron direction, and ϕ being the azimuthal coordinate. A right–handed coordinate set (x, y, z) is also defined , where the y–axis is vertical. Often the terms 'forward' and 'backward' are used to describe the two halves of the detector corresponding to $\theta < 90°$ and $\theta > 90°$ respectively.

The H1 detector is shown in figure 2.1. Its overall form reflects the imbalance of the electron–proton collisions, the forward region being designed to deal with high particle densities and high energies. A super–conducting coil of radius 3 m provides a solenoidal field of 1.15 T in the centre of H1, varying by less than 2% over the entire region of the tracking detectors [27]. Within the coil are the tracking system, comprising drift chambers and multiwire proportional chambers, electro-magnetic and hadronic calorimeters and scintillation counters for the recognition of proton induced background events. Around the coil is the iron return yoke which is laminated with streamer tubes between the laminations in which hadronic energy escaping from the central hadronic calorimeter can be measured, and in which muons can be identified. Further forward than the return yoke is a spectrometer for the detection and momentum measurement of high energy muons. Not shown in figure 2.1, but further along the beam–pipe in the backward direction, are two more background identifying scintillator walls, an electron tagger ($z = -33$ m) for photoproduction events, and a photon detector ($z = -103$ m) which is used with the electron tagger to monitor the luminosity.

A trigger which is designed to recognise the occurrence of an electron–proton collision is implemented, which must cope with the very high rate of bunch crossings in H1 and the large data output of the detector.

HERA Experiment H1

1	Strahlrohr und Strahlmagnete	9	Myon–Kammern
2	Zentrale Spurkammern	10	Instrumentiertes Eisen (Streamer–Röhren)
3	Vorwärtsspurkammern und Übergangsstrahlungsmodul	11	Myon–Toroid–Magnet
4	Elektromagnetisches Kalorimeter (Blei)	12	warmes elektromagnetisches Kalorimeter
5	Hadronisches Kalorimeter (Edelstahl)	13	Vorwärts–Kalorimeter
6	Supraleitende Spule (1.2T)	14	Betonabschirmung
7	Kompensationsmagnet	15	Flüssig Argon Kryostat
8	Helium Kälteanlage		

4, 5 } Flüssig Argon

Figure 2.1: A cut away view of the H1 detector.

Figure 2.2: An r–z projection of the H1 tracking detectors.

2.2   Tracking Detectors

At the heart of the H1 detector are the tracking detectors (figure 2.2) which are divided into two mechanically separate sections, the central tracking detector (CTD) and the forward tracking detector (FTD). Each contains drift chambers, which allow precise reconstruction of the paths of charged particles, and proportional chambers which give very fast information for triggering purposes.

Drift chambers contain a gas which is ionised by a charged particle passing through it. The ion pairs created drift in a region of field, the positive ions towards a cathode and the electrons towards an anode wire. Near an anode wire the field is stronger such that multiplication occurs, that is, the electrons gain sufficient energy between collisions to liberate further ion pairs. It is the anode wires which are monitored to find pulses which are induced by the moving charges near the anode wire in the drift chamber. The time at which the pulse forms depends on the distance that the electrons must drift in the field before arriving in the region of the high field. Measuring this time provides an accurate measure of the distance from the anode wire which the charged particle passed, the resolution being typically a few hundred microns. By sampling the pulses at both ends of the anode wires it is possible to compare the sizes of the pulses and so estimate the position along the wire of the

particle, a usual resolution being 1% of the wire length. By combining different orientations of sense (anode) wires, the path of a charged particle traversing the detectors can be accurately reconstructed and the momentum determined by the amount of bending in the magnetic field.

Proportional chambers contain closely spaced wires, arranged such that any particle traversing the chamber must pass through a high field region close to an anode wire in which multiplication occurs. Cathode pads or anode wires may be sampled for pulses. A signal is received very quickly in response to a passing charged particle due to the short maximum drift time. This is useful for triggering. The position resolution is rather coarse, depending on the separation of the readout pads or wires, but the time resolution is of the order of tens of nanoseconds.

The main part of the CTD is the central jet chamber (CJC) which is divided into two sections, most centrally CJC1 and outside this CJC2. Sense wires are strung parallel to the beam–pipe and are sampled at both ends so that the point along a wire at which a charged particle passes can be approximately determined, as well as the drift coordinate which provides a precise point in the r–ϕ projection. CJC1 and CJC2 are split into 30 and 60 cells in azimuth respectively, each cell containing 24 (and 32) wires which form a plane tilted at about 30° with respect to the radial coordinate. This tilt ensures that reasonably stiff tracks will always cross a wire plane in each of CJC1 and CJC2 and will also be detected in more than one cell, allowing resolution of the ambiguity of the drift coordinate (from the pulses on a single sense wire it is not clear on which side of the wire a particle passes).

In order of increasing radius the components of the CTD are the inner multiwire proportional chamber (CIP), the inner z chamber (CIZ), CJC1, the outer z chamber (COZ), outer multiwire proportional chamber (COP) and CJC2, as shown in figure 2.3. The z chambers complement the CJC by providing an accurate z coordinate, having wires strung perpendicular to the beam direction, and a moderate ϕ coordinate achieved by two ended readout of the wires. Each sense wire forms a regular polygon in an r–ϕ plane (16 sided for CIZ, 24 sided for COZ) which is centred at the centre of the beam–pipe, and each cell consists of 4 sense wires which are separated in the radial coordinate, r. The CIZ and COZ are divided into 15 and 23 cells in z respectively.

Each of the two proportional chambers consists of two concentric chamber layers,
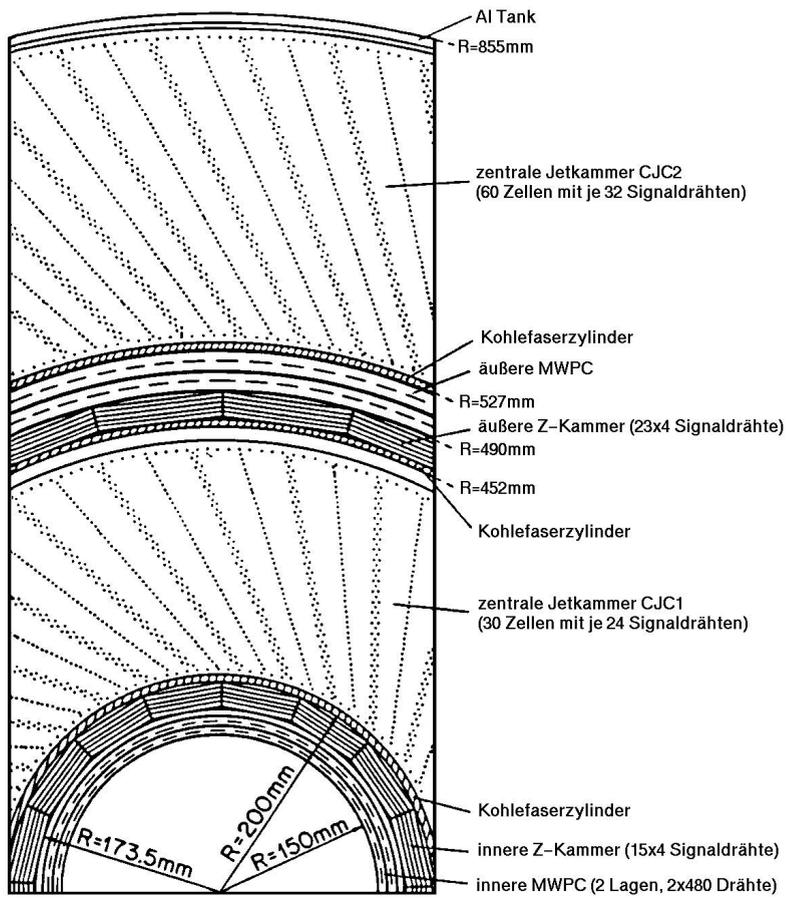
Figure 2.3: An r–ϕ cross–section through the CTD.

the output being read from cathode pads. For the CIP the pads are 36.6 mm long in z and cover 45° in azimuth, the two layers being displaced from one another by half a cell in azimuth to half the effective ϕ resolution. The COP has pads 120 mm long in z and covering 22.5° in azimuth, also giving a 16–fold segmentation in ϕ.

The forward tracking detector consists of three similar 'supermodules', each one comprising in order of increasing z: planar chambers, a proportional chamber, a transition radiator and a radial drift chamber. Each supermodule has three layers of cells which form the planar chambers, the sense wires in each layer being parallel to one another but the three layers lying at 60° to one another so that an accurate x–y coordinate is found by combining the information from each. The proportional chambers (FWPC) are similar to those in the CTD but have ring shaped cathode pads, each covering 45° or 22.5° in azimuth and having a radial width between 18 and 37 mm depending on the radius. They also serve the same purpose, providing a very quick signal with coarse position resolution useful for triggering. The transition radiators are purely passive, producing x–rays when an electron passes through which can be detected in the radial chambers, leading to larger signals than for heavier particles and hence allowing them to be discriminated. Sense wires in the radial chambers are strung radially, the chamber being segmented 48–fold in ϕ, each cell having 12 sense wires separated in z by 10 mm. By sampling the pulses at both ends of the wires the radial coordinate can be approximately determined ($\sigma \approx 3$ cm [27]) in addition to the accurate ϕ coordinate.

Tracks at polar angles greater than about 155° are not efficiently reconstructed in the above chambers, and the backward proportional chamber (BPC) is designed to give an accurate space–point (an angular resolution of about 0.5 mradians [27]) up to $\theta \approx 175°$. This is achieved by extracting signals from the anode wires rather than cathode pads and having four layers of wires, each one orientated at 45° relative to one another. Within a layer the wires are parallel and separated by 2.5 mm.

The tracking system as a whole is designed to provide a momentum measurement resolution given by $\sigma_p/p \approx 0.003p$ (p in GeV), and an angular resolution, $\sigma_\theta \approx$ 1 mradian [27].
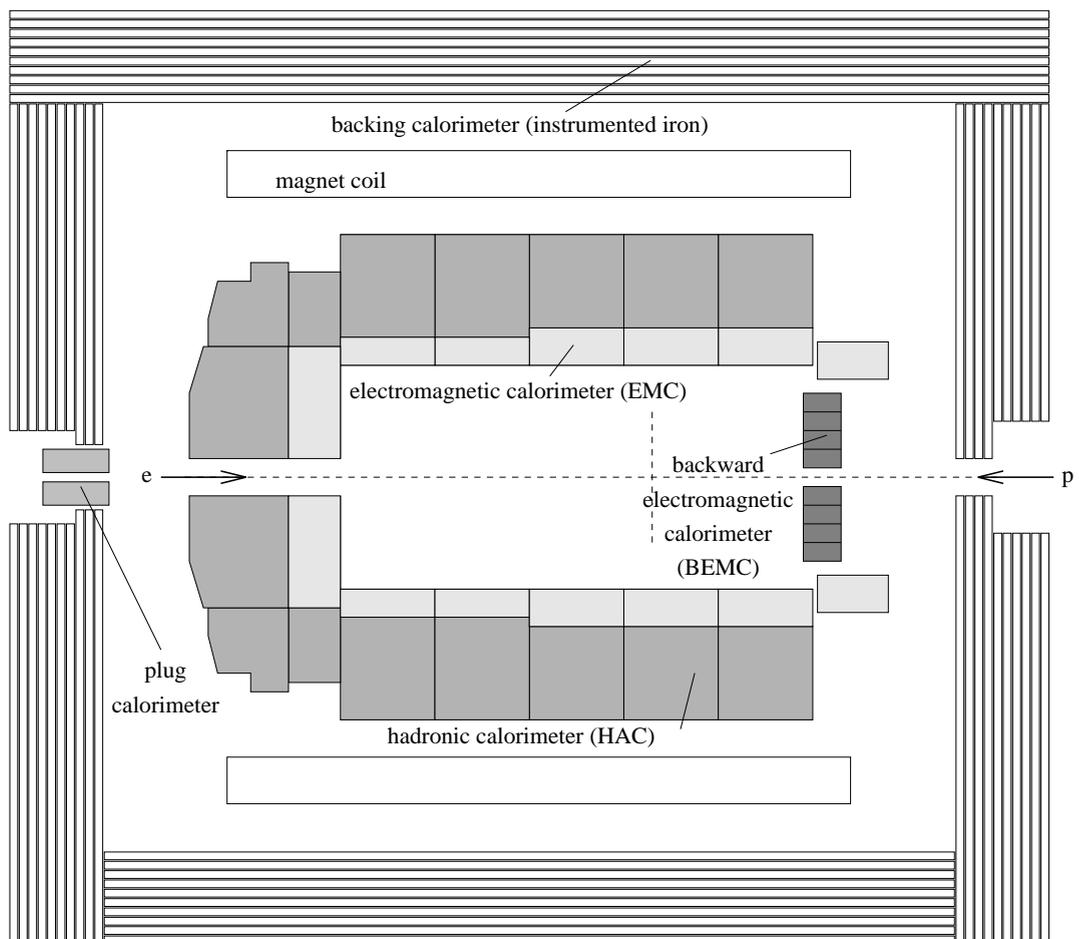
2.3   Calorimeters

The calorimeters measure the energy of incident particles by inducing particle showers in some medium (lead or steel in H1) and inserting sensitive regions within the medium to detect the shower development.

Photons and electrons with high energy which are incident on an absorber form a cascade of further photons and electrons by the processes of Bremsstrahlung and pair production, these being the dominant processes of energy loss [28]. The longitudinal development of such an electromagnetic shower is characterised by the radiation length, X_0, the mean distance over which a high energy electron loses all but e^{-1} of its energy. Eventually all the energy will be lost through ionisation if the shower is contained completely in the calorimeter, so that measuring the total amount of ionisation gives a measure of the energy of the incident particle.

Hadronic particles form showers in a very different way, the dominant process of energy loss being through inelastic nuclear collisions, the products of which take part in further such collisions. The characteristic length of the shower is the nuclear interaction length, λ_I, which is typically much greater than X_0 for the absorbers used (for lead $\lambda_I \approx 30.X_0$) [28]. The π^0 mesons liberated decay to photon pairs and start electromagnetic cascades which have a much shorter characteristic length so that a hadronic particle incident on a calorimeter deposits a significant fraction of its energy early (from the decay of π^0 mesons liberated in the first nuclear collision) and then forms a much more slowly developing shower. About 30% of the energy is dissipated in the breakup or excitation of nuclei and other processes which are not detectable [29]. Most detectors therefore give a greater response for electromagnetic showers than for hadronic showers initiated by particles of the same energy which must be compensated for.

The resolutions of calorimeters, σ_E/E, tend to be dominated by a term proportional to $E^{-\frac{1}{2}}$ which is due to the statistical fluctuation in the number of particles produced in the shower development. Other terms appear due to noise, calibration uncertainties, non–uniformity and incomplete shower containment. Non–compensation for the difference between the responses to hadronic and electromagnetic showers adds a constant term to σ_E/E approximately proportional to the degree of non–compensation [28].

Figure 2.4: An r–z view of the calorimeters.

The H1 calorimeters are shown in figure 2.4. In the polar angular range between 4° and 153° a liquid argon calorimeter consisting of an electromagnetic part (EMC) and a hadronic part (HAC) is situated within a single cryostat. For access to the central tracking region a separate lead–scintillator calorimeter (BEMC) is used in the backward region. In the very forward region between the liquid argon calorimeter and the beam–pipe is the plug calorimeter with copper absorber and silicon pad readout. The return yoke iron is also instrumented with streamer tubes and acts as a tail catcher for escaping hadronic energy.

The EMC uses lead as the absorbing medium, plates of 2.4 mm being interspersed with 2.35 mm liquid argon filled gaps. For each gap there is a plane of pads from which the signals are taken. In the HAC 19 mm thick stainless steel absorber plates are interspersed by double gaps of 2.4 mm liquid argon, a plane of readout pads being situated on either side of a board in the centre of the double gap. The total depth of the electromagnetic part is between 20 and 30 radiation lengths and the entire liquid argon calorimeter has a depth between $5\lambda_I$ and $7\lambda_I$. Fine granularity is achieved by dividing the calorimeter into about 45000 cells. It is this granularity which allows good compensation since hadronic showers and electromagnetic showers can be distinguished by their different shapes. Then for energy deposits which are recognised as being part of a hadronic shower a weighting can be applied to the detector signals [30]. Similarly noise in the calorimeter can be reduced by ignoring cells which give a significant signal but which appear geometrically unrelated to any other significant cell.

The electromagnetic energy resolution of the liquid argon calorimeter is given approximately by $\sigma_E/E = 12\%/\sqrt{E} \oplus 1\%$ [27] (E in GeV) with a present calibration uncertainty of about 3% [31]. Hadronic energy can be measured with a resolution $\sigma_E/E = 50\%/\sqrt{E} \oplus 2\%$ [27], presently with a 5% calibration uncertainty. [31].

The backward electromagnetic calorimeter (BEMC) covers the polar angular range approximately between 151° to 177°, having a circular front face of diameter 162 cm. It is layered longitudinally, alternately 2.5 mm of lead as the absorber, and 4 mm of plastic scintillator as the sampler, there being in total 50 sampling layers. Cross-sectionally the BEMC is segmented into 88 stacks, most of which are square with side 15.9 cm. Signals are carried by wavelength shifters which run along the sides of the stacks. On two sides of the stacks are two such wavelength shifters, each of 8 cm width, which run along the entire depth of the stacks and offer some

space resolution within a stack. Wavelength shifters of 16 cm width cover the last 15 sampling layers of the other two sides so providing information about the later shower development. In total the BEMC has a depth of 22.5 radiation lengths and 0.97 hadronic absorption lengths which means that only about 30% of the energy from interacting hadrons is typically contained in the calorimeter, and about 30% of incident hadrons do not leave any signal [27].

An important task of the BEMC is the identification of scattered electrons in low–Q^2 ($Q^2 <\approx 100 GeV^2$) deep inelastic scattering events. Its resolution in reconstructing the energy of an electron is given by $\sigma_E/E = 10\%/\sqrt{E} \oplus 2\%$ [27], and there is presently an approximately 2% calibration uncertainty [32]. Position is determined with a resolution of about 1.3 cm for such electrons. A hadronic energy resolution of about $\sigma_E/E = 80\%/\sqrt{E}$ [27] is possible by combining the BEMC and the tail catcher behind the BEMC [27].

Eleven layers of streamer tubes interspersed between the ten layers of iron comprising the return yoke are instrumented by pads, from which signals are taken. The pads vary in size from about 30 cm by 30 cm to about 50 cm by 40 cm and the signals from 5 (or 6) pads which lie behind one another are summed to give an effective two–fold longitudinal segmentation to the hadronic energy measurement in the tail catcher. The tail catcher, which serves to measure hadronic energy which escapes from the liquid argon calorimeter and the BEMC, covers the polar angular range from 6° to 172° and has a depth of about $4.5\lambda_I$ with an energy measurement resolution of $\sigma_E/E \approx 100\%/\sqrt{E}$ [27].

The plug calorimeter fills the gap between the liquid argon calorimeter and the beam–pipe to avoid the loss of transverse hadronic energy at low angles. It consists of nine layers of copper absorber interspersed with eight layers of silicon detectors, only four of which were installed in 1992. Suffering from lack of containment of showers and coarse sampling, the energy resolution is $\sigma_E/E \approx 150\%/\sqrt{E}$ [27].

2.4   Muon Detectors

Muons with greater than about 1.2 GeV energy will reach the iron return yoke. Being instrumented with limited streamer tubes the muons can be detected here, the direction of the muon can be determined and an approximate momentum measurement is

10 cm

iron
laminations

LST layers
with pads

LST layers
with strips

r

z

muon

Figure 2.5: Cross–sectional view through the instrumented iron.

also possible. In the forward direction the muon detection in the instrumented iron
is complemented by the forward muon system (FTD) which consists of layers of drift
chambers either side of an iron toroidal magnet, and which can provide a reasonable
momentum measurement for muons up to very high momenta ($\approx$ 200 GeV) as well
as a directional measurement. Both muon systems can only determine the direction
and momentum of a muon within the limits of multiple scattering which the muon
suffers, and therefore it is advantageous to use the muon detectors to identify tracks
left by muons in the tracking detectors.

Each streamer tube of the instrumented iron has a square cross–section of 1 cm
side and a single wire in the middle running along the length of the tube. High
voltage is applied to the inner sides of the tube and the wire is kept at ground

potential. The very high field means that signal amplification is not necessary, the signals can be read directly from the wires or from pads or strips which are glued on to the high resistance covers of the streamer tubes.

A cross–sectional view through the instrumented iron is shown in figure 2.5. Ten iron layers are interleaved with a total of sixteen streamer tube layers. Signals are taken from wires in all of the layers, eleven of the layers also have pad readout as explained above, and the remaining five layers have strips running perpendicular to the wires. Using the wire signals the position of a passing muon can be determined with a resolution of about 3–4 mm, strips give a resolution of about 10–15 mm in the perpendicular coordinate. Pads provide a space–point with an accuracy of about 10 cm [27].

In the barrel region of the instrumented iron muons can be efficiently reconstructed if they have greater than about 2 GeV momentum, but otherwise the track may not be sufficiently penetrating to leave enough signals in the muon detectors. A momentum estimation is possible using the field in the return yoke iron but the aim is to identify the muon track in the central tracking detectors by using the reconstructed track in the instrumented iron.

In response to the higher density of tracks in the forward direction in H1 and the more energetic muons produced in this direction there is a separate muon spectrometer (FMD) which detects muons of energy greater than 5 GeV in the polar angular range from 3° to 17° and provides a momentum measurement for muons up to about 200 GeV. This is achieved by three double layers of drift chambers either side of an iron toroidal magnet. The entire system sits forward of the forward endcap of the instrumented iron and so is independent of the field from the H1 solenoidal magnet. A detailed description of this detector is given in the following two chapters.

2.5   Scintillator Walls

Situated behind the BEMC at $z \approx -2$ m are two walls of scintillators which provide timing information with a resolution of about 4 ns. These form the time of flight device (ToF), which by measuring the time of particles passing through it with respect to the beam crossing time, is able to distinguish proton induced background events from genuine electron–proton collision events.

The principle of this distinction is that if a proton upstream of the ToF interacts with gas particle in the beam–pipe or with a part of the beam–pipe itself, then the products of that interaction will pass through the ToF device at about the same time as the proton bunch from which the proton originated. In contrast, if the proton were involved in an electron–proton collision in the interaction region of H1, then the products of that collision would reach ToF somewhat later, in fact at about the same time as the passing electron bunch. This time difference is about 13 ns, but varies because the proton bunches have a length equivalent to 2–3 ns so that interactions do not occur exactly at the nominal H1 vertex point.

The plastic scintillator planes of the ToF device are mounted perpendicular to the beam–pipe and cover an area about equivalent to that of the BEMC, the more forward plane being divided into 16 separate counters and the more backward plane into 8 larger counters. Lead plates of 6.5 mm thickness sandwich the scintillators, so protecting them from the effects of synchrotron radiation from the electrons. For the identification of background events and possible physics events, three time windows are defined with respect to the beam crossing time. The first window, called 'global', is designed to contain all hits in the ToF device associated with a particular beam crossing, and so has a width of almost 96 ns. A second window is defined around the time at which background hits from upstream proton interactions are expected and has a width of about 25 ns. This 'background' window is within the global window, as is the 'interaction' window which starts after the end of the background window and has a width of about 13 ns. Electron–proton collisions and synchrotron radiation from the electron bunches will result in hits in the interaction window.

In 1992, using ToF signals in the background window as a veto on events triggered by other parts of the detector (see below) resulted in a 99% reduction in the trigger rate [27]. Such a reduction is vital, since otherwise the detector would be practically disabled by constantly processing background events.

Further upstream, at $z \approx -6.5$ m and $z \approx -8.1$ m respectively, are two further double scintillator walls, the outer and inner veto walls. The outer veto wall covers a large area corresponding approximately to that of liquid argon calorimeter and has a time resolution of about 8 ns, whilst the inner veto wall extends only about 1 m from the beam–pipe and has a resolution of about 3 ns. Using the same principle as the ToF device, the veto walls are able to provide signals useful for proton induced background recognition, and are also used for assessment of the

background conditions.

2.6 Electron Tagger and Photon Detector

The electron tagger (ET) and photon detector (PD), situated respectively at $z = -33$ m and $z = -103$ m very close to the beam–pipe, are used in coincidence to monitor the luminosity in H1. They are able to measure the rate of the Bremsstrahlung interaction $ep \rightarrow ep\gamma$ by detecting the final state electron and photon. The cross–section for this interaction is precisely known so that a measurement of the rate together with a known acceptance of such events provides a measure of the luminosity.

Both detectors are crystal Čerenkov calorimeters, formed from an array of crystals 20 cm ($\approx 22X_0$) long with square cross–section. The ET is a 7 by 7 array covering an area 154 mm by 154 mm, and a 5 by 5 array covering a 100 mm by 100 mm area forms the PD. An energy resolution of $\sigma_E/E = 10\%/\sqrt{E} \oplus 1\%$ [27] (E in GeV) is achieved, with a position resolution of better than 1 mm.

The visible cross–section is about 28 mb in the electron tagger, corresponding to a rate of about 400 kHz at design luminosity. Background arises from synchrotron radiation, proton beam halo and Bremsstrahlung interactions of electrons with gas particles in the beam–pipe. The photon detector is guarded against proton beam halo by 2 m of iron behind it, whilst a lead filter of width $2X_0$ and a water Čerenkov counter of width $1X_0$ in front protect against the synchrotron flux and act as a veto, events where a particle is detected in the water Čerenkov counter being rejected. About 10% of the rate is expected to come from the interactions with gas particles in the beam–pipe. The amount of this source of background can be estimated by making use of electron 'pilot' bunches which have no partner proton bunch. A correction is made based on this measurement.

The greatest contribution to the uncertainty in the absolute luminosity measurement is due to the uncertainty in acceptance, presently at about 5.5%. It is expected that the total systematic error in luminosity measurement can be reduced from the present 7% to less than 4% [27].

The electron tagger also serves to identify the scattered electron in photopro-

duction events where $Q^2 < 0.01 GeV^2$, in particular suppressing the proton induced background.

2.7   Triggering

The task of the trigger is to recognise physics events, filtering out the background events which do not result from electron–proton collisions. Every 96 ns there is a beam crossing in the vertex region of H1, that is, an electron bunch and a proton bunch pass one another and interactions may occur. With every bunch crossing a decision must be made as to whether an interaction has occurred, and in this case the output from all the detectors must be collected, a process which takes about 1 ms. Information for the trigger decision comes from nine separate trigger systems which are based on different parts of the H1 detector, but these 'trigger elements' can only be delivered to the central trigger logic within a time corresponding to about 20 bunch crossings. To avoid having to stop the detector and wait for this time to see whether a bunch crossing resulted in an interaction (which would result in the detector being effectively inactive for more than 95% of the time), the trigger is 'pipe–lined'.

Pipe–lining is the storage of information from successive bunch crossings such that every bunch crossing can be analysed. With every bunch crossing each of the nine trigger systems produces its own trigger elements which it delivers to the central trigger logic. The systems must be synchronised such that the central trigger receives information relating to the same bunch crossing from all of the nine trigger systems at the same time. If the central trigger decides that the trigger signals might signify a physics events then it sends out an 'L1keep' signal to all the detector parts of H1 which causes the freezing of all the detector output information that is stored in pipe–lines. This L1keep decision is made 24 beam crossings after the interaction actually took place, which means that the history of all the detector output over at least the previous 24 beam crossings must be stored at any time. Using pipe–lining means that the detector is only disabled after an interaction has been recognised, and until that time all bunch crossings are surveyed by the trigger.

The trigger is divided into four levels. Described above is the first level, L1, which receives all the trigger elements and combines them logically to form 'subtriggers'.

There can be up to 128 subtriggers in total which are different coincidences of the trigger elements from the separate detector parts, and are divided into three categories: physics triggers which are signatures of physics interactions, monitor triggers which select events useful for detector studies, and the cosmic trigger which selects cosmic ray events for calibration studies. If any single subtrigger condition is satisfied for a bunch crossing then the L1keep signal is issued and the detector is essentially disabled ('dead–time' begins). The rates of acceptances of events by each of the subtriggers is monitored separately, and if any rate becomes too high then that subtrigger is 'downscaled', that is, only a given fraction of events passing the conditions demanded by that subtrigger will cause an L1keep signal.

The L2 trigger makes a more sophisticated decision than L1, analysing the event according to the subtrigger that caused the L1keep signal and producing a decision after 20 μs as to whether the event should be rejected. If the event is rejected then the detector is re–enabled and the time lost was only 20 μs. Otherwise the time consuming operations involved with reading all the detector output information begins, and the L3 decision making process starts. L3, as L2, uses only the information available to L1, the trigger elements, but makes more complex topological studies of the events and takes a few hundred μs to do so, after which the event may be rejected. If L3 does not reject the event then all the detector output is passed on to the central data acquisition system so that an L4 decision can be made.

The L4 trigger operates asynchronously so that the detector is not disabled during whilst it analyses the events. Making all the data available to the L4 trigger takes until about 1 ms after the original L1keep signal, and during this time the detector is disabled. Dead–time ends once this process is finished. Having carried out full event reconstruction using the detector information that was not available to the synchronous triggers, the L4 trigger filters out the remaining events which are identified as not of interest (except a small proportion kept for other studies). L4 accepted events are recorded on tape.

A maximum rate of about 50 Hz for sending events to the central data acquisition system is currently acceptable, which means that the L3 trigger may only accept events up to this frequency. At the same time the dead–time of the detector should be kept low. A dead time of 10% could be achieved with, for instance, an L1keep rate of 1000 Hz and an L2 acceptance rate of about 200 Hz [27]. In 1992 the L2 and L3 triggers were not used so that L1 was only able to accept events at a rate less

than 50 Hz. Since the proton current was only about 1% of the design value, this was manageable and events were recorded to tape at an average rate of about 8 Hz.

Chapter 3

The Forward Muon Detector

3.1   Introduction

Two characteristics of physics events as seen in the H1 detector necessitate a spectrometer capable of identifying and reconstructing the momentum of high energy muons at low angles to the proton direction. Firstly, the momentum spectrum of muons produced in the decay of heavy particles is harder in the forward region than in the central region, and secondly the proton remnant in inelastic events produces a high density of tracks in the forward region.

The forward muon spectrometer at H1 unambiguously identifies muons and produces an independent momentum vector measurement in the polar angular range $3° < \theta < 17°$ and momentum range approximately $5\ GeV < p < 200\ GeV$. It is possible to use the spectrometer independently, but preferably it should be used to identify the track left by the muon in the forward tracker (FT) where a more precise momentum measurement is possible. The ability of the forward muon system to measure the momentum and find the direction of the muon makes it possible to pick the track in the forward tracker from the background of many other tracks, most of which result from the proton remnant. In particular, background muons from kaon decay can be identified by the difference in momentum of the kaon seen in the forward tracker and the muon in the forward muon detector.

In this chapter a description of the hardware of the forward muon detector is given, and the process of reconstructing muon tracks is explained. The next chapter introduces the computer simulation of the detector, and assesses the potential per-

formance, with particular reference to identification of J/ψ particles via their decay into muon pairs as an example of the demands on the forward muon detector made by physics at HERA.

3.2 Hardware Overview

The forward muon detector (FMD) stands outside the iron return yoke, between 6.4 m and 9.4 m from the nominal H1 vertex in the proton direction, and so is not within the solenoidal field of the H1 superconducting magnet. Instead the FMD contains its own toroidal magnet which bends charged particles from the vertex in the polar angle, θ. To detect this bending and so measure muon momentum, and also to find the direction of a muon entering the system, there are three drift chamber layers on either side of the toroid. The forward muon system, comprising the toroid and the six drift chamber layers, is shown in relation to the rest of H1 in figure 3.1. A muon passing through the system is detected in each of the six layers, leaving a signal which can be interpreted to find where the muon was incident on each layer. These space points are used to form a pre–toroid track segment and a post–toroid track segment corresponding to the straight line paths of the muon before and after the toroid. The difference in direction of the two segments which correspond to a single muon track gives a measure of the muon momentum, whilst the direction of the pre–toroid segment indicates the direction of flight of the incoming muon.

Each of the six drift chamber layers is formed by mounting drift cells onto frames, there being in total 1520 cells. Cells are of a particularly simple design, each containing a single sense (or signal) wire with two ended readout allowing a two dimensional space point to be identified. The distance that a muon passed from the wire is calculated from the time at which a signal pulse arrived, and the point along the length of the wire is derived from the relative shapes of the two pulses at either end of the sense wire. Each cell is 12 cm wide and between 34 cm and 241 cm long, and the space point is identified with a resolution of about 250 μm across the width of the cell and between about 2–6 cm along the length. The relative values of these resolutions mean that the orientation of the mounting of cells to form layers determines the ability of the layer to measure a particular coordinate. In fact two different orientations are used, forming layers which produce better measurements of the radial position of the incident muon, the so–called θ–layers, and of the azimuthal position,
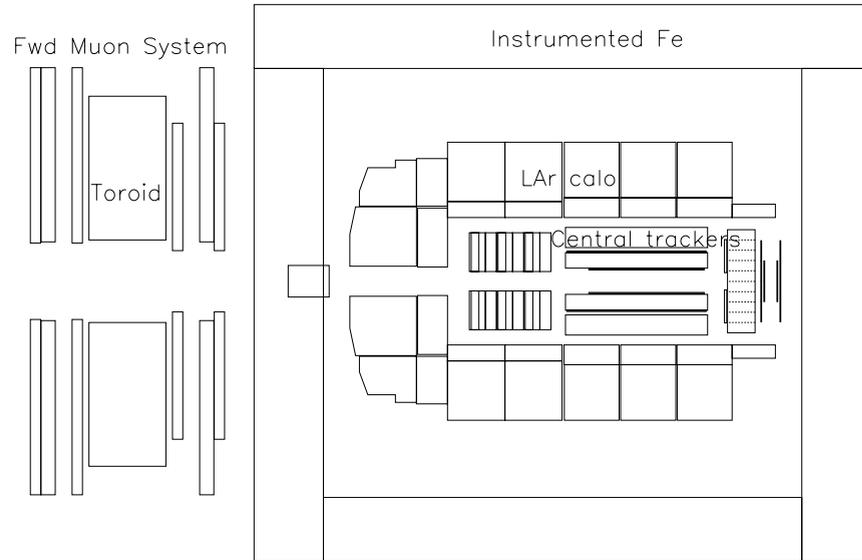
Figure 3.1: The Forward Muon Detector, comprising three drift chamber layers on each side of a toroidal magnet, in relation to the rest of the H1 detector. Protons go from right to left.

the ϕ–layers. On each side of the toroid one ϕ–layer is sandwiched between two θ–layers so that the order of layers in order of increasing H1 coordinate z is θ_1, ϕ_1, θ_2, toroid, θ_3, ϕ_2, θ_4. The toroid itself is of solid iron, extends radially from 65 cm to 290 cm and is 120 cm thick. A field is produced which varies in strength with radius from 1.75 T at 65 cm to 1.5 T at 290 cm, by 12 coils each of 15 turns of copper around the toroid, carrying a current of 150 A.

3.3 Drift Cells

The drift cells are rectangular in cross–section, 2 cm in depth and 12 cm wide, and contain a single nichrome resistive sense wire which runs along the centre of the cell and is of 40 or 50 μm diameter. Two PCB planes, each 1.6 mm thick, form the front and back of the cell, and are supported at the sides by aluminium walls of 0.7 mm thickness. The outer faces of the PCB planes maintain their copper coating, whilst the inside facing surfaces are etched so that copper strips, 4 mm wide, with 2 mm gaps between them run the length of the cells. These act as drift electrodes, being
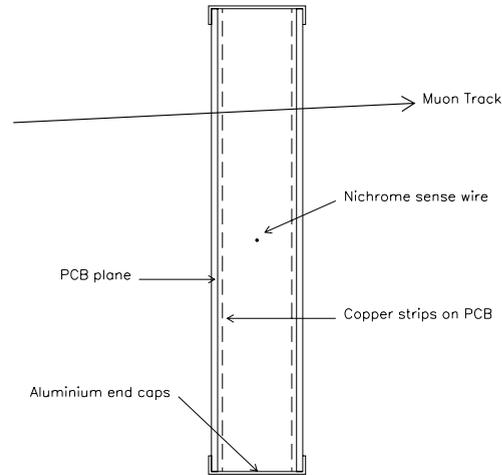
Figure 3.2: A drift cell in cross–section. The sense wire runs along the length of the cell, into the page in this diagram.

linked by a resistor chain across which a potential difference is applied. A total potential difference between the most central strip and ground of 2.88 kV produces an average field in the cell of about 0.48 $kVcm^{-1}$ so as to cause electrons to drift towards the sense wire in the centre. The sense wire itself is kept at the higher voltage of 4.2 kV which produces a region of high field in which signal amplification occurs through avalanching. Electrostatic modelling of the cells has been done and is discussed in some detail in [33]. Essentially the simple design of the cell results in a rather uniform field over most of the cell, although the region of non–uniformity caused by the sense wire extends to about 2 cm from the wire. A gas mixture, 92.5% argon, 5% carbon dioxide and 2.5% methane, flows constantly through the cells and was chosen because of its suitable drift–field to drift–velocity relationship and because of its non–flammability. The cross–section view of a drift cell is shown diagramatically in figure 3.2.

A muon passing through the cell produces a number of electron–ion pairs, through colliding with atoms of the gas, which form ionisation clusters along the path of the muon. In the field of the cell the electrons drift towards the sense wire in the centre at a drift velocity determined by the gas mixture and the field strength. At the cho-

sen field strength the drift velocity in the gas mixture above is relatively insensitive to small variations in the field and is about 5 $cm\mu s^{-1}$. The high field region around the sense wire produces avalanching since the drifting electrons gain enough energy between collisions to produce further ion pairs, and so the signal induced on the wire is amplified. It is the movement of charge around the sense wire that induces the pulse which then propagates in both directions along the wire. A more detailed description of drift chamber operation is given in [34, 26].

The electronics used to sample the signal pulses at each end of the sense wire are isolated from the sense wire by a 1 nF capacitor. The signal from a pre–amplifier of input impedance 200 Ω is fed into an analogue to digital converter (F1001–FADC [35]) which samples at ten times the rate of the HERA bunch cross-ing frequency, so measuring the cell output every 9.61 ns. These FADC's have an 8–bit non–linear response giving an effective 10–bit range and have a memory of 255 time bins which is continually overwritten so that at any time a 2.5 μs history of the cell is stored. In response to an event trigger, the sampling by the FADC is stopped and the memory frozen. A scanner then transfers the contents of the FADC to a front end processor, removing regions of the cell history in which the FADC contents remained below a pre–set threshold to reduce the volume of raw data to be handled. Once this task is complete the FADC's can resume sampling and the raw data from the triggered event is available for on–line processing.

In order to reduce the total number of electronic channels needed to sample the detector output, cells are linked into pairs by a so–called z–link, a wire containing a 330 Ω resistor joining one end of the sense wire of one cell to one end of the sense wire of the partner cell. Then each cell pair has one free sense wire end which is sampled by the above electronics chain. A linked pair of cells is represented in figure 3.3.

3.4   Space–point Reconstruction

Referring to figure 3.3, a muon passing through cell 1 produces a pulse at some point along the sense wire which then propagates along the sense wire in both directions. Both the resultant pulses are sampled and considered in reconstructing the point in cell 1 through which the muon originally passed. The sampling channel at the end
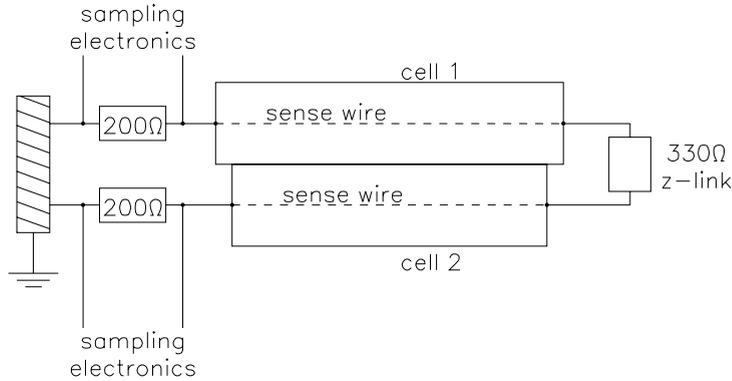
Figure 3.3: A z–linked pair of cells, showing also the preamp input impedances. Components associated with the high voltage supply to the sense wires are not shown.

of cell 1 sees a pulse that has travelled along some fraction of its sense wire, whereas the channel at the end of cell 2 sees a pulse that has travelled along some fraction of cell 1, through the z-link and along cell 2. By comparing the shapes of these two pulses it is possible to identify through which of the two cells the muon passed and where along the wire of that cell to within a few centimetres. The time between the interaction causing the event and the pulse arriving from the muon is a measure of the distance from the sense wire that the muon passed, since for a given wire it is the time for the electrons to drift from the primary ionisations occurring along the muon track to the sense wire, plus some wire–dependent constant. Using this method it is possible to reconstruct the distance from the wire of the muon with a resolution of about 250 μm. The algorithms described below are implemented in reference [36].

3.4.1   Drift Coordinate

Finding the drift coordinate, that is the distance from the sense wire to the path of the muon, is a two stage process. In the first stage the times, t_1 and t_2, of arrival of

the pulses are found and the average of the two, $t = (t_1 + t_2)/2$, is taken to be the 'drift time'. The second stage involves relating the drift time to the drift distance, defined as the distance, x, of the muon from the wire.

Figure 3.4 illustrates graphically the method of calculating the time, say t_1, from a single pulse. Typically, a pulse as seen in the FADC and read by the scanner has a steep rising edge and a long tail. In fact the flatness of the pulse is determined largely by how far along the sense wire it has propagated and figure 3.4 shows the first few time bins of a normal pulse. A threshold is set which is above normal levels of noise, and a pulse is defined to be at least two consecutive time bins with contents above this threshold. As mentioned above, the scanner discards all regions below threshold, except that eight time bins of history are kept immediately before any pulse identified. The average content of these 'front pad' bins is taken to be the zero level for the pulse, a pedestal shown as LBASE in figure 3.4. An algorithm known as the 'leading edge algorithm' or 'first electron method' is used to assign a time to the pulse, which looks through the contents of the time bins representing the steep leading edge of the pulse and searches for the two adjacent bins with the greatest difference in content. This difference is the maximum difference of samples (MAXDOS) and the time bin with the greater content of the two is labelled IMAXDOS. A straight line is defined by the contents of the bins IMAXDOS and IMAXDOS-1 which intersects LBASE at a point A. The time t_1 is defined as some chosen fraction, K, of the way between time A and the time of the bin IMAXDOS. Presently K takes the value 1/3.

This method of associating a time with a pulse aims to be equivalent to finding the time of arrival of the first ionisation cluster at the sense wire, and the resolution attainable in finding this time is limited chiefly by diffusion of the drifting electrons and the width of the FADC bins (9.61 ns). Assuming a perfectly known drift distance to drift time relationship for a cell these two factors impose an intrinsic time determination resolution, practically a best attainable resolution. Electron diffusion gives a contribution to the intrinsic resolution independent of drift velocity but proportional to the square root of the drift distance, whereas the FADC bin width contribution is proportional to drift velocity [34]. The diffusion has been measured to give an uncertainty of about 68 $\mu m cm^{-\frac{1}{2}}$ [26], while a drift velocity of 4.96 $cm\mu s^{-1}$ in the region $x > 0.5\ cm$ [33] adds a constant 137 μm in quadrature. Thus a drift coordinate resolution cannot possibly be better than about 150 μm at $x = 1\ cm$ and about 200 μm $x = 5\ cm$, and this is only attainable with a perfect
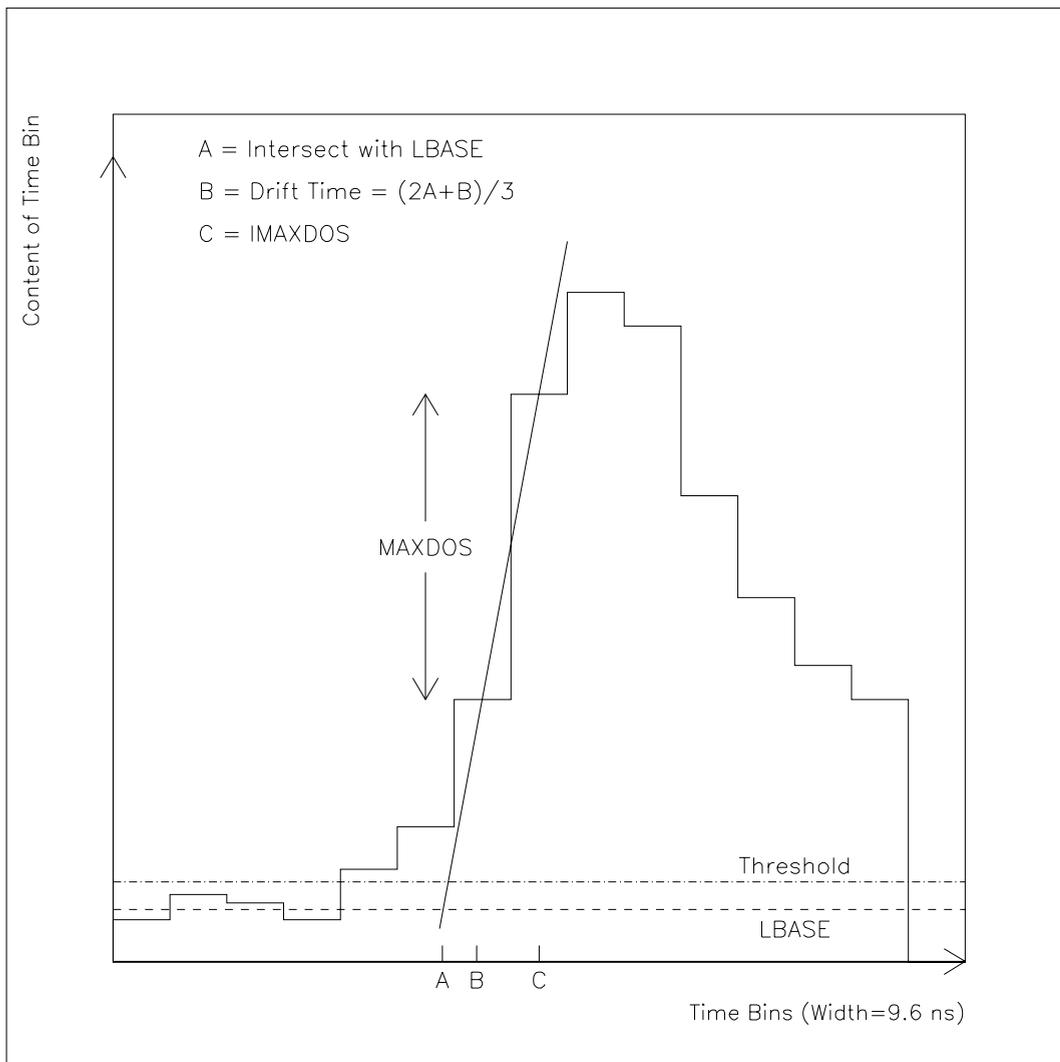
Figure 3.4: Illustration of the method of determining drift time from a pulse as recorded in an FADC.

knowledge of how t and x are related. In practice this is not possible, and the aim is to achieve an x resolution of about 250 μm in the H1 environment.

Drift distance x is presumed to be related to drift drift time t by

$$x = v.(t - t_0) \tag{3.1}$$

where v is the drift velocity and t_0 is a constant time offset. This constant drift velocity assumption has been found to be reasonable at distances greater than 0.5 cm from the sense wire for muon tracks perpendicular to the cell face [33]. The values v and t_0 need to be found. Although the time t_0 is cell dependent and results from the combination of several factors: the time that the FADC stops sampling with respect to the interaction, time for a pulse to travel along the co–axial cable from the detector to the electronics rack, the time taken by a pulse to travel along the sense wires of a linked pair of cells and the region of varying drift velocity near to the sense wire, it is not necessary to consider each of these components individually but only to determine a global t_0 common to all the cells of the detector, and the relative t_0 values of each cell. The relative t_0 for each cell with respect to some reference cell is found by using test pulses which are sent out from the FADC at a fixed time to the cells at the detector. Each test pulse splits and takes two different routes through the detector. The shorter route is from the FADC to the first preamplifier and back, and the second is through the first preamplifier, along the linked cells and back to the FADC via the second preamplifier. By considering the difference in times of return of the first and second pulses for each cell pair in the detector it is possible to determine the relative t_0 values of each cell pair [37]. A factor to account for the time of flight of a muon between layers of the forward muon system is added. It remains to find the global t_0 having applied the cell to cell corrections, and to find the drift velocity v.

The method used for finding the t_0 and v is described in [38]. Because of the simple rectangular shape of the cell with a maximum drift distance for electrons of 6 cm, half of the muons passing through a cell should pass more than 3 cm from the sense wire, and half less than 3 cm from the sense wire, assuming an even illumination of the cell across its width. This makes it possible to find the drift time, t_{mid}, which is associated with muons passing 3 cm from the wire by taking the median drift time of many muons passing through a cell. The same procedure can be carried out for another drift distance, assuming for instance that one sixth of all muons pass within 1 cm of the sense wire and so calculating the time returned for a

muon passing 1 cm from the wire again by using the distribution of drift times for many muons traversing the cell. Having determined the drift times associated with two different drift distances, v and t_0 are themselves unambiguously determined. In general it is possible to check the linearity of the relationship between x and t from the distribution of drift times resulting from many muons incident on a cell. An even distribution of muons over the width of the cell should result in a flat, top–hat shaped distribution of drift times (with some smearing at the edges). It is the result of this type of study which supports the statement above that the relationship 3.1 is valid for drift distances x greater than about 0.5 cm.

Using the fact that track segments either side of the toroid are straight, it is possible to use the drift times for cells through which the muon passed to provide a measurement of t_{mid} independent of that above method, and also to assess the resolution in calculating x with this drift time to drift distance relationship [38].

By the above method, the drift velocity was found to be $4.93 \pm 0.04 \ cm\mu s^{-1}$, consistent with a measurement made in a test set–up in Manchester [33], the global t_0 was $216 \pm 5 \ ns$, though this would be slightly different for a different reference wire, and the resolution in x was about $300 \ \mu m$ averaged over the entire drift space.

3.4.2   Along the Wire Coordinate

A pulse originally formed at a particular point along a sense wire is propagated in both directions, and sampled at both ends of the wire pair. In travelling along the resistive sense wires and through the resistors of the z–link and the preamplifiers the pulse changes shape, becoming flatter with a more slowly rising leading edge and a longer tail (the theory of the development of these pulses is discussed in similar chambers in reference [39]). Sampling both pulses arising from one muon passing through a cell allows a comparison of the pulses which gives an idea of how far each of the pulses has travelled before reaching the preamplifier. This points to the coordinate along the wire of the muon, known as the (local) z coordinate.

Typical pulses seen are illustrated in figure 3.5. Supposing a muon to have passed through cell 1, which is linked to cell 2, the pulse sampled from cell 1 has travelled some distance along the sense wire of cell 1 whereas the pulse sampled from cell 2 has travelled the rest of cell 1, through the z–link and along cell 2. Usually a
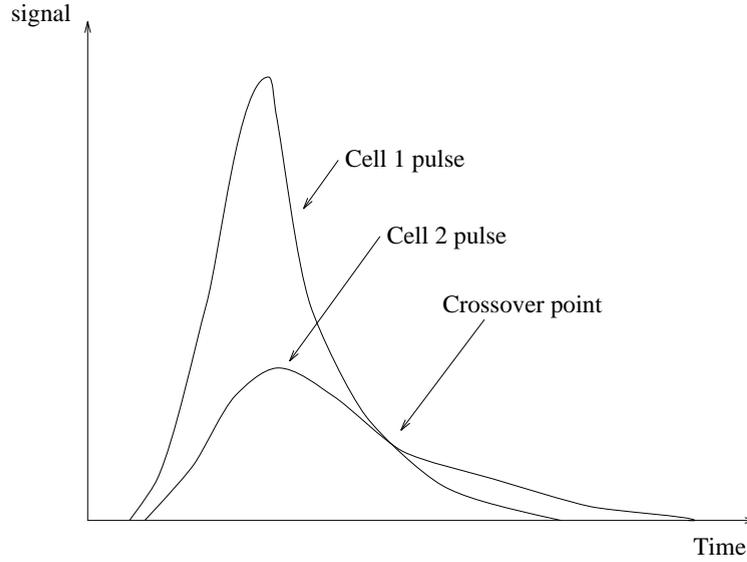
Figure 3.5: Representation of two pulses arising from a single muon passing through cell 1, where cell 2 is the z–linked partner to cell 1.

cross–over point is seen as shown in the figure, a time at which the pulse from cell 2 becomes greater than that from cell 1 on its longer tail, and this was found to occur on average about 8 time bins after the beginning of the pulses. In the light of this the integrated charge contained in the first 8 time bins of each pulse is calculated, and the two values obtained, Q_1 and Q_2, are combined in the expression

$$\mathcal{Z} = \frac{Q_1 - Q_2}{Q_1 + Q_2} \tag{3.2}$$

where z is now taken to be a function of $\mathcal{Z}$.

To determine the relationship between z and $\mathcal{Z}$, a test set–up was created using a z–linked pair of cells and a scintillator trigger which accepted cosmic muons passing through a region of length 4 cm of one of the cells [40]. For each position z_{trig} of the scintillator trigger along the cell, the pulses from around 3000 cosmic muons were analysed. Then for a single value of z there is a distribution of $\mathcal{Z}$ produced, the mean of which gives the mapping $\mathcal{Z} \to z$ and the spread of which is related to the resolution in reconstructing z.

The two z–linked cells used were of length 135 cm and had a resistance of 750 Ω. It was found that calculating Q_i as the sum of contents of the first 8 time bins of each pulse introduced a great sensitivity to the start time of each of the two pulses

with respect to a time bin start time, so that the effective z resolution calculated from $\mathcal{Z}$ would necessarily be poor. To counteract this the charge is integrated over 8 time bins worth of time (76.9 ns) after the drift time t associated with that pulse. This eliminated the quantisation effect. In rare cases where either of the two pulses is less than 8 time bins long, both pulses are integrated over the length of time of the shorter pulse.

Data were accumulated from 11 points, z_{trig}, along the cell, and the relationship between $\mathcal{Z}$ and z_{trig} is shown in figure 3.6. The points are consistent with a straight line where an error of 2 mm for each point is assumed, resulting from the estimated accuracy of positioning the trigger and the statistical errors. Using this linear relationship between $\mathcal{Z}$ and z gives a resolution of 3.5 cm in z, independent of z.

In order to extrapolate this result to apply to all cell pairs in the detector, which consist of cells of varying lengths, it is helpful to regard the preamplifier input impedances, the sense wires and the z–links as a chain of resistance 'lengths' as shown in figure 3.7. Supposing that a muon passes through cell 1 a fraction κ of the way from the z–link end to the preamplifier end of the cell, a value ρ can be assigned to the coordinate given by

$$\rho = \frac{R_{total}/2 - R_{preamp} - (1-\kappa)R_1}{R_{total}/2} \tag{3.3}$$

where R_{total} is the total resistance length of the chain, $R_{total} = 2.R_{preamp} + R_1 + R_2 + R_z$.

Now it is supposed that ρ and $\mathcal{Z}$ are related in the same way for all cell pairs of the detector. Both cells in the test set–up were of resistance 750 Ω, so that z and ρ were in this case related by

$$\rho = \frac{1115 - 200 - (1 - z/135).750}{1115} \approx 0.15 + 0.0050.z \tag{3.4}$$

which gives

$$\rho = 1.05\mathcal{Z} + 0.01 \text{ for } \mathcal{Z} > 0 \text{ and}$$
$$\rho = 1.05\mathcal{Z} - 0.01 \text{ for } \mathcal{Z} < 0. \tag{3.5}$$

At the moment, the expression used for the cell pairs in the detector is $\rho = 1.00\mathcal{Z}$, though there is provision for a constant factor to be included so that
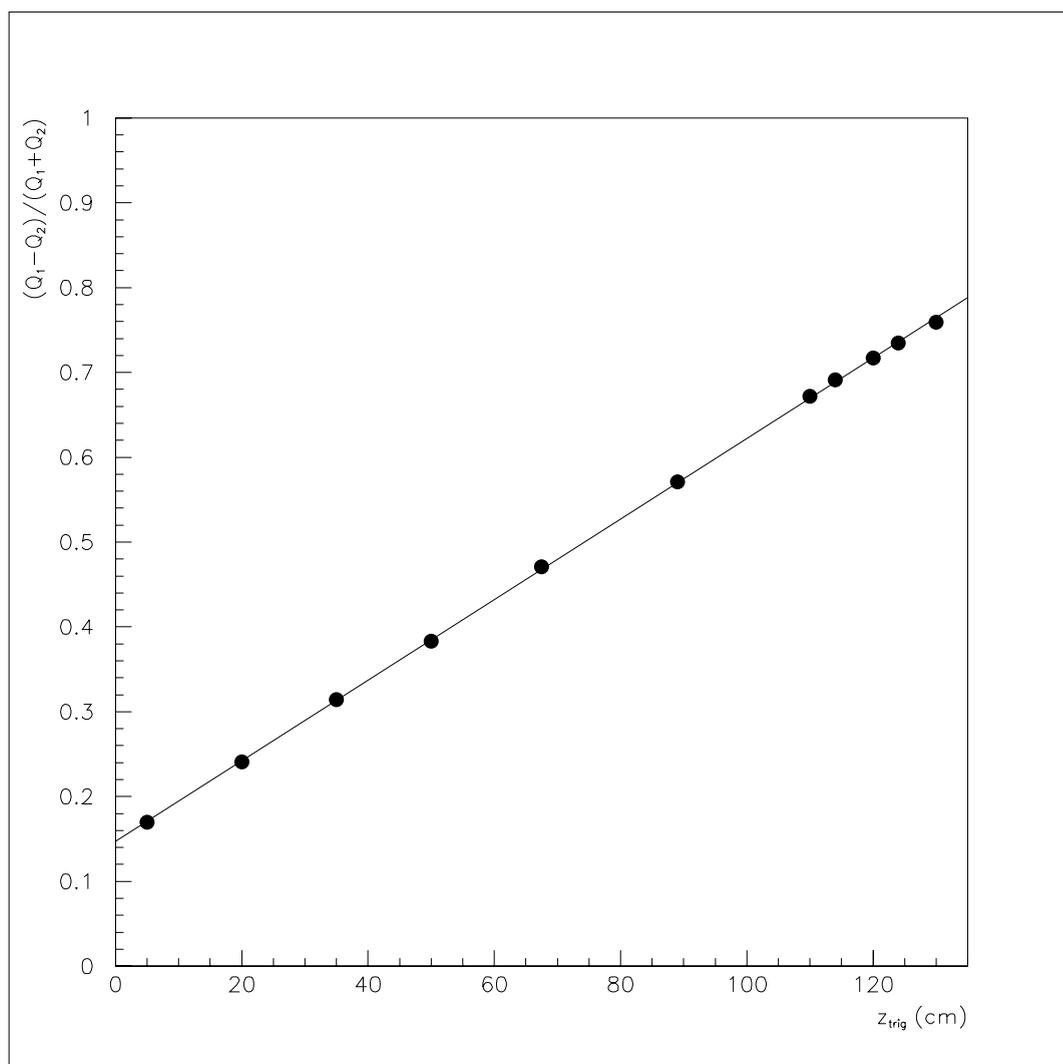
$$\rho = \frac{l_{\text{eff}}}{l}\mathcal{Z} \tag{3.6}$$

Figure 3.6: $\mathcal{Z}$ as a function of z_{trig}, where z_{trig} is the distance from the z–link end of the cell. The straight line fit is given by $\mathcal{Z} = 0.0048z + 0.15$.
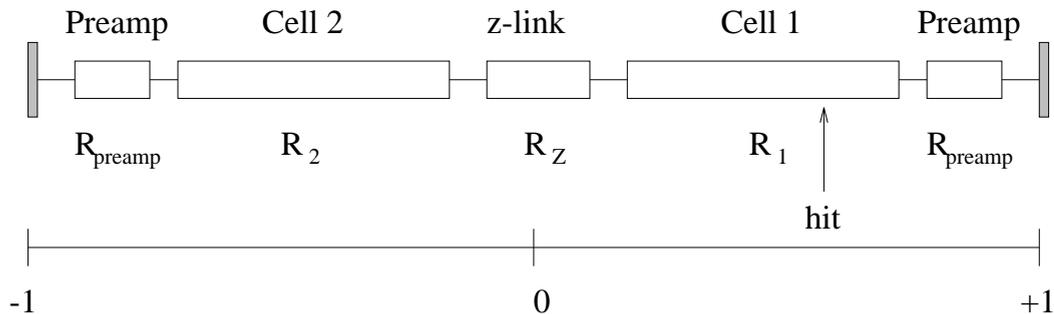
Figure 3.7: Considering the preamplifier impedances, sense wire resistances and z–link resistance as having a length given by their respective resistances, a scale can be formed $-1 < \rho < +1$ as shown, which is linear in the resistance length. Then the position of the hit can be expressed in terms of ρ.

where l_{eff}/l takes a value close to 1. The actual z coordinates are then derived from ρ given the resistances of the cells of the cell pair. The resolution of 3.5 cm in z corresponds to a resolution of 0.017 in ρ, that is, 0.85% of the total equivalent wire length as represented in figure 3.7.

3.5   Octants and Layers

The six layers of the Forward Muon Detector are formed from a total of 1520 cells. Each layer consists of eight octants which are fixed together on an aluminium 'door–frame', alternately on each side with a slight overlap so that there is no dead space between octants. The octants themselves are identical within a layer and comprise two planes of cells either side of an 'octant frame', each plane being displaced from the other by half a cell width. This displacement cuts out the dead space between each cell and removes the ambiguity of the calculated drift coordinate which arises because the drift time alone does not indicate on which side of the sense wire the muon passed. The mounting of cells onto an octant frame to form a layer of two planes is shown in figure 3.8.

To describe the orientation of cells on an octant frame, a local coordinate system is used whereby the y–axis ($x = 0$) runs radially from the centre of the beam–pipe along the octant centre and the (x, y, z) coordinate system, with z being the H1 z–axis, is right–handed. The two types of layers, θ and ϕ, have different orientations
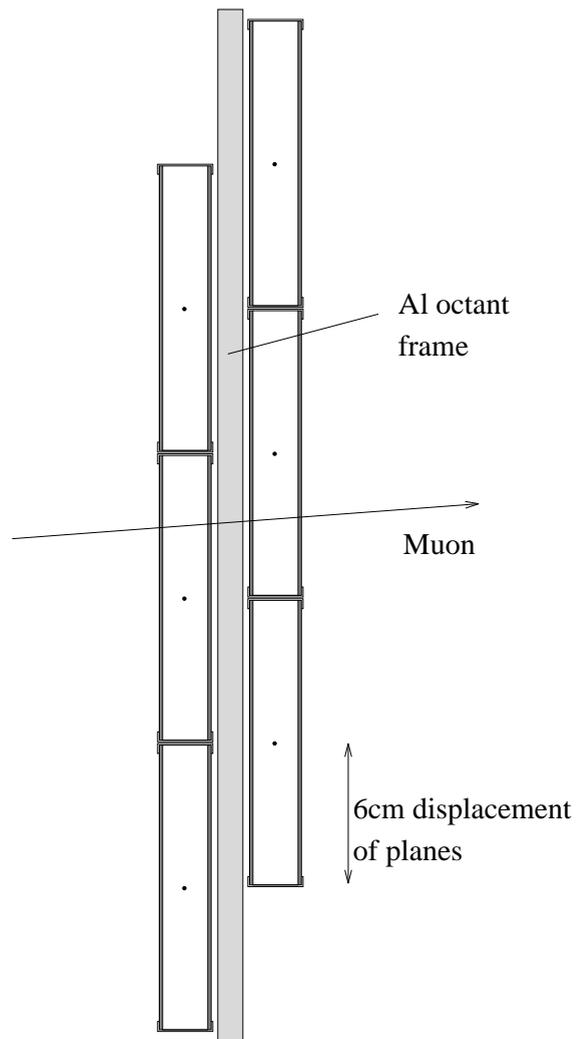
Figure 3.8: Cross–section of cells mounted on an octant frame showing the displacement of the two planes by half a cell width (6 cm).
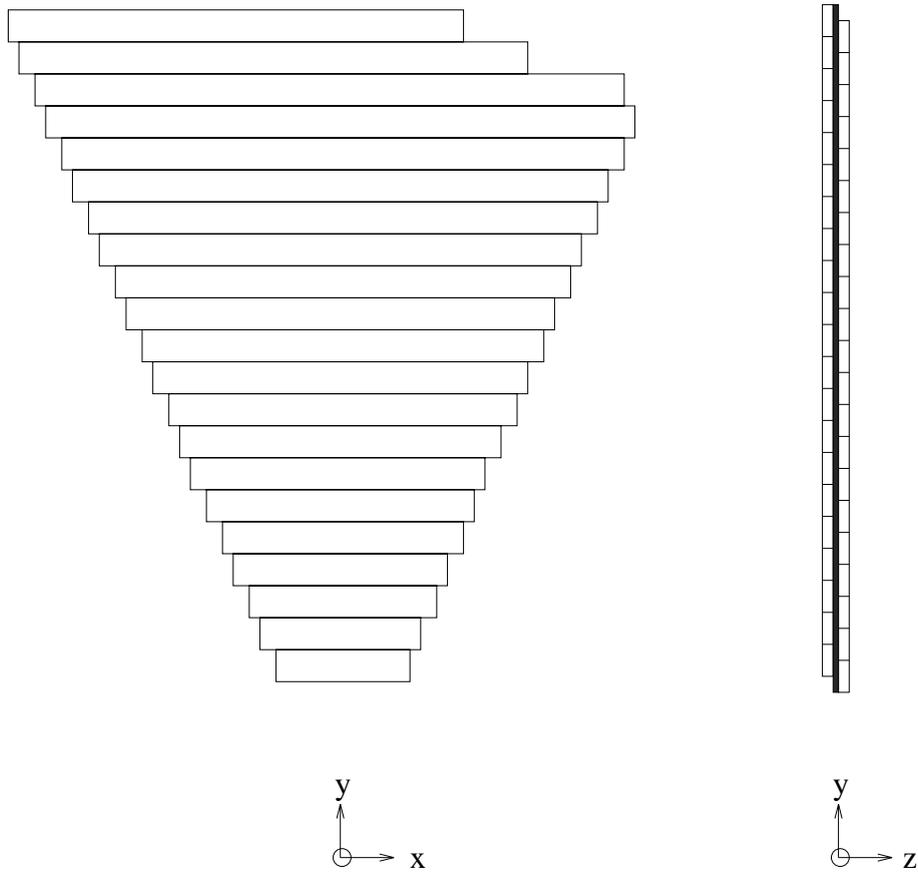
Figure 3.9: Mounting of cells to form a θ–octant. Numbering the cells from 1 to 21 (inner to outer), θ_1 contains cells 1–12, θ_2 contains 1–14, θ_3 2–19 and θ_4 2–21.

of cells on the octant frames as shown in figures 3.9 and 3.10. Since the drift coordinate for a cell is much better determined than the along the wire coordinate, the orientation of cells on a θ–octant allows a more accurate local y coordinate to be determined, which is approximately equivalent to the determination of the polar angle θ. Similarly a ϕ–octant allows better determination of the local x coordinate.

Cells are located on the octant frames by dowel rods so that their positions with respect to the frames are accurate to within about 50 μm. Each cell is partnered with an adjacent cell in the same plane except each of the ϕ–octants contains one single un–linked cell. A total of 1520 cells then corresponds to 1536 channels to read out. The preamplifiers are also attached to the octant frames and then the signals are transferred to the electronics racks containing the FADC cards via coaxial cables. Each preamplifier deals with eight channels and each FADC with two preamplifiers.
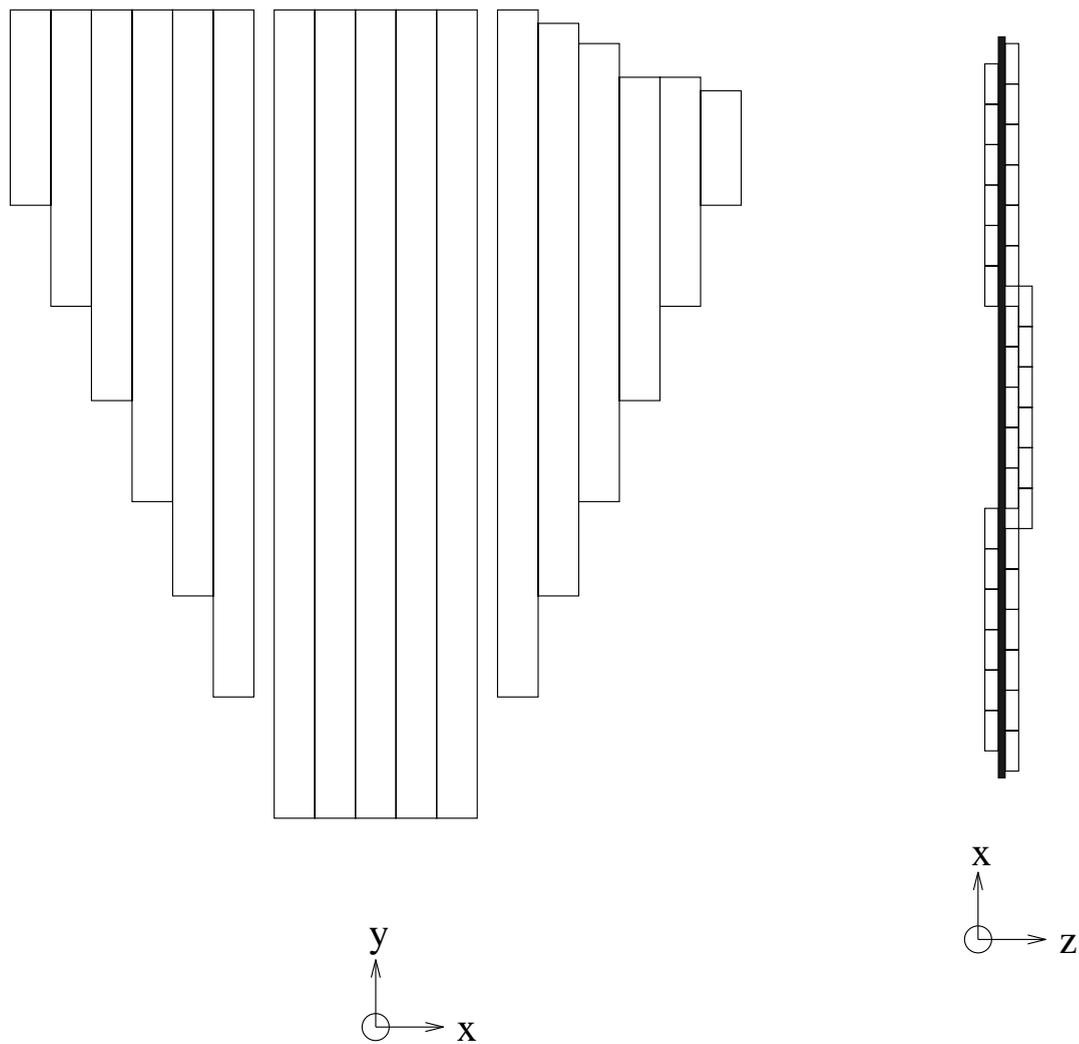
Figure 3.10: Mounting of cells to form a ϕ–octant. Layer ϕ_2 contains all cells shown, whereas ϕ_1 does not contain the outermost 2 cells of each plane on each side (positive and negative x).

A rack governed by one scanner contains 16 FADC cards so that the entire forward muon system is catered for by 6 racks of FADC's.

3.6   Alignment

Having used the space–point determination described above to find the point at which a muon passed through an octant in local coordinates, the transformation to H1 global coordinates needed for associating points to form tracks is dependent on the exact alignment of the octants of the different layers with respect to one another. The problem of determining the positions and orientations of all the octants within the system to a sufficient accuracy so as not to compromise the best achievable momentum resolution determined by the position resolution of the cells themselves is the subject of a study in reference [26]. In particular it is necessary to know the octant positions to about 50 μm in the coordinate corresponding to the drift direction in the cells, and to about 1 mm in z. This is beyond the accuracy of the positioning of the octants, so that they must be measured. A physical survey is restricted because of the lack of access to the detector, though some information will be gained from such a survey which will complement the method of alignment using 'beam halo' muons. These are muons which arise from proton collisions with gas in the beam–pipe or with the beam–wall and travel almost parallel to the beam thereafter. Using this prolific source of high energy muons with the toroid field off at times of no collisions allows alignment measurements of the octants to sufficient accuracy by assuming the straightness of the muon tracks.

3.7   Reconstruction of Tracks

Track reconstruction identifies muon tracks in the Forward Muon System and associates a momentum and direction with them, starting from the space–points in H1 coordinates of all hits seen in an event. Typically an event contains many spurious hits from parts of the proton remnant scattering off beam–pipe components into the detector, and also from synchrotron radiation.

A track consists typically of twelve hits, two in each of the double layers, though reconstruction is possible with less. A three stage procedure converts the space–

points defined by hits into tracks: the association of hits in the double planes of
each layer into pairs, the association of pairs into track segments, and finally the
association of segments pre– and post–toroid to find tracks and provide a momentum
measurement. Track segments are tracks on one side of the toroid only, which are
therefore straight.

The pair finding uses the half cell stagger of the two planes in a layer to resolve the
ambiguity in drift coordinate, taking the pair of hits that best points to the vertex.
In some cases hits may remain unpaired, in which case both possible coordinates
are kept and considered in the segment finding procedure.

To find a segment, each pair of hits in a θ–layer is used to define a cone which is
extrapolated to the associated θ–layer on the same side of the toroid. This defines
an area on the associated layer in which hits could form a segment with the original
pair. The pair of hits in the associated layer producing the best segment fit is
chosen. Using the two pairs, suitable hits in the ϕ–layer are sought which fit into
the segment. Finally the segment is defined by a best fit to all the points that have
been found to belong to it.

Each found track segment defines a straight line in space which represents the
possible path of a muon on one or other side of the toroid. To construct a full
track, that is, the path of a muon which passes through the toroid, a pre–toroid
segment and a post–toroid segment must be linked together and the path of the
muon through the toroid inferred from these two segments. As a first step an
attempt is made loosely to form pairs of segments, each pair being one pre– and
one post–toroid segment, in which both segment tracks could have been formed by
the same muon passing through the toroid. To do this all straight lines defined by
segments are extrapolated to the centre plane of the toroid (the plane defined by
$z = 790$ cm in H1 coordinates). A pre–toroid segment is paired with a post–toroid
segment if the points of incidence on this plane are sufficiently close to each other.
Now unpaired segments are rejected and each pair is considered as possibly forming
a full track.

The next, more detailed step, attempts to recover the paths of muons and their
momenta. This involves reconstructing the path of the muons through the toroid
in which it suffers energy loss and is bent in the magnetic field. Each pair of
segments is taken in turn and a 'momentum scan' is performed: it is assumed that

the pre–toroid track segment is the track left by a muon entering the forward muon system with momentum $p_{assumed}$, and then the path that that muon would have taken through the toroid is calculated (taking magnetic bending and energy loss into account but not multiple scattering). In this way a post–toroid segment has been inferred which can be compared to the real post–toroid segment which is the partner of the pre–toroid segment. The comparison is made quantitive by a χ^2 value, a lower χ^2 representing a better compatibility of the inferred and the real post–toroid segment. This procedure is repeated for 50 different values of $p_{assumed}$ — this is the 'momentum scan' — so that a plot of χ^2 as a function of $p_{assumed}$ is built up. If there is no value of $p_{assumed}$ which yields a χ^2 below a pre–set threshold, the pair of segments is deemed not to form a full track at all. Otherwise the value of $p_{assumed}$ with the smallest associated χ^2 is taken as an estimate of the momentum of the muon, $p_{estimate}$. This value $p_{estimate}$ is improved upon by using the two χ^2 values corresponding the two $p_{assumed}$ values either side of $p_{estimate}$, and the χ^2 from $p_{estimate}$ itself, to form a quadratic function, $\chi^2(p)$. The minimum of this function is the final momentum taken, p_{rec}, and the second derivative at the minimum provides an estimate of the uncertainty of this reconstructed momentum.

After repeating the above procedure for every pair of segments, it is still possible that a single segment is a part of more than one reconstructed full track. In which case all but one of these tracks is rejected, the one being chosen because its reconstructed momentum had the smallest associated χ^2 value.

Any full tracks which remain are assumed to have been the paths of muons passing through the forward muon system, including the toroid, and the momentum of each of these muons is taken to be p_{rec}.

The ability of the forward muon system to reconstruct the momenta of muon tracks is discussed and assessed in the next chapter.

Chapter 4

Potential for Physics of the FMD

4.1 Introduction

In this chapter the forward muon detector is considered both as an independent muon spectrometer and as a device for identifying muon tracks in the forward tracker (FTD). The ability of the system to reproduce the momentum and track position and direction of a muon is determined and discussed. To assess the potential for linking to tracks in the forward tracker, the performance of the FMD as an independent system is combined with the results of a study of energy loss and multiple scattering undergone by a muon passing from the central region of the H1 detector to the FMD. This is effectively testing the ability of the FMD to reconstruct muon tracks and momenta in the forward tracker region.

Finally, the identification of J/ψ particles via their decay into a muon pair is used as a testing ground for the forward muon spectrometer. The rôle of the FMD in this identification is discussed and the potential for reconstructing the final state muons is assessed by investigating the spectrum of muons in the final state and the spectrum of other tracks in the FTD from which the muon tracks must be distinguished.

To assess the potential performance of the forward muon detector, a simulation program, H1SIM [41], is used which contains a material description of the detector and utilises the GEANT program [56] to simulate physical processes which particles undergo in the media. The input are particle 4–vectors, and the output are data banks equivalent to the output data banks from the H1 detector, resulting from the

tracking of the input particles through the detector. It is then possible to treat this output exactly as for real data and, for example, reconstruct muon tracks in the forward muon system. This provides a useful method for testing the detector since it is possible to compare the reconstruction output with the tracks of the simulated particles passing through the detector, a record of which can be kept.

4.2   Simulation of the FMD

The aim of the simulation of the detector is to produce the detector response to an input event. This input event is always in the form of particle momentum 4–vectors which are generated at some origin, usually the H1 vertex. For physics studies the input is the result of some monte carlo (MC) generator. The relationship between the monte carlo generator output, which is in the form of particle 4–vectors, and the detector response is complex, but correct simulation of the detector allows a direct comparison of results from a monte carlo generator and from real events, so testing the monte carlo generator in a way which would otherwise not be possible. In this study, the simulation is initially used to test the response of the detector, in particular the forward muon detector, to muons which are created very near the event vertex in the vertex region in the centre of the H1 detector. In this case the input event is a single muon with a given momentum and direction, and the output is the detector response banks and a record of the track at various points in the detector. This track record could be called the 'MC truth', and its comparison to the reconstruction of the simulated detector response gives an idea of the expected detector performance.

Detector simulation works in three separate stages: the 'GEANT' step, the 'DIGI' step and the 'TRIGGER' step. The GEANT stage tracks particles through the detector in which they undergo the relevant physical processes. For a muon these are decay in flight, multiple scattering, ionisation and delta rays production, Bremsstrahlung, electron–positron pair production and nuclear interactions [42]. The input to this stage are the initial particle 4–vectors and a description of the physical materials of the detector. Particles are then tracked in steps through the detector, and a record is kept whenever they pass through a sensitive region, a region in which particles can be detected. To define the geometry of the detector, H1 is split into sub–detector volumes, including the 'FWFE' volume which contains the

forward muon system geometry description including the drift chambers, toroid and the beam–line description for those parts of the beam line and its magnets which are situated within the forward muon system. Each cell of the drift chambers is included as a rectangular box containing the drift gas, having front and back walls of 1.6 cm thick PCB supported at the sides by 0.7 mm thick aluminium supports. They are mounted according to design specifications and do not reflect the misalignments of the real detector. The sensitive regions are the insides of each cell, so that if a particle is tracked by GEANT through the forward muon system a record is kept every time it passes through a cell. A representation of the FWFE volume is shown in figure 4.1.

The size of each step made by the particle passing through the toroid is limited by the physics processes. Essentially the particle steps to the next interaction of a sort mentioned above, or to the next material boundary. Magnetic bending and continuous energy loss are also simulated and these can also limit the step size. The decision as to which physics process the particle will next undergo results from a calculation of an interaction length for each of the above processes which is dependent upon the medium and the process itself. The number of interaction lengths for a given process that the particle will travel before undergoing the process is decided at the beginning of the journey and is a randomly generated quantity with an exponential distribution [42] (interaction length is analogous to half–life).

Entry and exit points of particles to the sensitive regions of the detector and the characteristics of the particles at those points are the inputs to the DIGI stage of H1SIM, which simulates the detector output in response to these particles. In response to a muon passing through a cell of the forward muon system, two charges and a time are returned which correspond to the integrated charge at each end of the sense wire and the drift time. Producing charges and times from space–points is exactly the opposite process of the space–point reconstruction explained in the previous chapter, and the DIGI step of H1SIM uses precisely the inverse formulae. To simulate the resolution of the cells, the DIGI step includes a random smearing of charges and time which produce the desired uncertainties, 250 μm in the drift coordinate and 1% of the total cell pair resistance length in the along the wire coordinate.

The output from the DIGI step is in the same form as the detector response from real events and is ready for reconstruction. For the forward muon system it is
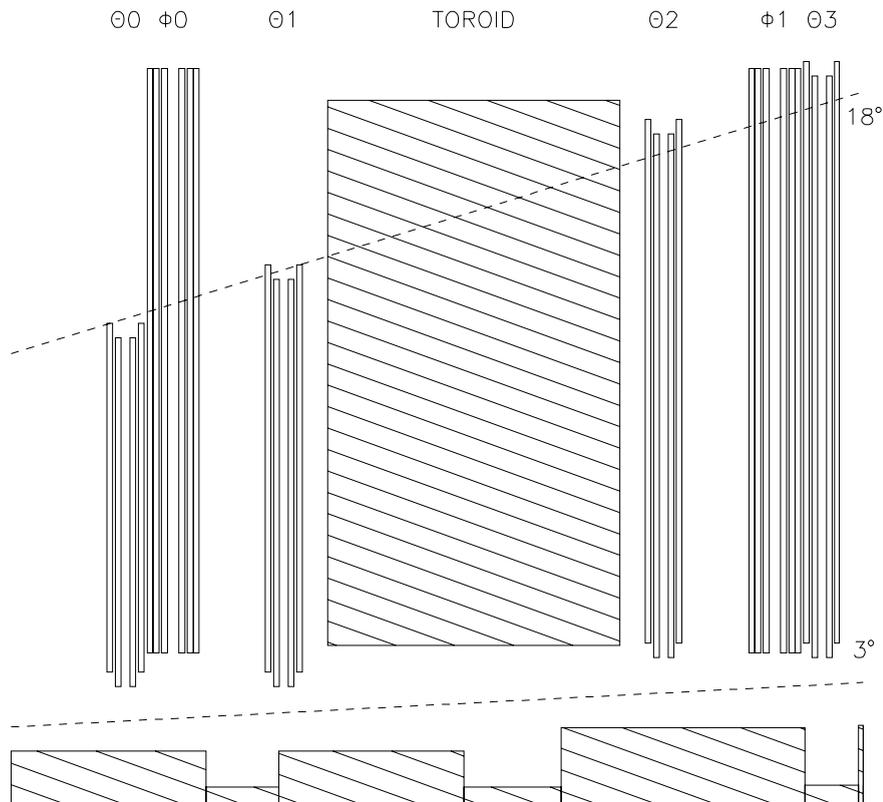
Figure 4.1: An r–z projection of the FWFE volume as described in the geometry description of H1SIM. Individual cells are not shown. The diagram extends from $z = 600$ cm to $z = 950$ cm with respect to the H1 vertex.

possible to compare the reconstructed tracks with the tracks of the simulated muons and so test the resolution of the system as a function of the resolution of the cells.

The TRIGGER step simulates the trigger response to a simulated event and is not relevant to this study.

4.3 FMD Performance

In this section the ability of the forward muon system to act independently to reconstruct the momentum, direction of flight, and point of entry to the FMD of a muon is discussed.

Whilst the direction of flight and point of entry to the forward muon system can be determined to an accuracy given by the ability to reconstruct track segments before the toroid, the momentum resolution is very much limited by the iron toroid in which a muon suffers multiple scattering and energy loss as well as the desired bending in the magnetic field. Since muons being produced near the H1 vertex enter the system in a plane of approximately constant ϕ, the bending of the muons in the toroidal field is measurable, to a good approximation, by the change in polar angle θ of the muon in passing through the toroid.

Taking the path of a muon through the toroid to be 1.2 m, and a field of 1.6 T, the change of θ in the direction of flight of the muon due to the field is given approximately by $\Delta\theta = 0.58/p$, where p is the muon momentum in GeV and θ is measured in radians. The contribution to $\Delta\theta$ due to multiple scattering in the iron of the toroid is to be added to the above and has an approximately normal distribution with standard deviation given by $\sigma_{\Delta\theta}^{ms} = 0.13/p$ and mean zero [28]. Thus it is impossible, even with perfect resolution in reconstructing track segments, to have an inverse momentum resolution better than about 22%:

$$\frac{\sigma_{1/p}}{1/p} > \approx 0.22 \ . \tag{4.1}$$

In the above, energy loss in the toroid has been neglected. This is almost entirely due to ionising collisions for the magnitude of momenta considered here (approximately $1 \ GeV < p < 100 \ GeV$), and much of the momentum loss is due to rather few high energy collisions leading to a statistical fluctuation in the total amount of en-
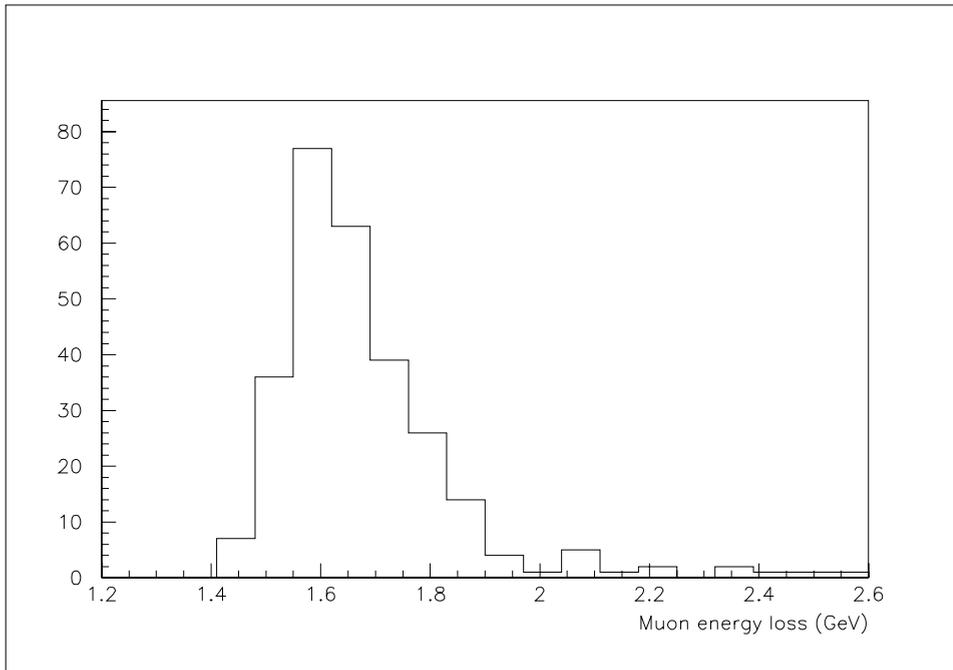
Figure 4.2: Energy loss of a muon of starting energy about 3 GeV in passing through the toroid. The muons were simulated randomly in θ and ϕ.

ergy loss. The reconstruction assumes a mean energy loss given by the Bethe–Bloch formula [28] in its extrapolation through the toroid, and so necessarily miscalculates the actual energy loss. However, this miscalculation is well within the momentum resolution limit given by equation 4.1 and so can be ignored as a contributing factor to the resolution. The absolute energy loss does though impose a minimal reconstructable momentum that a muon entering the forward muon system can have. Below this value the muon is stopped in the toroid or has so little momentum that the pre– and post–toroid segments cannot be identified as one track. Energy loss is weakly dependent on energy for minimum ionising particles, and the loss in the toroid for muons entering with momentum of about 3 GeV is shown in figure 4.2. The tail of energy loss is a sign that it is mainly due to a small number of high energy transfers. It becomes practically difficult to reconstruct tracks of muons with less than about 2.25 GeV momentum, and this is the lowest value that is taken in the momentum scan made in the attempt to reconstruct tracks from segments.

To assess the effects on a muon passing through the forward muon system, muons have been generated at the vertex and allowed to pass through the simulated de-
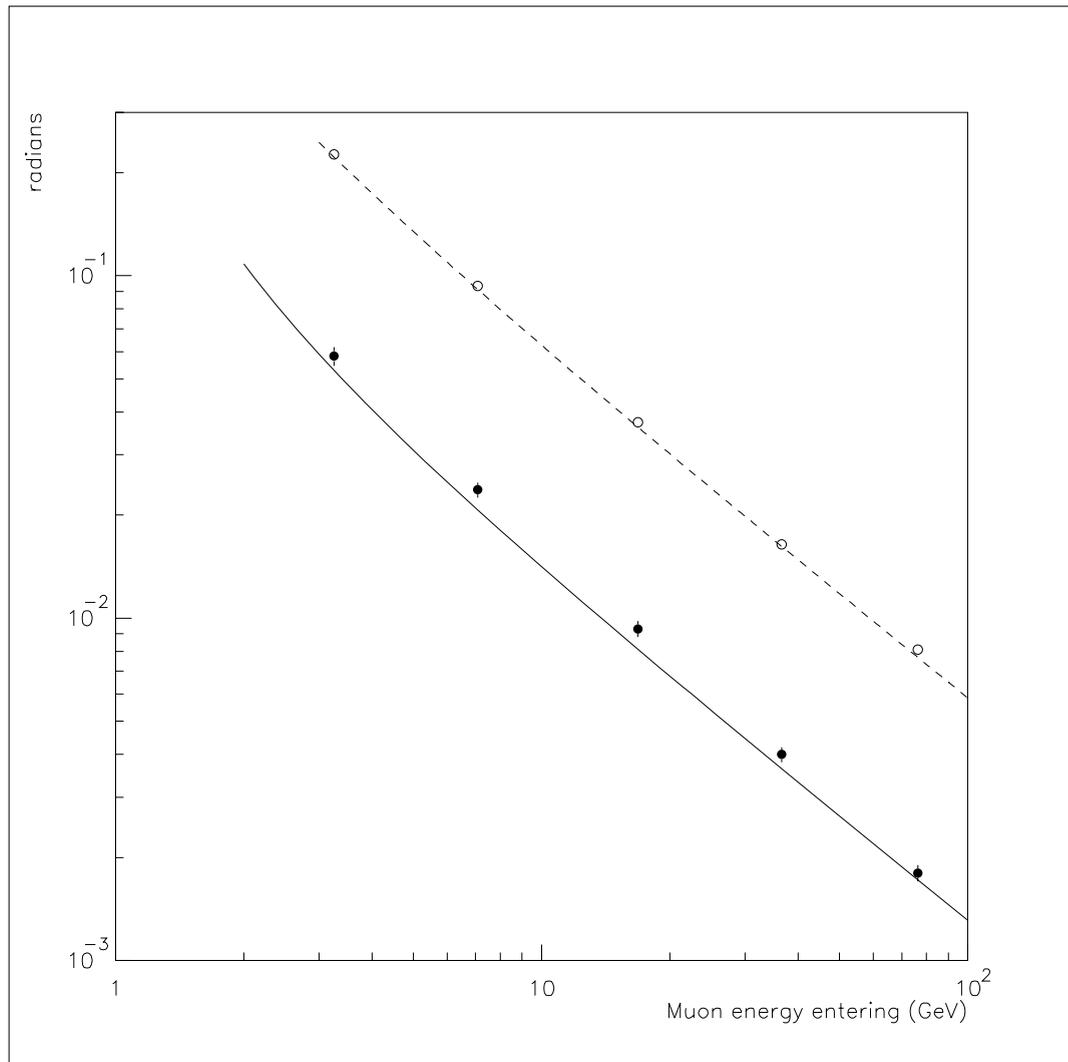
Figure 4.3: $\Delta\theta$ (open points) and $\sigma^{ms}_{\Delta\theta}$ (closed points) from simulated muons with the predictions $\Delta\theta = 0.58/p$ (dashed line) and $\sigma^{ms}_{\Delta\theta} = 0.13/p$ (full line).
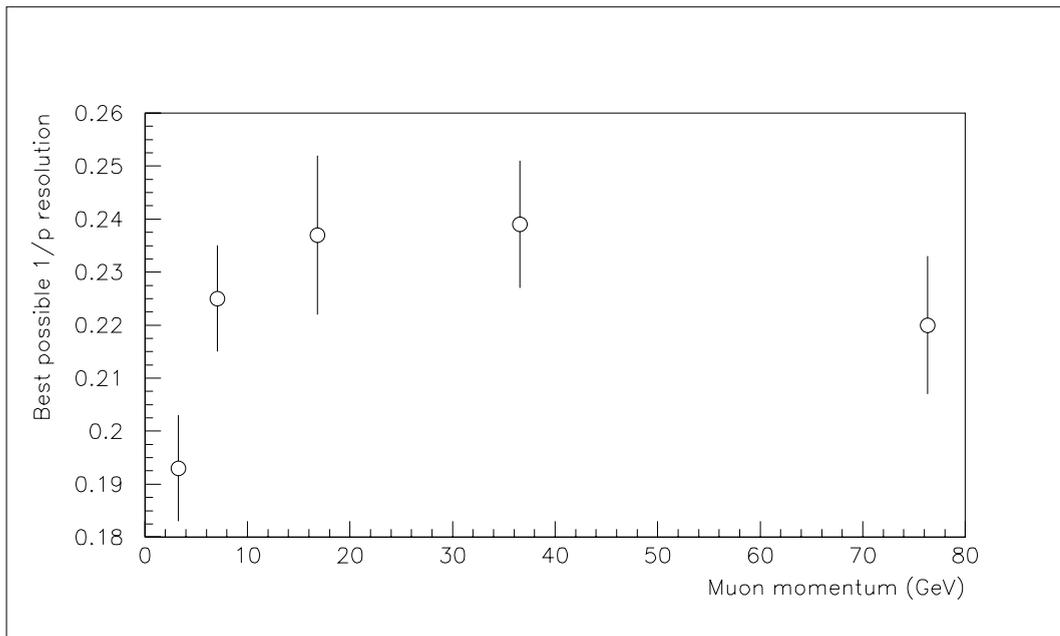
Figure 4.4: The best possible inverse momentum resolution, $\frac{\sigma_{1/p}}{1/p}$, as a function of muon momentum, limited by multiple scattering in the toroid.

tector. The directions and starting momenta of the muons can be specified, the direction in terms of polar angle θ and azimuthal angle ϕ. For plot 4.2, muons were generated randomly in ϕ and in the range $3° < \theta < 17°$, effectively the whole range covered by the forward muon system. Comparing the track record of the muons pre– and post–toroid indicates the energy loss. In figure 4.3 the change in θ, $\Delta\theta$, and the width of the distribution of $\Delta\theta$ due to multiple scattering are shown for muons of particular momenta. The lines shown are the calculated $\Delta\theta$ and $\sigma^{ms}_{\Delta\theta}$ as above where the momentum is taken to be the average momentum of the muon in the toroid rather than the initial momentum to account, to first order, for the energy loss. Here the agreement can be seen to be rather good, the discrepancy in $\sigma^{ms}_{\Delta\theta}$ is within the accuracy of the calculation leading to the result $\sigma^{ms}_{\Delta\theta} = 0.13/p$.

Using the results of figure 4.3 leads to the revised values for the best possible inverse momentum resolution of the forward muon system shown in figure 4.4. Essentially these are the ratios $\sigma^{ms}_{\Delta\theta}/\Delta\theta$, but a correction is made so that p now corresponds to the muon momentum on entry to the forward muon system rather than in the centre of the toroid. These values would represent $\frac{\sigma_{1/p}}{1/p}$ in the case of perfect track segment reconstruction.

The ability to find the θ direction of a track segment is independent of muon momentum, so that the error in reconstructing $\Delta\theta$ due to the limited resolution of the drift cells is independent of momentum. This error should be added in quadrature to the uncertainty in $\Delta\theta$ due to multiple scattering to give the total uncertainty in momentum determination. It is clear that the cell resolution, or equivalently the ability to reconstruct a track segment, becomes the limiting factor at high momenta where the magnetic bending and multiple scattering of the muon in the toroid is small, and so $\sigma_{\Delta\theta}^{ms}$ becomes small compared to $\sigma_{\Delta\theta}^{rec}$, where $\sigma_{\Delta\theta}^{rec}$ is the error in reconstructing $\Delta\theta$.

In considering the ability of the forward muon system to reconstruct track segments it is helpful to use the local coordinate system of the octant through which the muon passes, and to introduce an angle, η, corresponding to the difference in azimuth between the octant axis and the point of incidence of the muon (see figure 4.5). Then a segment can be parametrised in the form

$$
\begin{aligned}
x &= A_x(z - z_\phi) + B_x ~, \\
y &= A_y(z - z_\phi) + B_y ~,
\end{aligned}
\tag{4.2}
$$

where z_ϕ is the z coordinate at the centre of the ϕ–layer of the segment. The segment is formed by, in turn, hits in two planes of a θ–layer, two planes of a ϕ-layer and two planes of a second θ–layer and is a best fit straight line to all these points of incidence. In practice though, this means that the values A_x and B_x are almost entirely determined by the hits in the ϕ–layer, and A_y and B_y by the hits in the θ–layers since the drift coordinates of the cells are so much more accurately determined than the along the wire coordinates. Thus the accuracy in reconstructing a segment depends only on the resolution in finding the drift coordinate, σ_{drift}, and not at all on the along the wire coordinate which is only important in associating hits to form segments. The exception to this case is when there are less than two ϕ–layer hits associated with the segment.

Assuming a full complement of six hits on the segment, the values B_x and B_y can be reconstructed with a resolution of about $0.7\sigma_{drift}$ and $0.4\sigma_{drift}$ respectively. This is then the accuracy to which the point at which the muon passed through the ϕ–layer is known. The separation of the two θ–layers (65 cm) is much greater than the separation of the two planes of the ϕ–layer (2.42 or 3.42 cm, see figure 3.10), and this more favourable lever–arm means that A_y is more accurately known than A_x by a factor of more than 25.
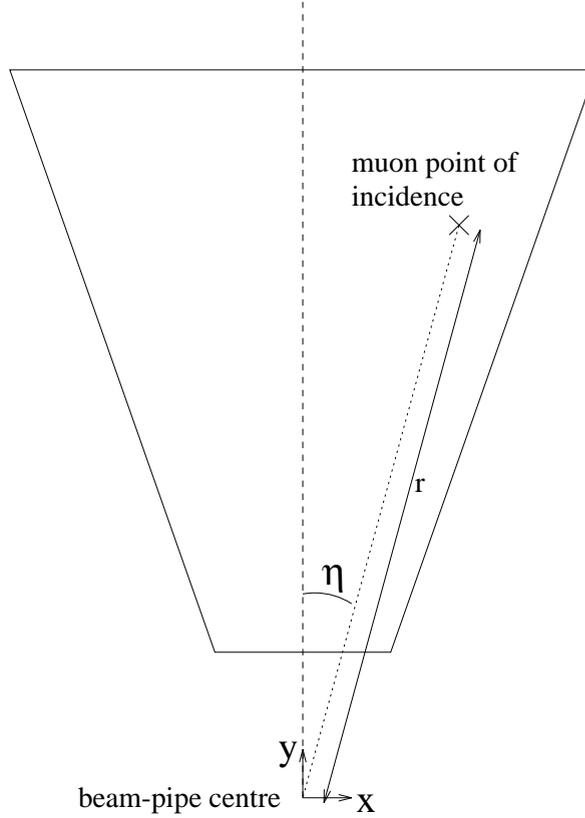
Figure 4.5: Local coordinate system for an octant. H1 z coordinate (ie the beam–pipe direction) is normal to the page. The distance r is the radial distance from the beam–pipe to the point of incidence.

To determine the muon momentum it is the polar angle θ of the segment, approximately $\frac{dr}{dz}$, which must be reconstructed, and this is given by

$$\theta = \sin\eta A_x + \cos\eta A_y \qquad (4.3)$$

so that the resolution in reconstruction of the θ coordinate of the direction of flight of the muon is

$$\sigma_\theta^2 = \sin^2\eta \; \sigma_{A_x}^2 + \cos^2\eta \; \sigma_{A_y}^2 \; . \qquad (4.4)$$

Even as close to the octant axis as $|\eta| = 1.5°$, the determination of A_x becomes the dominant term, thus it is the ϕ–layer drift coordinates reconstruction that limits the ability to reconstruct the θ coordinate of the segment, and so in turn limits the momentum resolution beyond the effects of multiple scattering.

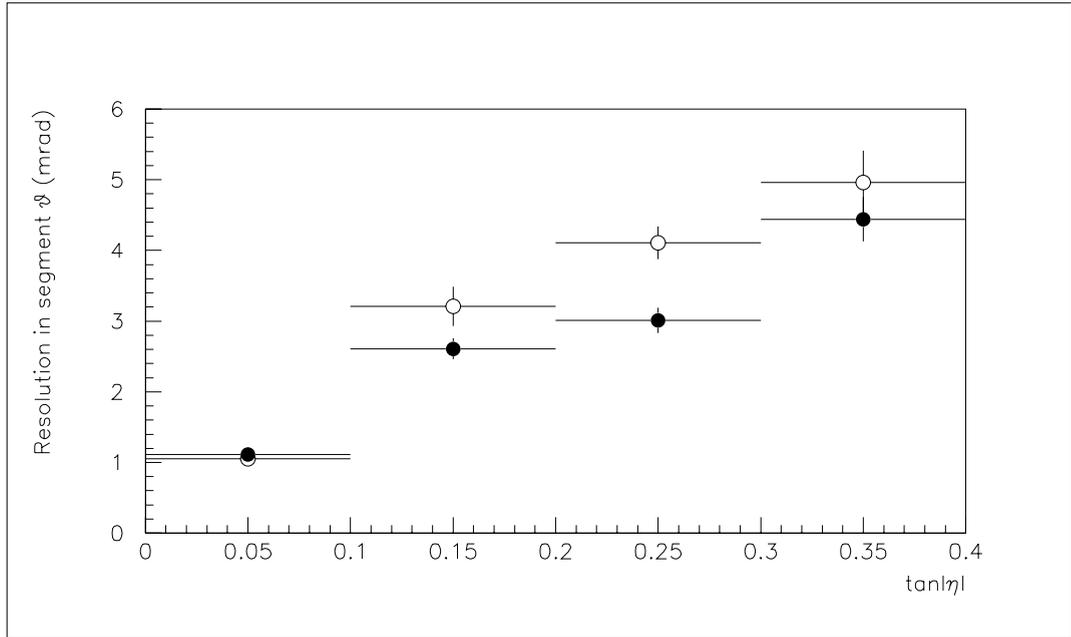A quantitative study that does not require any of the above simplifications and

Figure 4.6: Resolution in reconstructing the θ coordinate of the direction of flight of a muon entering the forward muon system as a function of $\tan |\eta|$, where η is the azimuthal angle of the point of incidence of the muon with respect to the octant axis. Two drift coordinate resolutions for the cells are assumed: $\sigma_{drift} = 250 \mu m$ (closed points) and $\sigma_{drift} = 350 \mu m$ (open points).

assumptions can be made using the simulation program H1SIM. By generating muons at the vertex of H1 with specified 4–momenta, and simulating their passage through the H1 detector before entering the forward muon system, the 4–momentum spectrum of muons entering the forward muon system reflects that of real muons originating from near the event vertex. Having simulated the forward muon detector output the reconstruction program is run and the result compared with the simulated tracks. In figure 4.6 the actual θ coordinate of the direction of flight of the muons entering the forward muon system is compared with the equivalent reconstructed coordinate to give the resolution in reconstructing the θ coordinate of a track segment. As argued above, σ_θ is seen to be strongly dependent on $|\eta|$ and also on the drift coordinate resolution of the cells, σ_{drift}, for which two values have been assumed: the nominal 250 μm and 350 μm. Altering the resolution of the along the wire coordinate by 50% was not found to significantly change σ_θ.

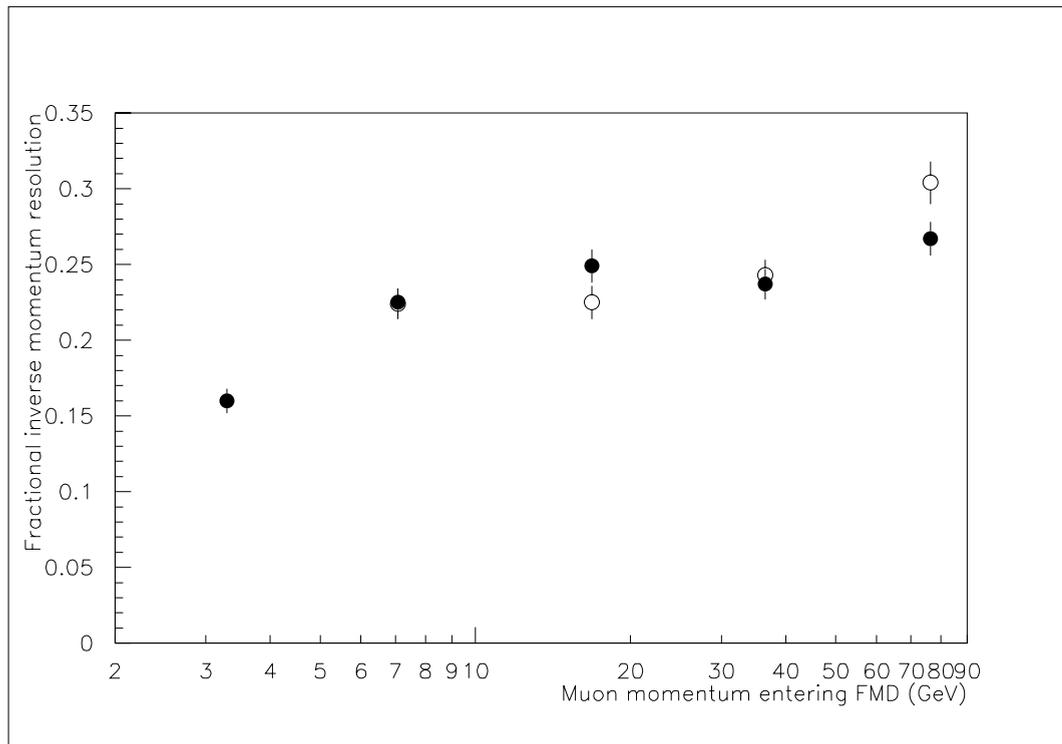A similar argument can be constructed leading to the result that the resolution

Figure 4.7: Fractional inverse momentum resolution, $\frac{\sigma_{1/p}}{1/p}$, as a function of momentum, p. Two drift coordinate resolutions for the cells are assumed: $\sigma_{drift} = 250\mu m$ (closed points) and $\sigma_{drift} = 350\mu m$ (open points).

in reconstructing the azimuthal ϕ coordinate of the direction of flight of a muon is almost independent of η (it is approximately proportional to $\cos\eta$). It is a feature of cylindrical polar coordinates that σ_ϕ is inversely proportional to the θ coordinate of the direction of flight. The above study with simulation of the forward muon system yields $\sigma_\phi \approx 0.014/\theta$ radians.

The fractional inverse momentum resolution, $\frac{\sigma_{1/p}}{1/p}$, where p is the momentum of the muon on entering the forward muon system, is shown as a function of p in figure 4.7. Muons were generated evenly over the detector area so that, in particular, dependence on the angle η defined above is not shown. Two sets of points are shown, one corresponding to a cell drift coordinate resolution of 250 μm and one to 350 μm. The inverse momentum resolution is not noticeably changed by a 50% increase in the resolution of finding the along the wire coordinate of hits in cells. Most obvious is the expected result that $\frac{\sigma_{1/p}}{1/p}$ appears limited only by multiple scattering at lower momenta (cf. figure 4.4) and only at higher momenta does it begin to rise as a result

of the limited ability to reconstruct the direction of flight of the muons.

If the reconstruction assumed the relationship $p = 0.58/\Delta\theta$ as indicated in figure 4.3, and used the two independently calculated θ directions of the pre–toroid and post–toroid segments of the track to find $\Delta\theta$, then the expected resolution $\frac{\sigma_{1/p}}{1/p}$ would be rather worse than that indicated in figure 4.7. More precisely, the relationship $\frac{\sigma_{1/p}}{1/p} = \sigma_{\Delta\theta}/\Delta\theta$ would hold, and $\sigma_{\Delta\theta}$ could be expressed

$$\sigma_{\Delta\theta} = \left((\sigma_{\Delta\theta}^{ms})^2 + (\sigma_{\Delta\theta}^{rec})^2\right)^{\frac{1}{2}} \ . \tag{4.5}$$

The values obtained for $\sigma_{\Delta\theta}^{ms}$ and $\sigma_{\Delta\theta}^{rec}$ are shown in figures 4.3 and 4.6. Using these values, and assuming $\sigma_{drift} = 250\mu m$, would give $\frac{\sigma_{1/p}}{1/p} \approx 0.35$ for $p = 40$ GeV and $\frac{\sigma_{1/p}}{1/p} \approx 0.60$ for $p = 80$ GeV.

In figure 4.7 a considerably better resolution is seen than that calculated above. This is because the two θ directions of the segments are not treated independently by the reconstruction. Instead, the fact that the post–toroid segment belongs to the same muon track as the pre–toroid segment is implicitly being used. The post–toroid segment is being corrected with respect to the pre–toroid segment by the 'momentum scan' reconstruction method explained in the previous chapter. This is best understood by considering reconstructing the tracks of very high momentum muons and referring back to equation 4.2. The uncertainty in A_x was the dominant factor in the determination of the θ coordinate of a segment. However, when the two segments are linked together to form a high momentum (and therefore very nearly straight) track, the values of A_x from the two segments are constrained to be very nearly the same. Effectively, the influence of the A_x uncertainty on the $\Delta\theta$ measurement is being removed. It could therefore be expected that for high momentum tracks, the correct value of $\sigma_{\Delta\theta}^{rec}$ to be used in equation 4.5 is the value at the octant axis ($\eta \approx 0$) where A_x is not the dominant factor. From figure 4.6 it is seen that $\sigma_{\Delta\theta}^{rec} \approx 10^{-3}$ radians near the octant axis. Applying this value to equation 4.5 yields $\frac{\sigma_{1/p}}{1/p} \approx 0.23$ for $p = 40$ GeV and $\frac{\sigma_{1/p}}{1/p} \approx 0.26$ for $p = 80$ GeV. These are in good agreement with figure 4.7.

The better inverse momentum resolution shown in figure 4.7 than was shown to be possible in figure 4.4 for the lowest muon momentum considered (about 3 GeV) is caused by the lack of efficiency in reconstructing these tracks. Only about 70% of muons entering the system are reconstructed since others suffer too much multiple scattering to leave a post–toroid track segment that might be associated with the

incoming muon track segment. For all other samples corresponding to the other points on the plot 4.7 the reconstruction efficiency was greater than 90%.

Muons generated with a momentum of 160 GeV produce a double peak distribution of reconstructed momenta which is also a result of the momentum scan method. The main peak is centred at the correct momentum of 160 GeV, but a second smaller peak corresponds to about 20% of the muons which are reconstructed as having a momentum of greater than 300 GeV. At high momenta the values of p_{assumed} in the momentum scan are widely spaced, consecutive values being 1000 GeV, 250 GeV, 100 GeV, 80 GeV and so on with ever decreasing gaps down to 2.25 GeV. This may result in a higher probability of the momentum being reconstructed in the range between 1000 GeV and 250 GeV than otherwise. With momentum scan values changed from the defaults above to be consecutively 300 GeV, 200 GeV, 100 GeV, 80 GeV and then as before, the double peak disappears and the reconstructed fractional inverse momentum resolution is less than 0.4. With such straight tracks as are produced by muons with very high momentum there is a danger of mis–identifying the charge of the muon. This is found to be true of only about 5% of muons at 160 GeV in this study.

The conclusion is that the forward muon system is capable of identifying the charge of muons and producing a satisfactory momentum measurement for muons which enter the system with momentum p in the range 2.25 $GeV < p < 200\ GeV$.

4.4   Pointing to the Forward Tracker

Charged particles detected in the forward tracker of H1 can be reconstructed with a momentum resolution $\sigma_p/p < 0.003p$ and track angular resolution $\sigma_{\theta,\phi} < 10^{-3}$ radians [27]. With the exception of very high momentum muons (greater than about 100 GeV) there is therefore an obvious advantage in trying to identify the track left by a muon in the forward tracker rather than simply using the results of the forward muon detector independently. In this sense the forward muon detector is acting as an unambiguous identifier of muons which are the only particles originating from the H1 vertex which pass through the calorimeter and instrumented iron. Successful identification of the track left by the muon in the forward tracker requires the forward muon system to be able to reconstruct the parameters of a muon not only

on entry to the forward muon system but in the forward tracking region of H1. This must be done sufficiently well such that the muon track in the forward tracker is distinguishable from the other tracks in that region. Inelastic scattering events in H1 typically result in a high density of tracks in the forward region.

The ability of the forward muon system to evaluate the momentum and direction of a muon near the H1 vertex is assessed in this section via a study of the effects on a muon passing through the H1 detector from the vertex to the forward muon system. In the next sections this is related to the identification of muons in the forward tracker which result from the decay of inelastically produced J/ψ mesons and which must therefore be distinguished from the background of other tracks in the forward tracker.

A muon originating from near the H1 vertex must pass through the central and forward trackers, the electromagnetic and hadronic calorimeters and the instrumented iron before entering the forward muon system. In doing so it suffers multiple scattering and energy loss in the media and bending in the field of the H1 solenoidal magnet and the return yoke. To some extent, in trying to work out the momentum and direction of a muon as they were at the H1 vertex, corrections can be applied to the reconstructed values on entry to the forward muon system. The average energy loss, perhaps as a function of momentum and direction, can be taken into account, as can the average bending in azimuthal angle ϕ, itself a function of momentum, charge and direction. Multiple scattering and the energy loss distribution cannot be corrected for and will contribute to the lack of resolution of reconstructing the initial momentum and direction.

The H1 detector simulation is used to investigate the effects on muons passing from the vertex to entering the forward muon system. Single muons of specified momentum and direction are generated at the vertex and their parameters compared on entering the forward muon system to those at the vertex. This is independent of the forward muon system itself, only the muon track record from the simulation of the particle passing through the H1 detector is used. The study is only concerned with muons which could pass through the forward muon system so they are generated with polar angles in the range $2° < \theta < 20°$.

The energy loss suffered by the muons is dependent upon the momentum of the muon and the materials through which they pass. For muons originating at the
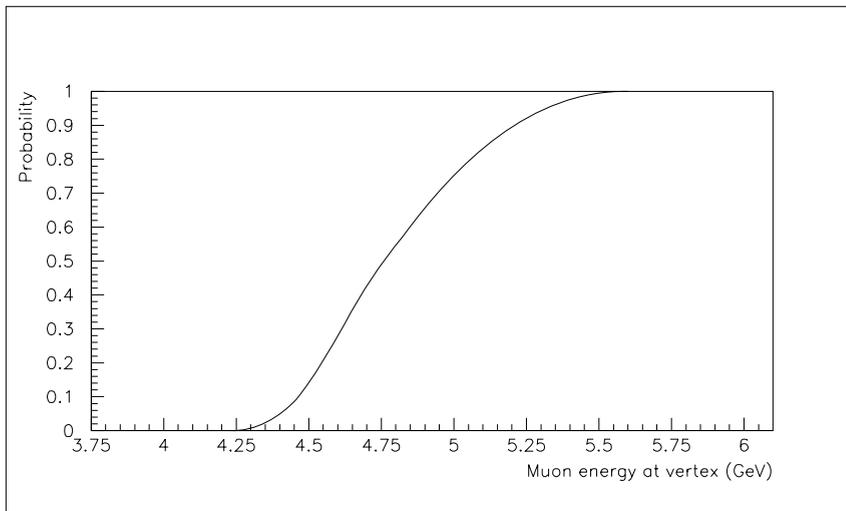
Figure 4.8: Probability that a muon will reach the forward muon detector with reconstructable momentum (> 2.25 GeV) as a function of the starting momentum of the muon, i.e. the momentum at the H1 vertex.

vertex with polar angle $\theta > 5°$ the energy loss is found to be very nearly independent of θ and ϕ, reflecting the symmetry of the H1 detector in this region. At lower angles the irregular structure of the calorimeters, beam–pipe and instrumented iron causes the energy loss to be quite strongly dependent on θ, but such muons would not anyway leave a track in the forward tracker. The dependence on momentum is weak as would be expected of minimum ionising particles, a good approximation to energy loss being given by $(0.005p + 2.9)$ GeV for momentum p in the range 5 to 100 GeV. An immediate consequence of this is that muons of momentum less than about 3 GeV cannot be expected to reach the forward muon system at all, and considering also that muons entering the FMD with momentum less than 2.25 GeV will not be reconstructed leads to the result of figure 4.8 which shows the probability of a muon reaching the FMD with reconstructable momentum as a function of the momentum that the muon has at the H1 vertex.

Energy loss is due mostly to a finite number of ionising collisions which results in a Landau type distribution. The RMS of this distribution is less than about 0.5 GeV for muons of less than 100 GeV momentum and only about 0.2 GeV for muons with a starting momentum 6 GeV. This spread is much less than the momentum resolution of the FMD and so does not compromise the ability to reconstruct the momentum at

the H1 vertex. By the same reasoning a correction to the momentum reconstructed by the FMD to account for energy loss which is dependent on momentum is not helpful. Assuming the momentum of the muon at the vertex to be 2.9 GeV greater than the momentum as reconstructed in the forward muon system leads to the fractional inverse momentum resolution shown in figure 4.9. Here p is the momentum at the vertex of H1 and the forward muon system is seen to be able to determine p to better than 27% up to 80 GeV.

Such a momentum resolution has particular significance for identifying muons resulting from the decay of charged kaons. Most such decays are identified by a kink in the track in the central tracking chambers or by a mismatch in track directions between the muon as detected in the muon chambers and the kaon in the central trackers. However, a background of muons with high transverse momenta from kaon decays still remains after such considerations which can be almost eliminated if the momentum of the muons can be reconstructed to better than about 30% [25]. The forward muon system is therefore potentially effective in identifying high energy muons which arise from the decay of kaons and which would not otherwise be recognised.

Multiple scattering of muons in the H1 detector occurs to a degree which is also almost independent of the polar angle θ of the muons for $\theta > 5°$ but which is inversely proportional to the momentum (up to an energy loss correction). Two parameters can be used to describe the amount of multiple scattering, one which refers to the change of direction of flight of the muons, and one which refers to the displacement of the point of entry to the forward muon system with respect to the starting direction of the muons. Considering the polar coordinate θ: a muon has a direction of flight at the vertex corresponding to θ_{vertex} but due to multiple scattering could have some other direction of flight on entering the forward muon system, θ_{FMD} (see figure 4.10). The distribution of $\theta_{FMD} - \theta_{vertex}$ is approximately normal with standard deviation θ_0 which can then be used to quantify the multiple scattering. Similarly the point of entry of the muon to the forward muon system may have the polar coordinate θ_{FMDpoe} (figure 4.10) and the distribution of $\theta_{FMDpoe} - \theta_{vertex}$ is also almost normal and has a standard deviation θ_1, the second parameter. For a particle passing through a constant medium the relationship $\theta_0 = \sqrt{3}\theta_1$ should hold [28], though since for a muon passing through H1 most of the scattering will occur in the instrumented iron the factor would be expected to be larger than $\sqrt{3}$.
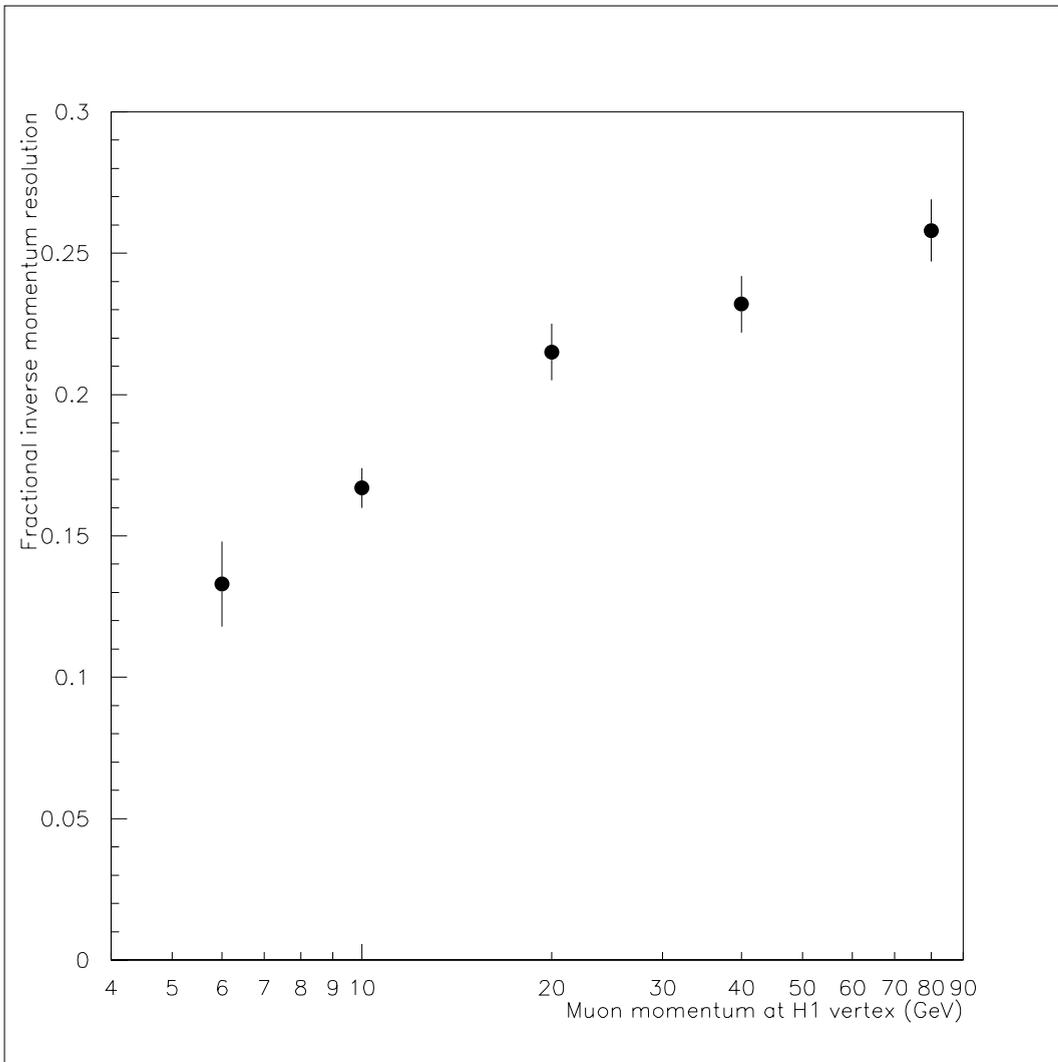
Figure 4.9: Fractional inverse momentum resolution, $\frac{\sigma_{1/p}}{1/p}$, as a function of p, where p is the muon momentum at the H1 vertex. The measured p is taken to be the momentum reconstructed in the FMD plus 2.9 GeV to correct for energy loss.
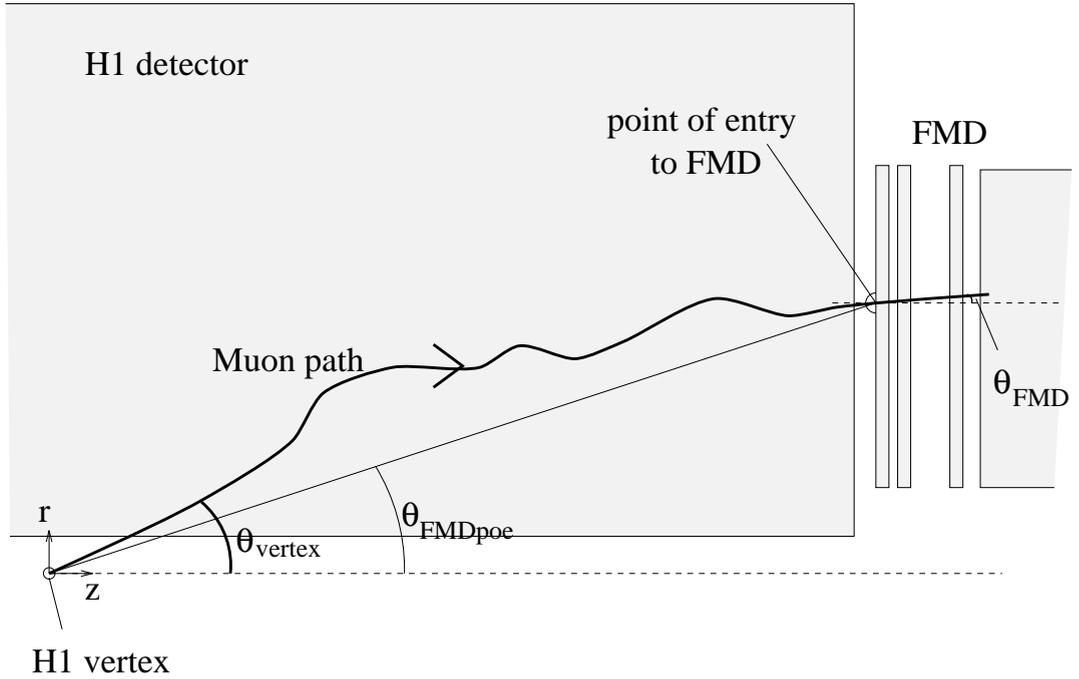
Figure 4.10: Illustration of the three angles θ_{vertex}, θ_{FMD} and θ_{FMDpoe}.

Simulation studies lead to the results

$$
\begin{aligned}
\theta_0 &= \frac{0.18}{p - 1.5} \text{ radians and} \\
\theta_1 &= \frac{0.06}{p - 1.5} \text{ radians}
\end{aligned}
\tag{4.6}
$$

where p is the starting momentum of the muons in GeV and the 1.5 GeV is a first order correction for energy loss.

The forward muon system is able to determine the θ coordinate of the direction of flight of a muon on entry (θ_{FMD}) with a resolution of about 3×10^{-3} radians (see figure 4.6) and the θ coordinate of the point of entry to the forward muon system (θ_{FMDpoe}) with a resolution better than 4×10^{-4} radians. The original direction of flight of the muon at the vertex (θ_{vertex}) can clearly be better determined by using θ_{FMDpoe}, and then the resolution is limited almost entirely by the degree of multiple scattering in H1 up to very high momenta (> 100 GeV). Thus, for muons originating at the event vertex with momentum up to at least 100 GeV, the θ coordinate of the direction of flight at the vertex should be determined by the forward muon system with a resolution of about θ_1 as given in equation 4.6.

In reconstructing the azimuthal coordinate ϕ of the direction of flight of the muon at the vertex a correction must be made for the bending in the solenoidal field. The resolution will then be limited by multiple scattering as for the θ coordinate, and this can be quantified by ϕ_0 and ϕ_1 which correspond to θ_0 and θ_1. More precisely, purely geometrical reasoning leads to the results $\phi_0 = \theta_0 / \sin\theta$ and $\phi_1 = \theta_1 / \sin\theta$.

Magnetic bending occurs in the central region of H1 in the solenoidal field and in the return yoke, where bending is in the opposite direction. In fact the bending in the two regions are expected to compensate each other exactly, in the sense that the muon track points back to the vertex as it leaves the return yoke, as long as energy loss can be ignored [43]. This is found to be the case with the ϕ coordinate of the direction of flight on entering the forward muon system being , on average, equal to the ϕ coordinate of the point of entry, and being $0.86/p$ radians greater than that at the vertex (independently of θ, for negatively charged muons). Where energy loss is significant the bending in the return yoke would be expected to be greater than the bending in the central region of H1 so that the change of the ϕ coordinate of the direction of flight will be less than the difference between the ϕ coordinate of the point of entry and that at the vertex. This effect is observed in the simulation studies.

Again it is better to use the reconstructed ϕ coordinate of the point of entry to the forward muon system to determine the ϕ coordinate of the initial direction of flight. The former value is reconstructed with a resolution better than $(8 \times 10^{-4} / \sin\theta)$ radians which is smaller than the degree of multiple scattering at least up to 70 GeV. Since the amount of magnetic bending is in general greater than the degree of multiple scattering a correction to account for this bending is clearly worthwhile. This introduces an error independent of the multiple scattering because the momentum of the muon is not known a priori, and so the correction to account for the bending is not exact. Making this bending correction based on the momentum as reconstructed in the forward muon system will lead to a resolution, σ_ϕ, of reconstructing the ϕ coordinate of direction of flight at the vertex which is a combination of multiple scattering and correction error:

$$\sin^2\theta \, \sigma_\phi^2 \approx \left(\frac{0.06}{p-1.5} \right)^2 + \left(\frac{0.86\sin\theta}{p} \frac{\sigma_{1/p}}{1/p} \right)^2 \text{ radians}^2 \qquad (4.7)$$

where p, the momentum of the muon at the vertex, is in GeV. Although the second term is significant and means that $\sin\theta \, \sigma_\phi$ is a (weak) function of θ, the first term,

representing the limitation due to multiple scattering, is always dominant within the θ range covered by the forward muon detector and for momenta up to at least 100 GeV. Averaging over this θ and p range the second term adds about 10% to the resolution, $\sin\theta \, \sigma_\phi$, that would result from multiple scattering uncertainty alone.

Figure 4.11 shows the resolutions for reconstructing the θ and ϕ coordinates of the direction of flight of muons at the H1 vertex using only the forward muon system reconstructed point of entry and correcting ϕ for magnetic bending, as obtained from simulation studies. It supports the arguments of the previous paragraphs, in particular that the ability of the forward muon system to find the initial direction of a muon is almost entirely limited by the amount of multiple scattering undergone in the H1 detector before reaching the forward muon detector.

In summary, figures 4.9 and 4.11 represent the ability of the forward muon system to recover the momentum and direction that a muon has at the H1 vertex. The momentum resolution is limited almost entirely by the momentum resolution of the forward muon system itself, and the directional resolution by multiple scattering in the H1 detector. A proper (full covariance) treatment of the forward muon detector output may lead to better results than are shown in 4.11 but the multiple scattering limit represented by the lines on the plots cannot be improved upon.

4.5 *J/ψ* **Production in H1**

The J/ψ meson is interpreted as a bound state of a $c\bar{c}$ pair of total spin, s, of 1 and total angular momentum, l, of 0. Importantly, it shares the J^{PC} quantum numbers of a photon ($J^{PC} = 1^{--}$). Since its mass, 3.097 GeV [28], is less than that of a $D\bar{D}$ pair, and it is the lowest energy $c\bar{c}$ vector state, it can only decay into states involving the lighter quarks: u, d, s. Such decays are suppressed so that the J/ψ has a very narrow resonance width and, more importantly from the point of view of identification in H1, has a significant branching ratio to $\mu^+\mu^-$ and e^+e^- pairs (about 6% each) via electromagnetic decay [29]. It is the decay channel $J/\psi \rightarrow \mu^+\mu^-$ which is considered here, the J/ψ resonance appearing as a peak in the di–muon invariant mass spectrum.

The study of J/ψ events at HERA is expected, through classification into various production mechanisms, to yield a measurement of the gluon content of the proton
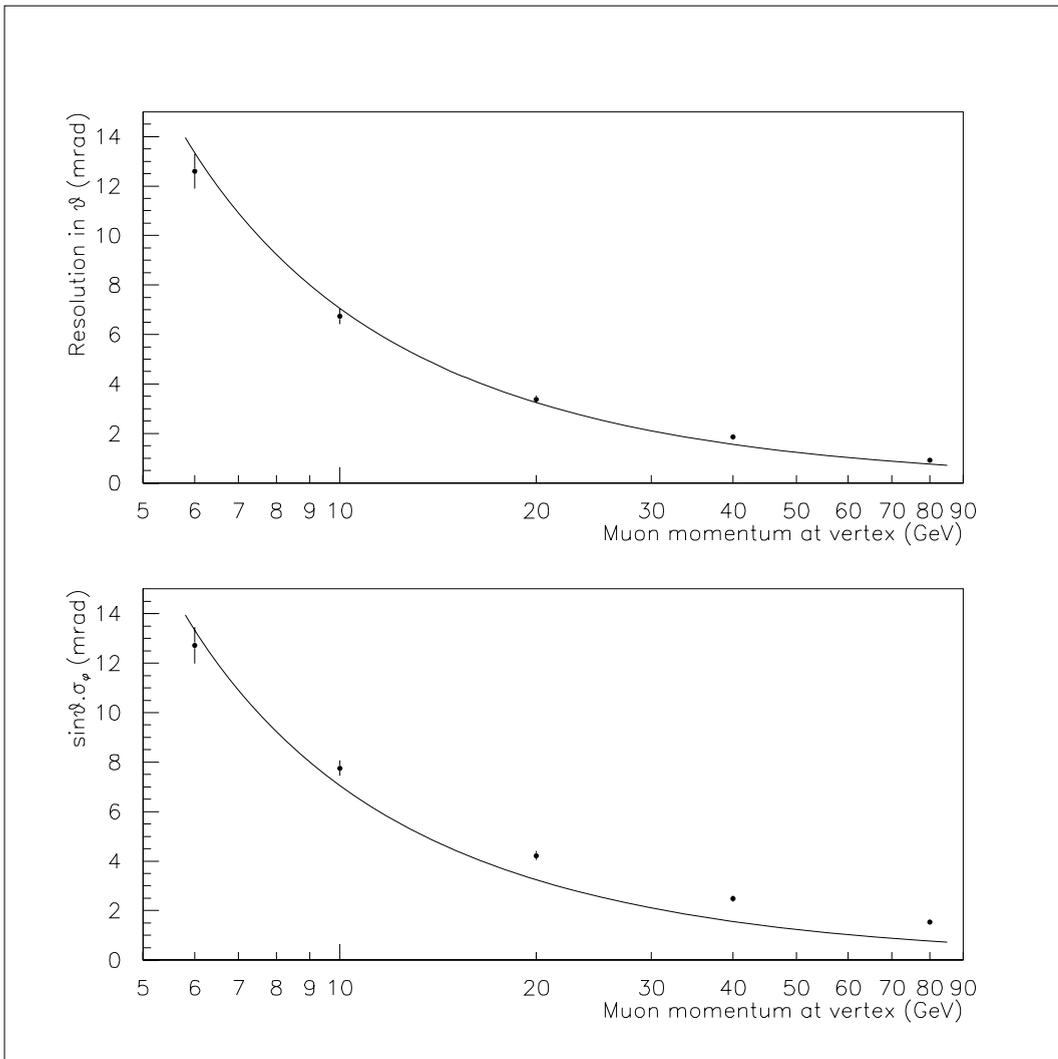
Figure 4.11: Resolutions of reconstructing the direction of flight of a muon at the H1 vertex using the forward muon system alone. Top: resolution in polar angle θ; bottom: resolution in azimuthal angle ϕ multiplied by $\sin\theta$.
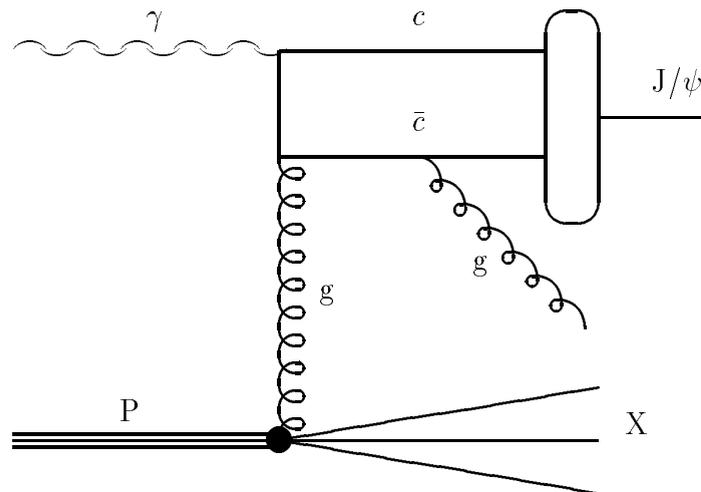
Figure 4.12: The photon–gluon fusion mechanism for J/ψ production.

down to $x_g \approx 3 \times 10^{-4}$ (x_g is the momentum fraction of the proton which the gluon has) [44, 45, 19], to discriminate between various models of elastic and diffractive production and so shed some light on the nature of the pomeron [46, 19], and possibly to give some measurement of the structure of the photon [47, 48, 19]. Since the mass of the J/ψ is already so well determined, the position of the J/ψ resonance peak will provide a calibration check for the H1 detector.

The physics studies mentioned above are made by identifying J/ψ photoproduction events, essentially γp collisions where the almost real photon is radiated by the incoming electron. In the rest frame of the proton, the photon can have energy up to about 50 TeV at HERA, to be compared with the energies of previous experiments in which typical photon energies are 100 GeV, and so models of J/ψ production used to describe previous results will be tested in a new kinematic regime at HERA.

Most generally, the photoproduction interaction considered is

$$\gamma(q) + p(P) \longrightarrow J/\psi(p_\psi) + X(p_X) \tag{4.8}$$

where the four momenta are shown in brackets and $q^2 \approx 0 \ GeV$. The kinematics of such events are characterised by $s_{\gamma p} = (P + q)^2$, the centre of mass energy squared, $M^2 = p_X^2$, $z = P.p_\psi/P.q$, a measure of inelasticity, and $t = (q - p_\psi)^2$.

A measurement of the gluon content of the proton is made by studying inelastic production of J/ψ, that is, the region in phase space of high mass M. The dominant process here is photon–gluon fusion, as illustrated in figure 4.12, a second gluon being
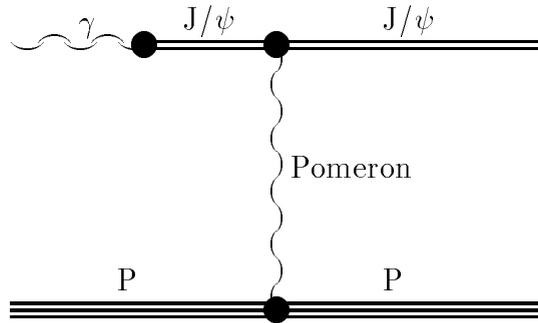
Figure 4.13: Elastic or diffractive (where the proton remnant has a similar mass to the proton) production of J/ψ by the transfer of a photon–like pomeron.

produced so that the $c\bar{c}$ pair may be a colour singlet. A perturbative calculation of the expected cross–section for this production mechanism of J/ψ is valid in the region $z < 0.9$, $|t| > 1\ GeV^2$, $M > 2$ GeV, considering the J/ψ meson as an S–wave bound state of $c\bar{c}$ [49, 50]. Since the cross–section from photon–gluon fusion is directly proportional to the gluon density in the proton at a scale of around $s_{\gamma p}$, by extracting a pure sample of such events the gluon content of the proton can be measured [45]. Such a sample can be selected by taking a more restricted region of phase space, namely $0.2 < z < 0.9$, and accepting only events in which the J/ψ was produced with more than 1 GeV transverse momentum (with respect to the photon axis in the γp centre of mass frame) and in which both decay muons were produced in the polar angular range $11° < \theta < 169°$ [19]. The remaining cross–section is about 37 pb, including the branching ratio to a di–muon pair, with a background due to other J/ψ production mechanisms of about 3%. A measurement of the gluon structure function which is good enough to distinguish between different present expectations should be possible after H1 has collected about 20 pb^{-1} of data.

In the regime of small mass transfer t the model described above does not represent J/ψ production fully, a perturbative calculation is no longer valid. The elastic and diffractive production are characterised by the proton remaining intact or nearly intact, low mass M and $z \approx 1$. A model based on the pomeron is used to describe present data and to predict cross–sections at HERA. Different interpretations of the pomeron itself are used. In one such the pomeron is regarded is photon–like [51], coupling directly to the quarks in the J/ψ and proton. A fluctuation of the photon
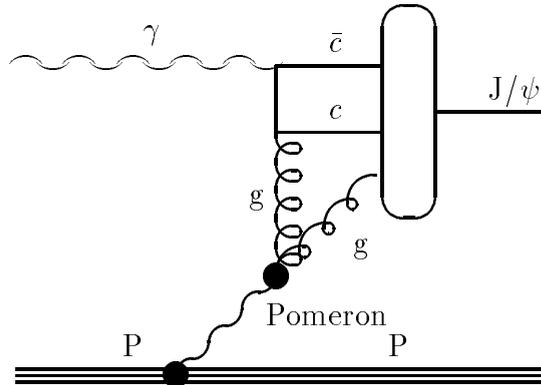
Figure 4.14: Elastic production of J/ψ as mediated by a pomeron consisting of gluons.

into an off-shell J/ψ (in a VMD–style transition) is realised by the pomeron which puts the J/ψ on shell as represented by figure 4.13 [46]. Another model regards the pomeron as consisting of a bound state of gluons [52]. A gluon from the pomeron participates in the hard interaction which is photon–gluon fusion as before. Such a model can also be used for elastic production, the relevant diagram being that of figure 4.14 [19]. In this model, cross–sections will clearly be dependent on the gluon content of the pomeron, so that the study of such interactions will provide information about its structure. Events of a diffractive nature can be recognised by the lack of proton remnant observed in the forward direction in H1.

The higher energies available at HERA than in previous experiments mean that a new production mechanism will be seen in which a parton from the photon participates in the hard interaction. In this way a photon structure is being resolved, and the study of these events, which may be recognised by the photon remnant, low z values and the forward produced J/ψ, could provide information about the hadronic nature of the photon [47, 19]. In particular, the interaction in which a gluon from the proton and a gluon from the photon participate in a gluon–gluon fusion hard interaction to produce a J/ψ and photon in the final state (figure 4.15) may lead to measurements of the gluon content of the photon [48]. The cross–section for this process is difficult to estimate because the gluon content of the photon is little known, but is certainly so small that measurements of the gluon content of the photon will only be possible after several years of H1 data taking.
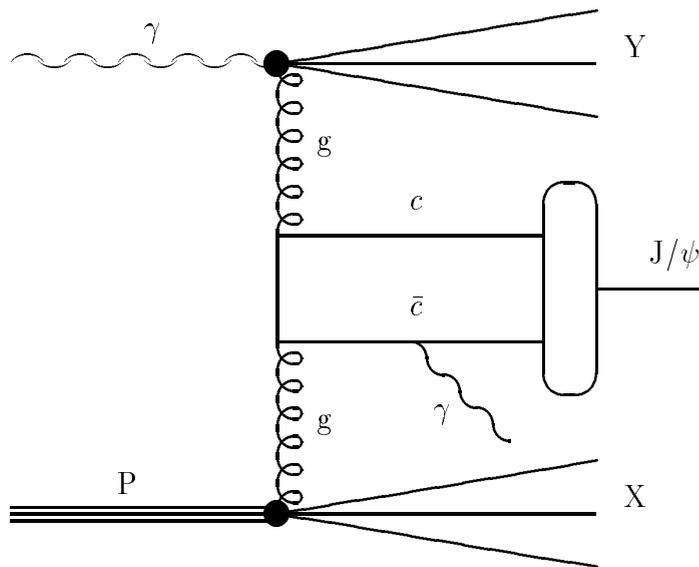
Figure 4.15: J/ψ produced by a resolved photon, in this case a gluon from the photon participating in the hard interaction with a gluon from the proton. There is a photon remnant, denoted Y, as well as the normal proton remnant.

The models outlined above lead to estimations of the cross–sections for J/ψ production at HERA of about 8 nb for the inelastic process (photon–gluon fusion) and about 4 nb for elastic and diffractive production [19]. No cuts are made to reach these values, and the branching ratio of $J/\psi \rightarrow \mu^+\mu^-$ is not included. As mentioned above, including the branching ratio and making suitable cuts to isolate a reasonably pure sample of J/ψ mesons produced via the photon–gluon fusion mechanism reduces the cross–section to about 37 pb. The efficiency of the H1 detector in detecting such events further reduces the number of J/ψ events found so that any physics study made requires a much greater integrated luminosity than is currently available. Resolved photon and other rarer production mechanisms have cross–sections at least an order of magnitude less than those above [19].

4.6 Role of the FMD in J/ψ Reconstruction

The identification of J/ψ particles in the H1 detector through the decay to a $\mu^+\mu^-$ pair requires the detection of the two muons and the reconstruction of the invariant mass, $M_{\mu^+\mu^-}$, given by $M^2_{\mu^+\mu^-} = (p_{\mu^+} + p_{\mu^-})^2$. Detection requires the muon having sufficient energy to leave a track in a muon detector, whilst reconstruction of the
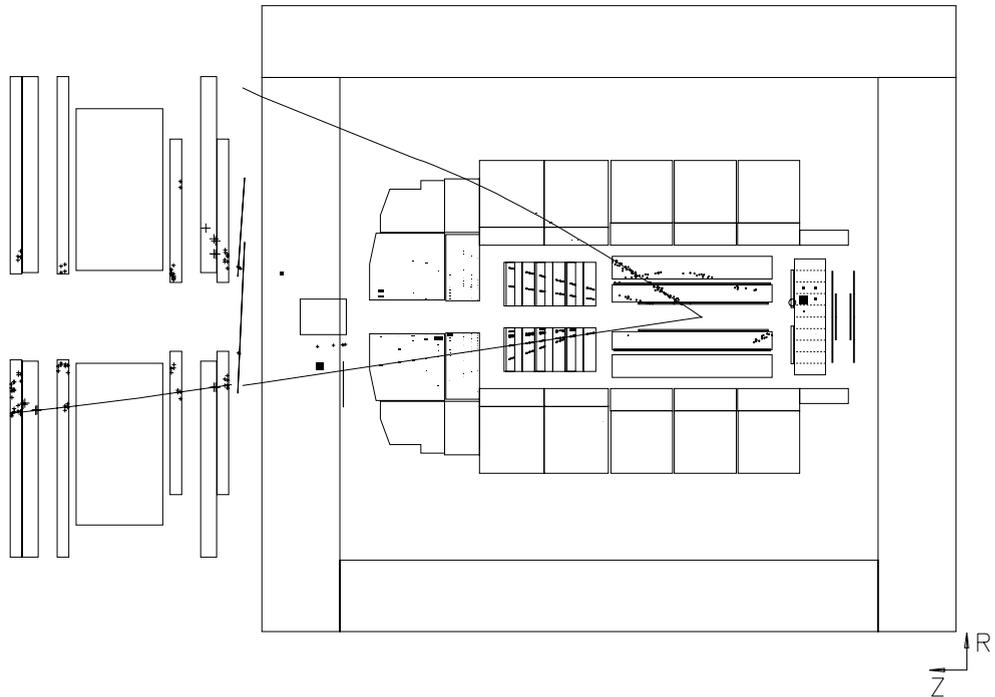
Figure 4.16: A monte carlo generated event in which a J/ψ, produced inelastically by photon–gluon fusion, decays into a di–muon pair in the H1 detector.

invariant mass is much improved by identifying the track left by the muon in the central trackers by linking to the muon detectors. In this section, the importance of the forward muon system in identifying muons from J/ψ decay is assessed by studying the angular and momentum distributions of muons expected in the H1 detector, and the ability of the forward muon system to find the track in the forward tracker left by the muon is tested with inelastically produced J/ψ events using the results of the previous sections.

The study has been made using the EPJPSI generator [53] which takes as its basis the photon–gluon fusion mechanism for inelastic J/ψ production described above. Events have been generated corresponding to about 10 pb^{-1} luminosity, and the program H1SIM was used to simulate the detector response to them. In total there are about 1910 events in which a J/ψ is produced inelastically by photon–gluon fusion and decays into a muon pair.

The H1 detector response to an event generated as above is shown in figure 4.16 in which the μ^-, with a momentum of about 20 GeV, passes through the forward

			μ^+				
			$\theta < 3°$	$3° < \theta < 17°$		$17° < \theta < 155°$		$\theta > 155°$
			all p	$p < 5$	$p > 5$	$p < 2$	$p > 2$	all p
μ^-	$\theta < 3°$	all p	29	7	49	13	5	1
	$3° < \theta < 17°$	$p < 5$	11	0	7	20	13	5
		$p > 5$	37	8	142	50	51	0
	$17° < \theta < 155°$	$p < 2$	24	30	36	160	221	125
		$p > 2$	9	11	50	221	159	68
	$\theta > 155°$	all p	0	5	0	125	64	156

Table 4.1: Angle and momentum characteristics of di–muon pairs arising from J/ψ decay. Momenta, p, are in GeV.

muon system. Both muons' paths of flight are shown as lines emanating from the vertex, and the track of the muon as reconstructed in the forward muon system is also shown. Having identified the muon in the FMD an attempt would be made to recover the track in the forward tracker left by the muon.

An inefficiency in the detection of $J/\psi \rightarrow \mu^+\mu^-$ arises because a muon requires at least 1.2 GeV momentum to reach any muon chambers in H1, since it must traverse the calorimeter in which it loses energy. In practice, the instrumented iron detector of H1 is only efficient in reconstructing muons with momentum greater than about 2 GeV [27], and the equivalent figure for the forward muon system has been shown above to be 5 GeV. These values are to be compared with the momentum that a muon from a J/ψ decay has in the J/ψ rest frame, 1.55 GeV.

In the photon–gluon fusion process the J/ψ is preferably produced with a low momentum in the centre of mass frame of the photon–gluon system which is reflected in a rapidly falling transverse momentum distribution [19]. The result of this is seen in figure 4.17 in which the strong correlation between muon momentum and muon polar angle is shown for all muons from J/ψ decay, and also the correlation between the polar angles of the two muons of the di–muon pair. In particular, there are many decays in which both muons travel at low polar angles in the direction of the forward muon system ($3° < \theta < 17°$) and such muons tend to have high momenta. However, muons produced at large angles to the beam axis are typically of low momentum, below the 2 GeV efficient detection threshold. This is better quantised in table 4.1 in which the muons are categorised according to polar angle θ and momentum. The
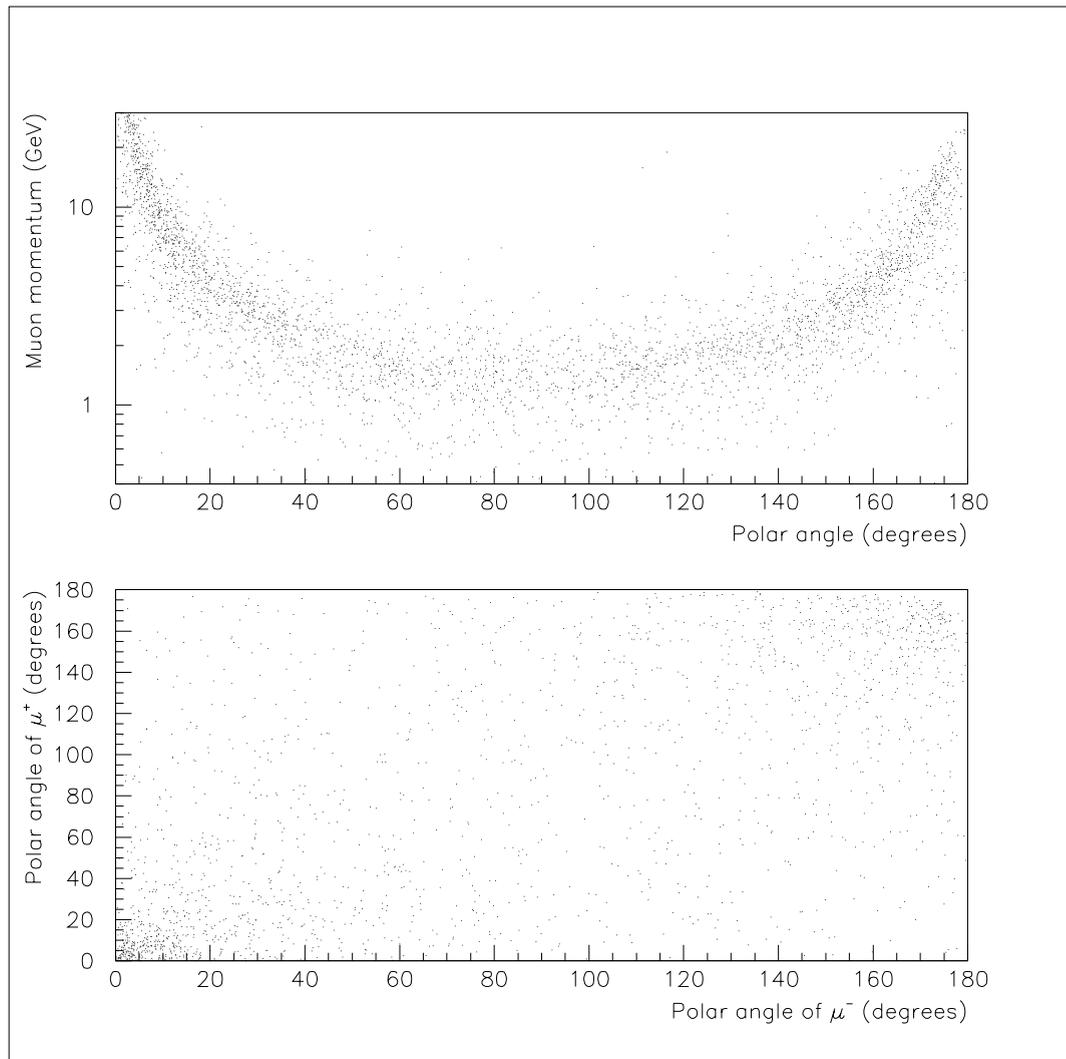
Figure 4.17: Muons produced from J/ψ decay, the J/ψ mesons being produced by the photon–gluon fusion mechanism (monte carlo). Above: the muon momentum in relation to the polar angle for all muons; below: the correlation between the polar angles of the μ^+ and the μ^- produced in the decay.

numbers correspond to the number of events expected after about 10 pb^{-1} integrated luminosity and may in reality be greater by some factor due to the uncertainty in the cross–section calculation, but the proportions should not be very different from those indicated here.

In table 4.1 the H1 detector is split into four regions based on the polar angle θ: muons in the first region, $\theta < 3°$, will not be seen at all but will disappear along the beam–pipe, $3° < \theta < 17°$ is the angular coverage of the forward muon system, in the region $17° < \theta < 155°$ muons can be detected in the instrumented iron chambers and linked to tracks in the central trackers, and muons with polar angle $\theta > 155°$ may be detected in the instrumented iron but will not leave any track in the central trackers. As remarked above, only if the muon has momentum greater than 2 GeV is it likely to be found, and the forward muon detector is only likely to reconstruct the path of a muon with greater than 5 GeV, hence the categories shown in the table. Thus, a J/ψ decaying to a di–muon pair is only likely to be seen in the H1 detector if both of the decay muons fall into one of the two categories
(a) $3° < \theta < 17°$ and $p > 5$ GeV or;
(b) $17° < \theta < 155°$ and $p > 2$ GeV.
This is only true of 402 of the 1912 muon pairs of table 4.1, that is, in about 21% of cases in which a J/ψ produced inelastically by photon–gluon fusion decays to a $\mu^+\mu^-$ pair both muons are likely to be identified in the H1 detector. For 60% of these events at least one of the muons is identified in the forward muon detector. Both muons can be detected in the FMD in 35% of them.

In figure 4.18 the momentum spectrum of muons from J/ψ decay which are produced in the direction of the forward muon system is shown. The range of momenta are are quite well matched to the abilities of the FMD, 83% of the muons having more than 5 GeV momentum and all other muons being in a momentum range in which the FMD has a fractional inverse momentum resolution of better than 25% (see figure 4.9).

Figure 4.19 is the reconstructed invariant mass of the di–muon pair for events in which both muons from the J/ψ decay are detected in the FMD. Before calculating the invariant mass the momenta and directions of the muons as reconstructed in the forward muon system are corrected for energy loss and magnetic bending. The fit shown is gaussian with mean 3.02 GeV (with 0.07 GeV uncertainty) and standard deviation 0.55 GeV, which should be compared to the J/ψ mass of 3.10 GeV.
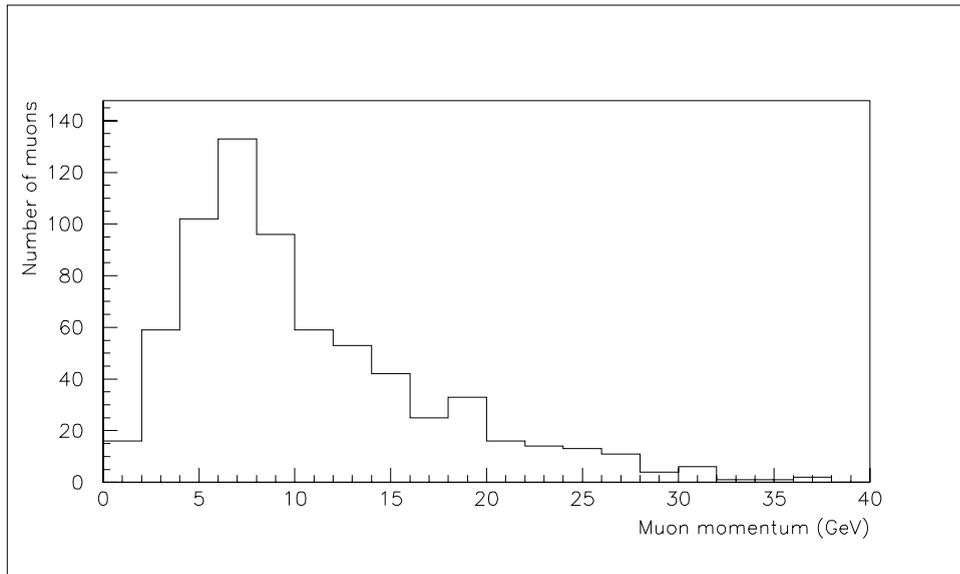
Figure 4.18: The momentum distribution of muons produced in the direction of the forward muon system from J/ψ decay.
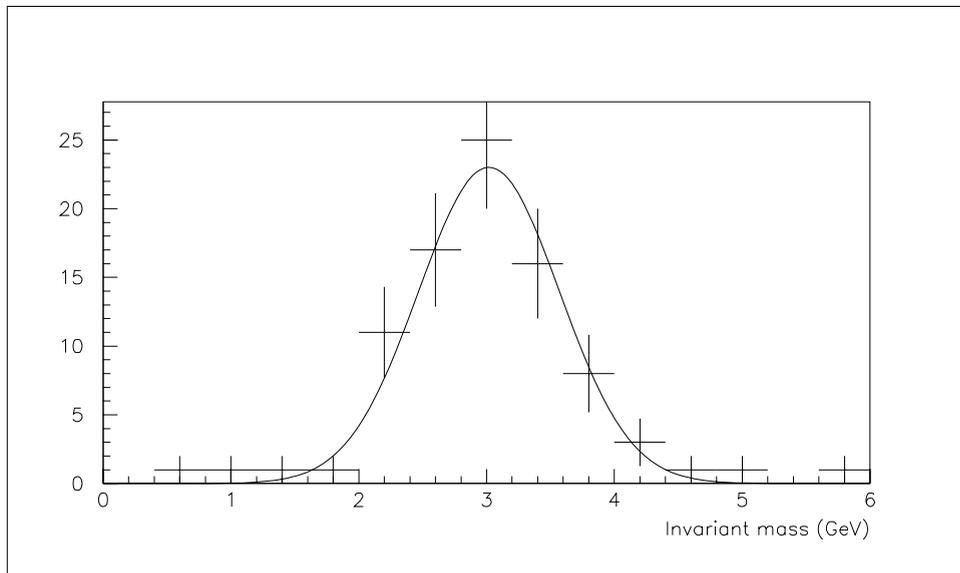

Figure 4.19: Invariant mass distribution of the di–muon pairs from J/ψ decay in which both muons are reconstructed in the forward muon system. The momenta of the muons as used in the invariant mass calculation is taken from the FMD reconstruction alone, without linking to the central trackers.

The resolution of J/ψ mass reconstruction would be better than 0.55 GeV if the momentum and direction of the muon as measured in the forward tracker were used.

The potential efficiency in identifying the track left by the muon in the forward tracker depends on the density of tracks there in comparison to the ability of the forward muon system to reconstruct the momentum and direction of flight of the muon. This is studied here by using the output from the simulation program H1SIM which results from the EPJPSI generator for inelastically produced J/ψ mesons. Only events in which at least one of the muons from the decay of the J/ψ travels in the direction of the forward muon system are studied, and for these events all charged particles in the forward tracker (FTD) other than the muon are considered. If the track of another charged particle is sufficiently close to the muon track in direction, such that the forward muon system cannot distinguish between it and and the muon by virtue of direction of flight alone, the momenta of the charged particle and the muon are compared to see if the forward muon system would be able to determine which track was left by the muon it has detected.

The rejection of charged tracks which are not close to the muon in the FTD in direction is made on the basis of the result of figure 4.11 in which the resolutions σ_θ and σ_ϕ, with which the forward muon system can reconstruct the direction of flight of a muon in the forward tracker, are shown. If a track is more than 6σ away from the muon in either the θ or ϕ coordinate of the direction of flight then it is assumed that the forward muon system could not mistake it for the muon track. Such a cut would introduce a linking inefficiency of less than 1%, that is, in less than 1% of cases would the forward muon system choose a track so far from the actual muon track in preference to the muon track on the basis of direction of flight alone.

From a total of 332 inelastic J/ψ events in which a muon was produced in the direction of the forward muon system with greater than 4.25 GeV momentum there are only 26 in which there is some other track, left by a charged particle with momentum greater than 1 GeV in the FTD, which is not rejected by the above angular cut. These tracks could be confused with the muon track in the forward tracker if the forward muon system were unable to provide any momentum information. In figure 4.20 the momentum spectrum of the tracks which may be mistaken for muons is shown. The momenta, p_{track}, are those of the charged particles which remain after the angular cut and can be seen to be preferably small. Since no muon with less than 4.25 GeV momentum will leave a track in the forward
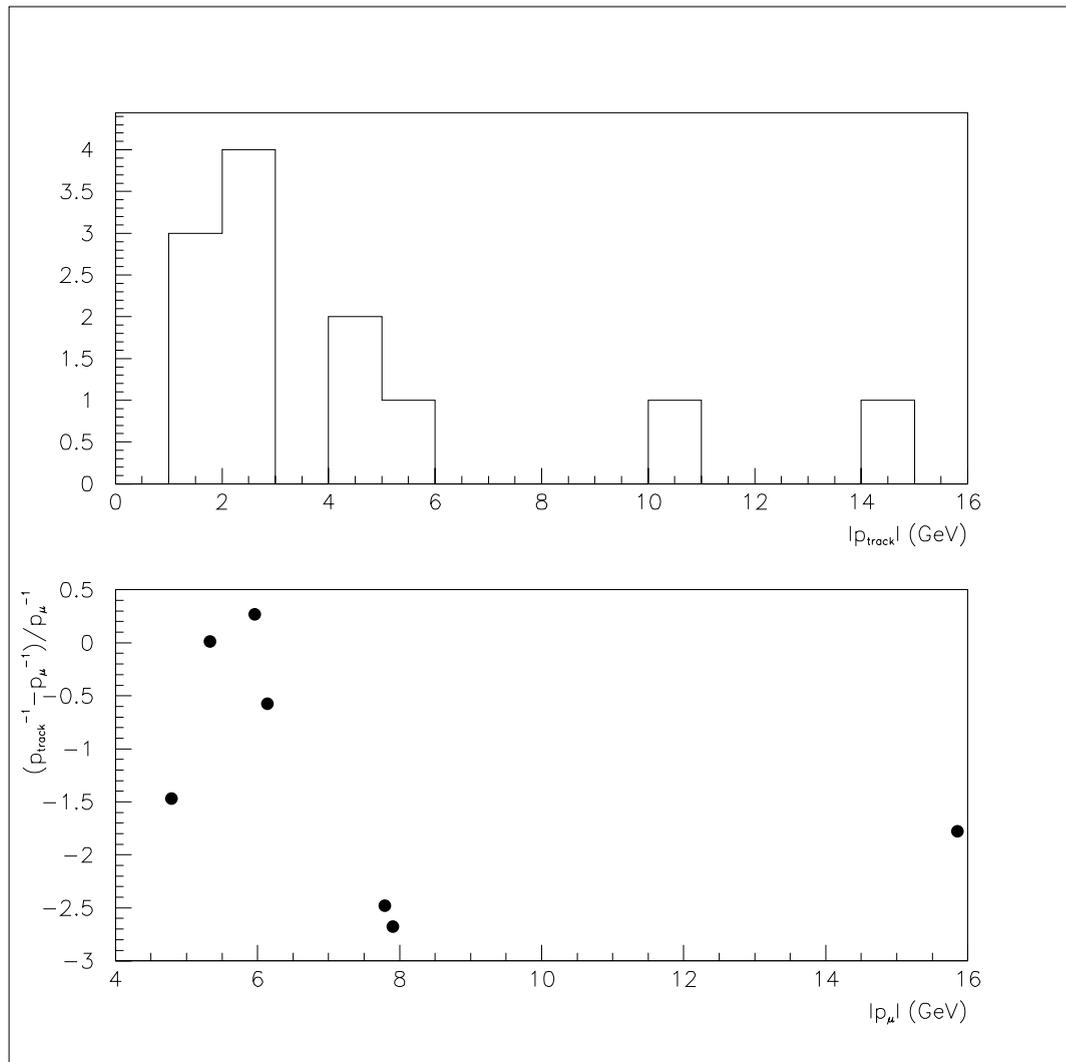
Figure 4.20: Above: the momenta of the charged tracks which may falsely be identified as muon tracks by virtue of their direction of flight. Below: $(p_{track}^{-1} - p_\mu^{-1})/p_\mu^{-1}$ and p_μ for the events in which a charged track of momentum $p_{track} > 4.25$ GeV may be falsely identified as the muon track.

muon system (see figure 4.8) the tracks of particles with smaller momentum seen in the FTD can be rejected immediately. Then only 7 remaining events include tracks not left by the muon which the forward muon system may falsely identify as the muon track. The lower plot shows the muon momenta, p_μ, and the values $(p_{track}^{-1} - p_\mu^{-1})/p_\mu^{-1})$ for these seven events, which should be compared to resolution $\frac{\sigma_{1/p}}{1/p}$ as shown in figure 4.9.

Given that the fractional inverse momentum resolution of the forward muon system is better than 15% for 6 GeV muons (figure 4.9), 5 of the 7 events can be rejected by the momentum measurement in the FMD, the possible fake muon tracks differing in momentum from the actual muon by more than 4σ. Thus, from the original sample of 332 events there remain only two in which the forward muon system might identify the wrong track in the forward tracker as being that of the muon which the FMD has detected.

In summary, these simulation studies show that in more than 99% of events in which a J/ψ is produced inelastically and decays into a $\mu^+\mu^-$ pair, and in which one of the muons leaves a track in the forward tracker and the forward muon system, the track left by the muon in the FTD can be identified.

4.7   Summary

In the context of the simulation program H1SIM, which models the output of the detector H1, there is a detailed description of the forward muon system. It can be used to study the potential performance of the FMD.

Such studies show that a muon originating at the H1 vertex with polar angle approximately in the range $3° < \theta < 17°$ and momentum between 5 GeV and 200 GeV can be detected in the FMD, and that its momentum can be determined with a fractional resolution, $\frac{\sigma_{1/p}}{1/p}$, which rises from about 14% to about 26% over the momentum range 5 GeV to 80 GeV. The lower limit of detectable momentum is due to energy loss experienced in the H1 detector before entering the forward muon system, and in the iron magnet of the forward muon system. Multiple scattering in the iron magnet makes a better momentum determination at small momenta impossible. The direction of flight of the muon at the vertex can be measured by the forward muon system to an accuracy limited mostly by multiple scattering in

the H1 detector.

An example of a physics process in which muon detection is important is inelastic J/ψ production via the photon–gluon fusion mechanism. The expected angular and momentum spectra of the final state muons mean that the forward muon system has an important rôle to play in J/ψ detection. In such events the forward muon system is capable of identifying the track in the forward tracker which was left by a muon found in the FMD.

Chapter 5

Hadronic Energy Flow in DIS

5.1 Introduction

The basis of deep inelastic scattering (DIS) at HERA was introduced in chapter 1. In the case of a neutral current interaction, the process

$$electron + proton \longrightarrow electron + hadrons$$

is mediated by a virtual boson, more precisely by a space–like photon or Z_0. In this chapter a quantitative study of the hadronic final state arising from such interactions as seen in the H1 detector is made. The data sample for the study is from the period of operation in Autumn 1992, at which time 26.7 GeV electrons were being collided with 820 GeV protons, and corresponds to an integrated luminosity of about 23 nb^{-1}.

Events are selected with the aim of producing a pure sample of neutral current DIS events in which the hadronic energy flow is well measured. Details of how this is achieved are given below. It is then possible to investigate the distribution of energy flow in the detector, and make comparisons with the predictions implemented in various Monte Carlo generators, briefly described later.

Even at the lower energies available in previous experiments, the Quark Parton Model alone has proved unable to account for the hadronic energy flow distributions [54], and QCD corrections to that model have been needed to do so. At HERA the larger phase space available for QCD effects makes the visible distributions sensitive to perturbative QCD effects in these interactions, those of hard

parton emission resulting in jets and softer multiple gluon emission [55]. Since most of the proton remnant escapes along the beam pipe and is not observed in the H1 detector, this experiment is most sensitive to radiation from the parton participating in the hard process. Testing the ability of the Monte Carlo generators to predict the H1 data therefore tests current understanding of QCD and also the validity of some of the approximations used. Of particular interest is the newly accessible low Bjorken x region, where there is phase space available for significant initial state radiation, that is radiation from the struck quark before the boson vertex, a better understanding of which will shed light on QCD evolution, and indirectly on the structure function of the proton.

In this study it can be seen that the topology of the hadronic final state in neutral current DIS events as seen in H1 is indeed sensitive to QCD models, and as such is able to discriminate between them.

5.2   Initial Event Selection

The identification of DIS events begins with the identification of the scattered electron in the backward electromagnetic calorimeter (BEMC). Initially, at the trigger stage, all events are accepted for which there is a cluster in the BEMC of greater than 4 GeV in coincidence with no veto from the time of flight (ToF) detector, but for the final event selection only electrons identified in the BEMC with an energy greater than 14 GeV are considered, which reduces the possibility of a pion in a photoproduction event being falsely identified as an electron in a DIS event to almost zero. The electron is identified with the highest energy BEMC cluster in the event and the backward proportional chamber (BPC) hit which is nearest to that cluster's centre of gravity. This hit must be within 15 cm of the centre of gravity, once projected onto the same plane, else the electron is considered not to be identified. It is further demanded that the centre of gravity of the cluster is not in one of the four triangular sections of the BEMC nearest the beam–pipe where the energy measurement is considered less precise, and that the distance of the BPC hit from the beam is between 18 and 60 cm. This demand ensures that the cluster is well contained in the BEMC.

After the above electron identification and selection, there remains a sample of

events each with a scattered electron of energy greater than 14 GeV as measured in the BEMC, scattered by an angle between about 5° and 25°, as measured in the BPC.

Two further conditions are enforced before proceeding to measure the hadronic energy. An event vertex must be found which lies within 50 cm of the nominal H1 vertex in z, that is along the beam–pipe, and there must exist at least one good track in the central jet chamber (CJC), where good means satisfying the following: having a vertex fit, a polar angle in the range from 20° to 160° with respect to the proton direction, a transverse momentum greater than 100 MeV, consisting of more than 10 hits, having an inverse radius measured to better than 50%, a χ^2 of less than 10 and a vertex z position within 10 cm of the event vertex.

5.3 Measuring the Hadronic Energy

The method of measuring the hadronic energy utilises the CJC and the three calorimeters : the liquid argon calorimeter, the BEMC and the tail catcher. In so doing it is possible to detect hadronic activity in the polar angular range from 4° to 176° with respect to the proton direction.

Firstly good tracks are identified, using the criteria above, but with the electron track, if it exists, being excluded. Each of these tracks defines a 4–vector momentum for a charged particle in the hadronic system in the approximation that the mass of that particle is negligible. The calorimeters are then used to pick up energy from neutral particles, from particles out of the angular range of good tracks, or from charged particles which were simply missed by the tracking reconstruction and so left no good track. To avoid double counting of energy for charged particles, that is to avoid taking both the track and calorimeter information for a particle, calorimeter cells behind a used track are ignored in the hadronic energy calculation. More precisely, for each used track there is a region of the calorimeter behind it which is masked off so that any energy found there is considered to be from the particle causing the track. The region is defined to be a cylinder around the extrapolated track of radius dependent on the calorimeter: 15 cm in the electromagnetic calorimeter (EMC) and the BEMC, 25 cm in the hadronic calorimeter (HAC) and 50 cm in the iron tail catcher. Cells corresponding to the scattered electron cluster

are also masked off. Where an energy deposit is found in a calorimeter cell which
is not masked off, a momentum 4-vector is formed, given by the amount of energy
measured in the calorimeter cell and the position of the cell with respect to the event
vertex.

Having followed the above procedure, there exists a set of momentum 4–vectors
representing the hadronic energy flow as seen in the detector, and also the previously
calculated scattered electron momentum 4–vector. These allow determination of the
kinematics of the event and a quantitative study of the hadronic system in the final
state.

5.4   Determination of Event Kinematics

In the following, k, l, q, and p are the momentum 4–vectors of the incoming and
scattered electron, the intermediate boson and the incoming proton respectively.
The four characteristic kinematic variables for describing deep inelastic scattering
events at HERA are $Q^2 \equiv -q.q$, the virtuality of the mediating boson, $y \equiv p.q/p.k$,
a scaling variable equivalent to the fraction of electron energy taken by the boson in
the proton rest frame, $x \equiv Q^2/2p.q$, the Bjorken scaling variable and $W^2 \equiv (q+p)^2$
the invariant mass squared of the final state hadronic system. For this study y and
Q^2 were measured directly from the observed final state and then x and W^2 were
calculated using the relations

$$x = Q^2/sy \tag{5.1}$$

where $s = (k+p)^2$ and

$$W^2 = Q^2 \frac{1-x}{x} + m_p^2 \tag{5.2}$$

where m_p is the proton mass.

Determination of y uses both the observed hadronic system and the scattered
electron, combining the energies, E, and momentum components in the incoming
proton direction, p_z, in the formula

$$y = \frac{\sum_{had}(E - p_z)}{\sum_{all}(E - p_z)} \tag{5.3}$$

where the sum in the numerator is over all 4–vectors associated with the observed
hadronic final state, and the sum in the denominator is over all particles observed

in the final state. Q^2 is determined from the scattered electron alone:

$$Q^2 = 4E_k E_l \cos^2(\theta_l/2) \tag{5.4}$$

where E_k, E_l, and θ_l are the energy of the incoming electron and the energy and polar angle of the outgoing electron respectively.

5.5   Final Event Selection

The initial event selection described above was based upon the scattered electron and the finding of an event vertex. Further events are rejected after the measurement of the hadronic system, to reduce possible background and produce a sample of events in which the hadronic system can be, and has been, reasonably measured.

So that the hadronic final state is reasonably contained in the H1 detector, only events for which W^2 is greater than 5000 GeV^2 are accepted, which essentially insists that the hadronic system arising from the struck parton of the proton is not largely undetected through having a small polar angle with respect to the proton direction.

Following this, two cuts are made to remove events where the hadronic system has clearly been badly measured, or perhaps the event has been wrongly identified as DIS, using the two identities

$$\sum_{all}(E - p_z) = 2E_k = 53.4 \ GeV \tag{5.5}$$

and

$$\left| \sum_{all} \vec{p_t} \right| = 0 \tag{5.6}$$

where $\vec{p_t}$ is the momentum vector projected onto a plane normal to the beam–pipe. Large deviations from these identities indicate that some significant error has been made in identifying and measuring the final state hadronic system or that the scattered electron has been falsely identified. The distributions of the expressions given in 5.5 and 5.6 are shown in figure 5.1 for data and Monte Carlo (MC), after all previously mentioned selections have been applied. The logarithmic scale should be noted.

Events are accepted if the conditions

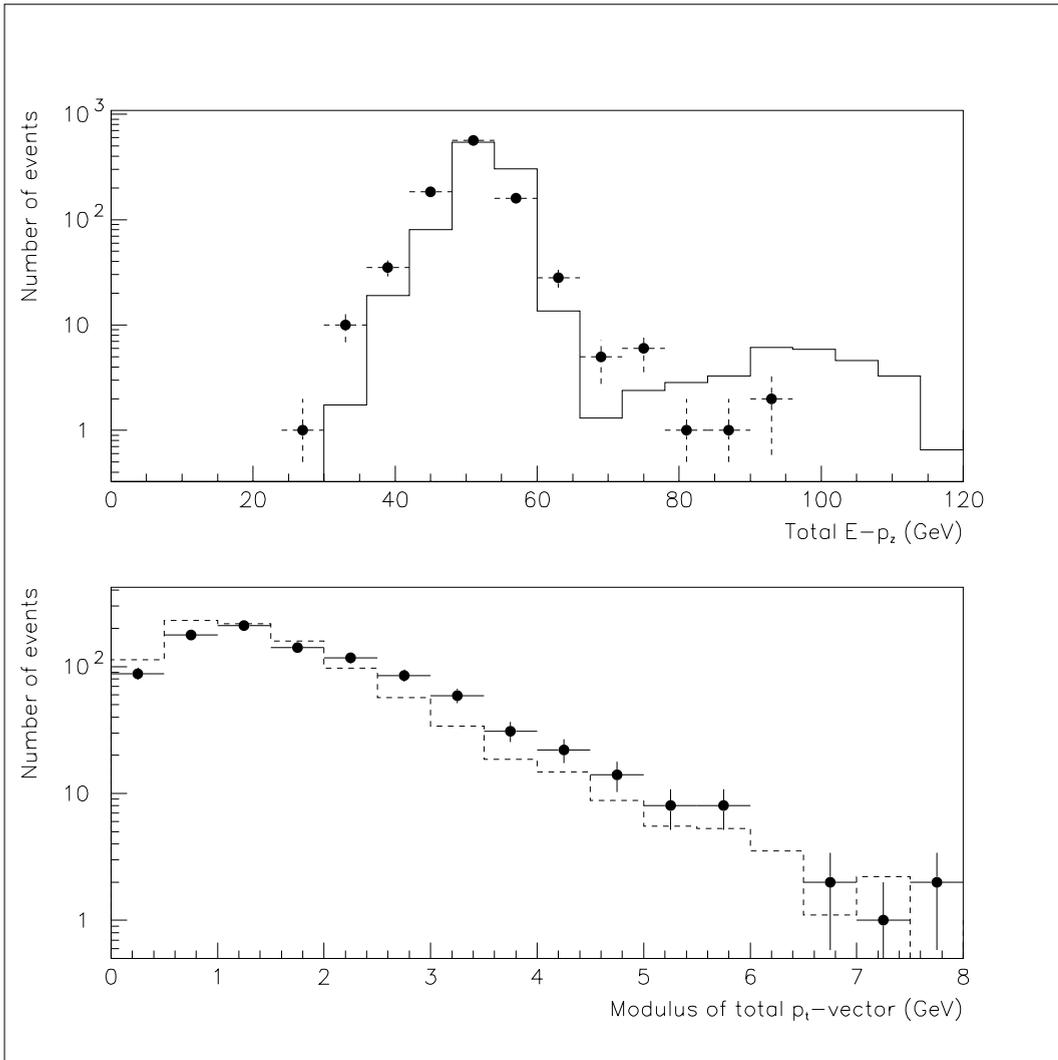$$35 \ GeV < \sum_{all}(E - p_z) < 65 \ GeV \tag{5.7}$$

Figure 5.1: Distributions of $\sum_{all}(E - p_z)$ (top) and $|\sum_{all} \vec{p_t}|$ (bottom) for H1 data (points) and MC (lines).

and

$$\left| \sum_{all} \vec{p}_t \right| < 3.5 \ GeV \tag{5.8}$$

are satisfied. In the lower plot of figure 5.1, the selection 5.7 has already been made.

There remains a class of events in the sample which is characterised by the lack of a proton remnant seen in the detector, and almost equivalently a low M^2, where M is the invariant mass of the hadronic final state observed in the detector. These events may validly be classed as DIS but seem to be diffractive in nature, in that a low mass colourless object from the proton appears to be participating in the hard interaction, and the proton itself remains intact or almost intact. Since the Monte Carlos used in this study do not attempt to model such an interaction, these events are removed from the sample. The removal of these events uses the fact that they populate a region of (M^2, W^2) phase–space which is empty in the MC samples, namely that of small M^2/W^2. Figure 5.2 shows how the events from the data sample are distributed in (M^2, W^2) phase–space, and the projection onto M^2/W^2. On the upper plot the cut made is indicated by the line $M^2/W^2 = 0.005$, and the lower plot shows the comparison with Monte Carlo which has no peak at low M, reflecting the fact that the Monte Carlo generator does not model this class of events.

The demand that $M^2/W^2 > 0.005$ removes about 7% of the data previously selected whilst removing only about 1% of MC generated events.

Figure 5.3 shows examples of a DIS selected event, and an event rejected as diffractive–type, as seen in the H1 detector in an r–z projection and an x–y projection, where r, z, x and y are in the standard H1 coordinate scheme explained in chapter 2.

The final data sample contains 812 events, the kinematics of which are represented in figure 5.4, which also indicates the kinematic bounds imposed by the requirements on the scattered electron energy and polar angle, and on the W^2 of the event.

5.6 Background in the Final Data Sample

Possible sources of background still remaining in this sample are photoproduction, beam–gas events, beam–wall events and remaining diffractive type events.
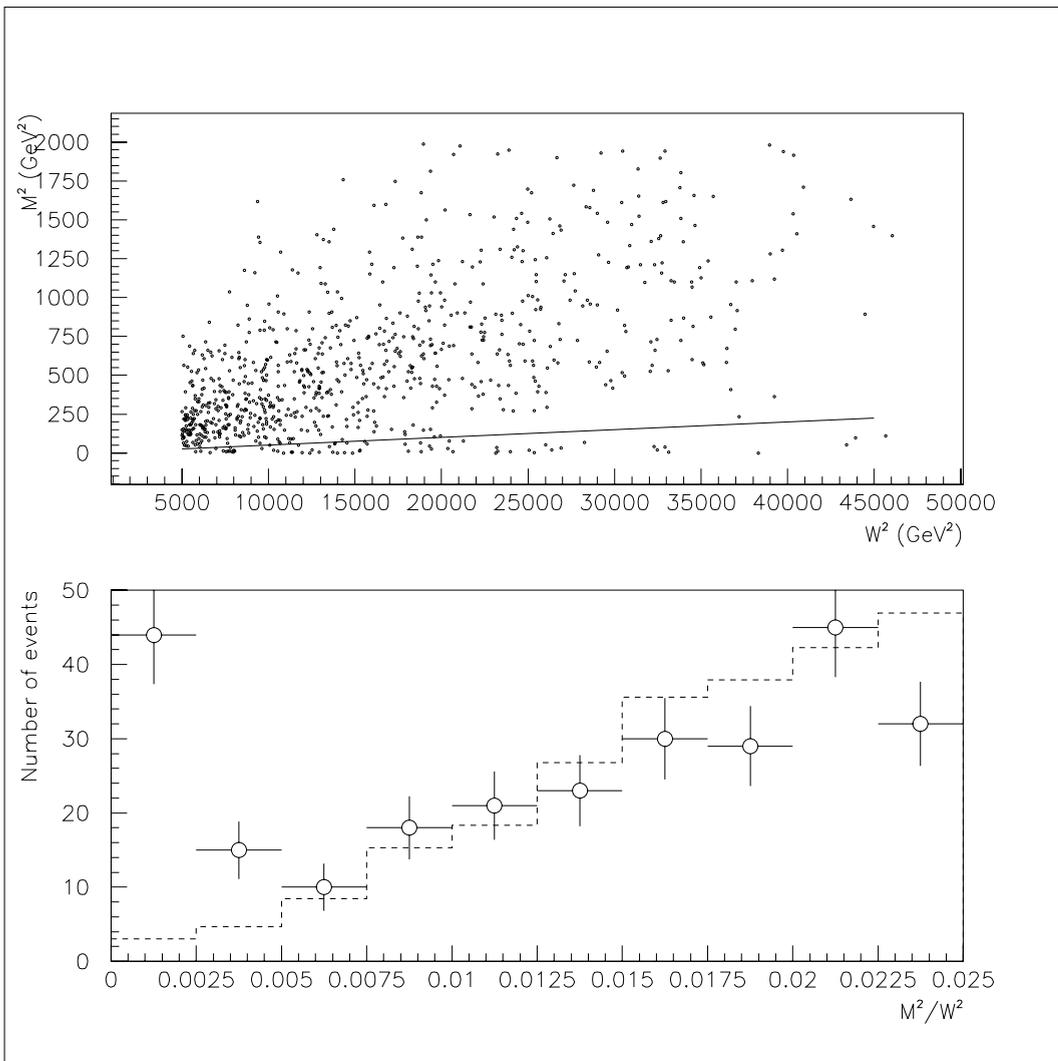
Figure 5.2: Upper plot: event M^2 and W^2 for data with diffractive–type cut at $M^2/W^2 = 0.005$ shown as line. Lower plot: M^2/W^2 for data (points) and MC (line).
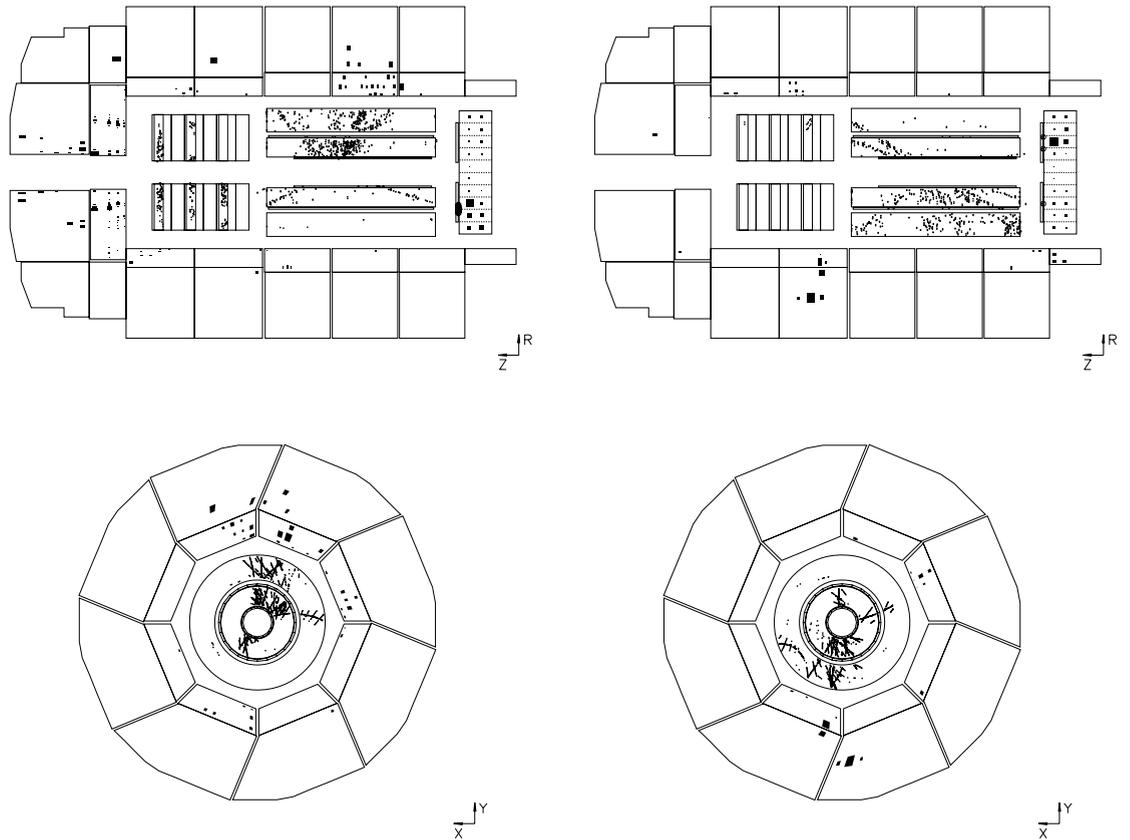
Figure 5.3: Left: selected DIS event with $x = 0.0026$ and $Q^2 = 46\ GeV^2$. Right: event rejected as diffractive–like, $x = 0.0024$, $Q^2 = 24\ GeV^2$. In particular, the proton remnant is clearly visible in the positive z part of the calorimeter at low angles to the incoming proton direction in the selected event, but is not seen in the rejected event.
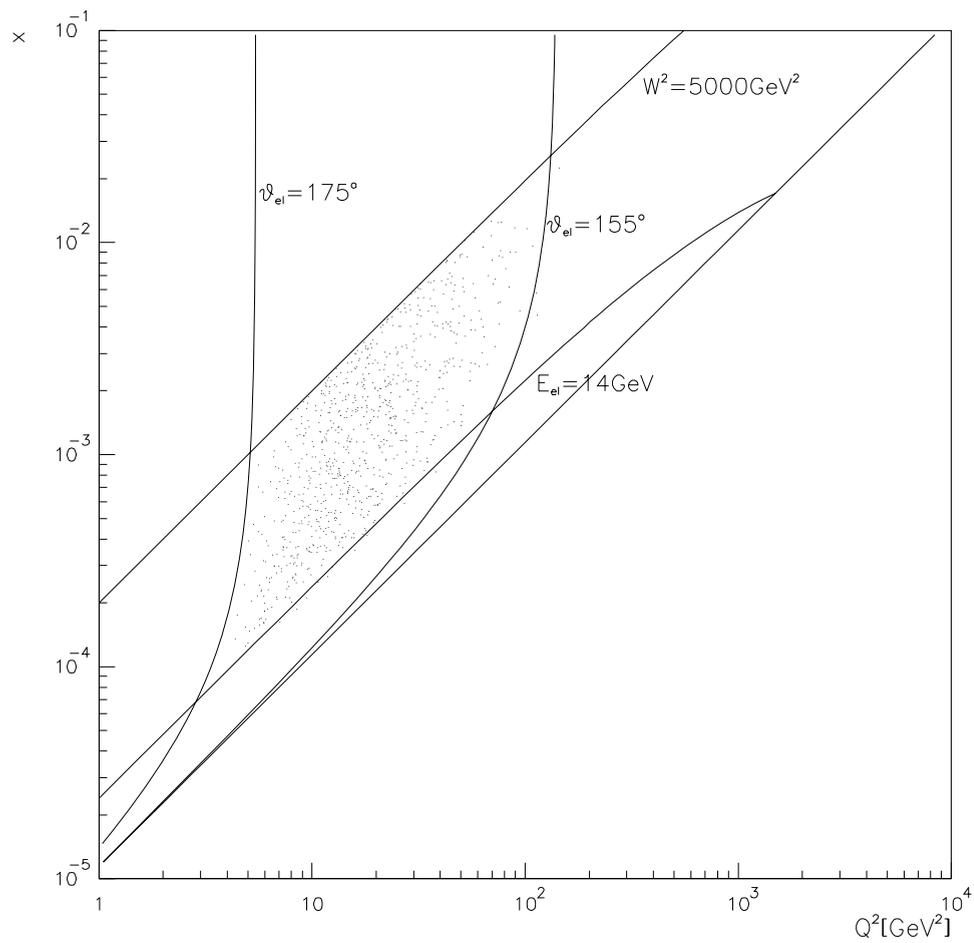
Figure 5.4: The final data sample of 812 events represented in (Q^2, x) phase–space.

The level of contamination due to photoproduction has been assessed using Monte Carlo generated photoproduction events corresponding to an integrated luminosity of about 48 nb^{-1}, that is about twice the luminosity which produced the actual data sample. These events are subject to the same event selection described above, and a total of 48 events remain after all cuts, suggesting that the final data sample contains about 24 photoproduction events, and less than 29 such events with 90% confidence. 29 events corresponds to about 3.5% of the sample.

Beam–gas and beam–wall events arise when an electron or proton from the beam collides with another particle in the beam–pipe but not associated with an electron or proton bunch, or collides with a particle of the material of the wall of the beam–pipe. Initially these events are suppressed by the demand of a vertex, a high energy scattered electron and a good track. Any remaining proton–gas or proton–wall events should be removed by the cut 5.7, leaving the small possibility of electron–gas and electron–wall events which should be removed by the cut meant to remove diffractive–type events, since there should be no forward energy deposited in the detector. An estimate of the maximum possible contamination can be gained by studying so–called pilot electron and proton bunches, which have no partner but pass through the vertex region without coming into contact with a colliding bunch. In the data taking period corresponding to this study, about one tenth of the electron current, and one tenth of the proton current, were carried by pilot bunches. However, in the event sample there are no events from pilot bunches. The strongest statistical statement that can be made given this result is that the data sample contains less than 3% of beam–gas events with 90% confidence, although it seems reasonable to assume that the actual level of contamination is much less than this. This pilot bunch method gives no indication of the amount of beam–wall background since it is probable that a bunch increases its transverse size in the presence of the colliding bunch. It would be surprising if the beam–wall background were as great as the beam–gas background.

The amount of remaining diffractive–type events is difficult to assess. A visual scan of selected events which have little energy in the very forward (proton) direction suggests that less than 2% of the data sample is of this type.

Possible additional background from cosmic muons and pile–up, that is where the remnants of some other interaction are superimposed upon the event arising from the true DIS interaction as a result of the high bunch crossing rate at HERA

(104 MHz), are certainly at a smaller than per cent level.

Combining the possible sources of background mentioned above leads to the conservative estimate that more than 93% of the final event sample is pure Deep Inelastic Scattering events.

5.7   Monte Carlo Generators

In order to use the experimental measurements to gain understanding of the underlying theory, the results are compared with expectations derived from Monte Carlo (MC) generators and detector simulation. The Monte Carlo generators themselves are detector independent, and contain the models for the interactions as far as the production of stable particles, defined to be particles with lifetime $\tau > 8$ *ns*. To determine the expected detector response for an event, the output from the Monte Carlo generator is processed through the program H1SIM [41], which is interfaced to GEANT [56], and contains an accurate description of the H1 detector and all associated materials, including the beam–pipe and beam–magnets in the vicinity of the detector. It is intended that this simulation of the detector should be accurate enough so that any differences seen between the experimental data and the generated data can be attributed to the failure of the Monte Carlo to properly model the physics processes. At any point in this chapter where experimental and generated data are compared, it can be assume that generated data is the simulated detector response to the Monte Carlo generated event.

Three MC generators were used in this study: LEPTO [57], DJANGO [58] and ARIADNE [59], in all of which the same model for the non–perturbative hadronization process was used, the Lund String Model as implemented in JETSET [60]. An introduction to Monte Carlo generators for DIS at HERA is given in [61, 62]. All the above use the same implementation of the underlying electroweak process except that DJANGO includes first order electroweak radiative corrections to the cross–section via an interface with HERACLES [63], but of particular interest are the models used to represent the perturbative QCD corrections which are different in each case and lead to different hadronic energy flow distributions in the final state. The 'parton shower' model, 'matrix element plus parton shower' model and the 'colour dipole' model are implemented in DJANGO, LEPTO and ARIADNE re-

spectively and are outlined below. A more comprehensive discussion is given in [64] and [54].

In the parton shower (PS) approach to describing QCD radiation, two parton cascades are formed. A parton cascade consists of several splittings of a single parton into two other partons, and thus has a tree–like structure. Time–like partons split into two further time–like partons in a so–called time–like parton shower, and space–like partons split into one space–like and one time–like parton in a so–called space–like parton shower. In either case a parton shower stops when all parton masses reach some threshold close to zero, typically where the modulus of the invariant mass squared is less than 1 GeV^2, and then partons undergo the non–perturbative process of hadronization. At the electroweak vertex, a space–like quark is excited to a time–like state by the mediating boson. The space–like quark is a result of a space–like cascade starting from an almost massless parton within the proton, and this space–like cascade is called the Initial State Parton Shower (ISPS). A time–like cascade, the Final State Parton Shower (FSPS), is initiated by the time–like quark coming from the vertex which becomes once more almost massless.

Parton cascades are parameterized by an evolution variable, t, which enters as the argument of α_s at each parton splitting, and also as the scale of the parton distributions in the proton which arise as factors at each splitting of the ISPS. In LEPTO this $t = M^2$, the invariant mass–squared of the splitting parton. The Altarelli–Parisi evolution equations are used to describe the probability at a particular t of a parton branching, and from these the Sudakov form factor is derived which gives the probability of a parton evolving from a scale $t = t_0$ to a scale $t = t_1$ without splitting (see [54]).

For practical reasons, parton showers in MC generators are always evolved away from the electroweak vertex, where the partons involved are maximally off–shell. This means evolving backwards 'into the proton' in the case of the ISPS. Considering the ISPS, and taking the scaling variable t to be the virtuality, Q^2, a cascade must be evolved that brings the parton at virtuality Q_1^2 at the electroweak vertex, down to a virtuality below the threshold Q_0^2. The value Q_1^2 is not known a priori, but must take some value between Q_0^2 (in the case of no branching in the ISPS) and Q_{max}^2. Q_{max}^2 is called the 'maximum virtuality scale' and can in principle be any function of the W^2 and Q^2 of the event. Once a maximum virtuality scale has been chosen, then the Sudakov form factor is enough to describe the shower evolution.

The FSPS works in the same way, evolving from the invariant mass squared of the quark at the electroweak vertex down to the threshold of hadronization. In both showers the evolution is strictly ordered in the variable t, equivalent to using the Leading Log Approximation (LLA). Gluon coherence effects in the time–like FSPS are not naturally included in this approach but are implemented by applying a strict angular ordering to the branchings : successive branchings have decreasing opening angles of the daughter partons.

Two shortcomings of the parton shower model are immediately apparent: the apparently unconstrained choice of the maximum virtuality scale, and the ignoring of interference inherent in the factorization into the initial state and final state parton showers. The choice of maximum virtuality scales directly determines the phase–space available for parton showers and so the amount of QCD radiation. Choosing either of the very different scales, Q^2 or W^2, is rather extreme and has been shown to greatly under–estimate and over–estimate the amount of energy in the hadronic final state respectively [65], favouring some intermediate scale, say WQ. This is the choice for the generator DJANGO used here, and is referred to as PS(WQ). Neglecting the interference terms between the initial and final state parton showers should be a good approximation for the softer, more collinear radiation, but not for harder and larger angle radiation. This leads to the Matrix Element plus Parton Shower (MEPS) model where first order α_s matrix elements are included explicitly, so intrinsically including interference terms for the hardest QCD radiation.

In the MEPS model the matrix elements for processes up to first order in α_s are calculated explicitly. These are shown in figure 5.5 without the cross–terms in the first order diagrams. To avoid the singular region of the matrix element, a lower limit is put on the invariant mass squared of any pair of particles appearing in the final state. This is implemented as a parameter y_{cut}, by default 0.015, such that $m_{ij}^2 > y_{cut}W^2$ for all pairs of particles (i,j), where W^2 is as defined above.

The choice of which of the three process of figure 5.5 occurred is made on a probabilistic basis using the matrix element calculation and the already chosen x and Q^2 of the event, as is the kinematic configuration of particles in the final state. Once this is done the kinematics of all the particles involved up to the first order QCD are determined, and the parton shower can be added to account for the softer emissions. The parton showers are exactly as in the PS model, but now the maximum virtuality scale is more constrained. In the case of interaction (a) of figure 5.5, there
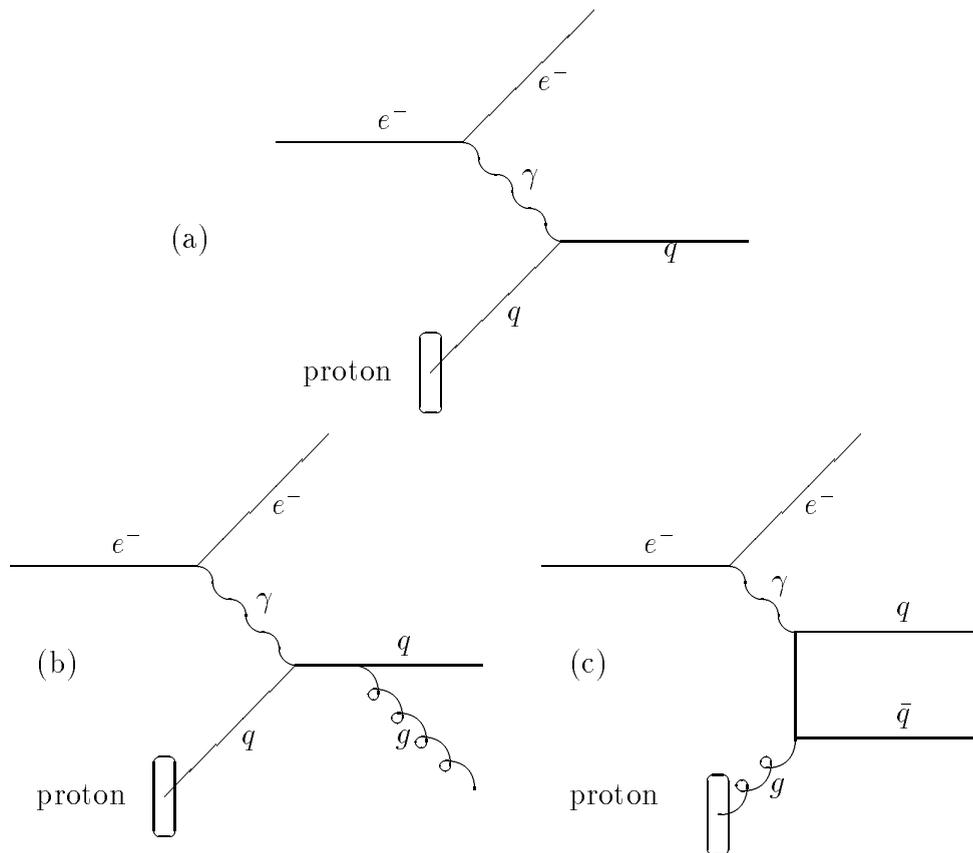
Figure 5.5: Feynman diagrams for the zeroth and first order QCD processes as implemented in the matrix element plus parton shower model. (a) zeroth order; (b) QCD Compton - this amplitude is added to the amplitude for a gluon radiated from the incoming quark; (c) Boson–gluon fusion - this amplitude is added to the cross term.

has been no radiation down to virtuality y_{cut}, and so this is chosen as the maximum virtuality for the parton shower. If (b) of (c) has occurred, there is still an ambiguity in the possible choice of maximum scales since it is not possible to say that, for instance in (b), the gluon was emitted from either the incoming or outgoing quark. This would allow calculation of the virtuality of the quark just before and after the vertex as wanted, but otherwise this calculation is not possible. In fact, the maximum virtuality scale for the final state parton shower is chosen as the invariant mass squared of the two outgoing partons. This is also the case for the initial state parton shower except in (b) where the highest choice is taken having calculated what the virtuality of the quark entering the boson vertex would be in the two cases of the gluon being radiated from the incoming and the outgoing quark.

The matrix element plus parton shower model has two advantages over the parton shower model: calculation of the exact first order matrix elements means that interference terms between the initial and final parton showers are, to some extent, accounted for, and also the maximum virtuality scale has been greatly constrained by the kinematics of the first order QCD process.

The third model, the Colour Dipole Model (CDM), assumes that gluons radiate from colour dipoles. A first gluon results from the colour dipole formed by the struck quark and the proton remnant, which leaves two remaining dipoles between the radiated gluon and the proton remnant and between the gluon and the quark. These in turn can radiate, and so on. The proton is treated as an extended object in one dimension, and its size suppresses small wavelength radiation. This is implemented in the Monte Carlo by only involving a fraction of the proton in the dipole emission of the gluon, where that fraction is inversely proportional to $p_\perp$, which is the evolution parameter for this model. This model does not contain the division into initial and final state radiation and also naturally takes into account the gluon coherence effects which were implemented by enforcing angular ordering in the parton shower. It does not, however, include properly the boson–gluon fusion interaction and this is included separately as a first order matrix element calculated exactly. Dipole radiation then proceeds starting from the two dipoles formed between the proton and quark and between the proton and anti–quark. It is also clear that the radiation is only regulated by W^2 and not Q^2, in fact the maximum $p_\perp^2$, equivalent to the maximum virtuality scale of the parton shower, is proportional to $W^{\frac{4}{3}}$.

In the following MEPS, PS(WQ) and CDM refer to the results from the corre-

sponding generators, LEPTO, DJANGO and ARIADNE.

5.8   Results

The distribution of hadronic energy flow in deep inelastic events is here represented by plots of the transverse energy as a function of pseudorapidity, η, and of azimuthal angle, ϕ. Pseudorapidity, η, is a measure of polar angle and is defined by

$$\eta = -\ln\tan\frac{\theta}{2} \tag{5.9}$$

where θ is the polar angle with respect to the incoming proton direction, so that positive η corresponds to the forward half of the detector. The azimuthal angle, ϕ, is measured with respect to the scattered electron, so that $\phi = 180°$ corresponds to the direction opposite to the scattered electron in the projection onto the coordinate x, y–plane in standard H1 coordinates.

Figure 5.6 shows the transverse energy flow as a function of η, comparing the experimental data with Monte Carlo expectations from the three models outlined above. In each case the proton structure function MRS–D0 has been assumed [66]. The errors shown on the data points are purely statistical, and are not shown for the MC data where the number of events in the sample is approximately six times more. It should be noted that each event contributes to each point on this plot.

The same Monte Carlo data samples are compared with the experimental data in figure 5.7 which shows the distribution of transverse energy as a function of azimuthal angle, ϕ. Once again each event contributes to each point and the errors shown are purely statistical.

5.9   Conclusions

Both figure 5.6 and figure 5.7 show that the Monte Carlo generated data does not reflect the experimental data. The most striking feature in the comparison is the lack of energy in the forward region of the detector predicted by the Monte Carlo generators with respect to the data. This discrepancy is beyond the bounds of possible error given by the description of the detector as implemented in the
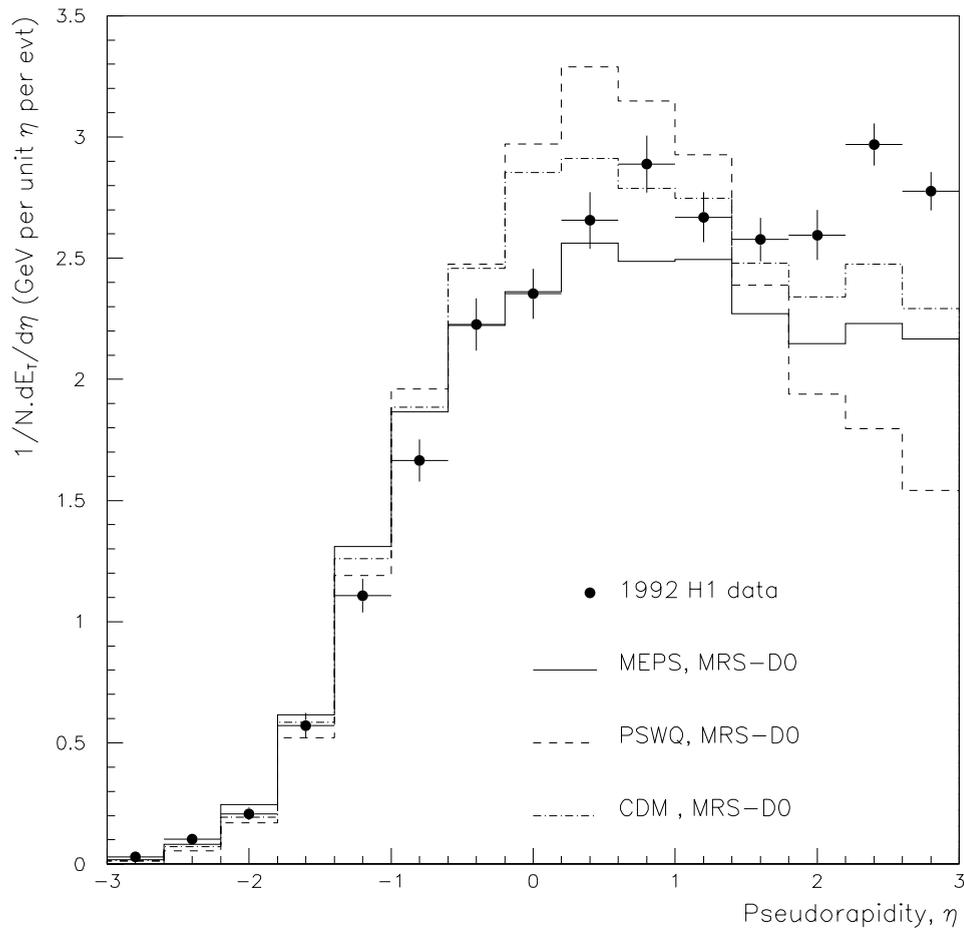
Figure 5.6: Transverse energy flow per unit pseudorapidity per event for H1 data and for Monte Carlo predictions based on three different models of perturbative QCD radiation in DIS events.
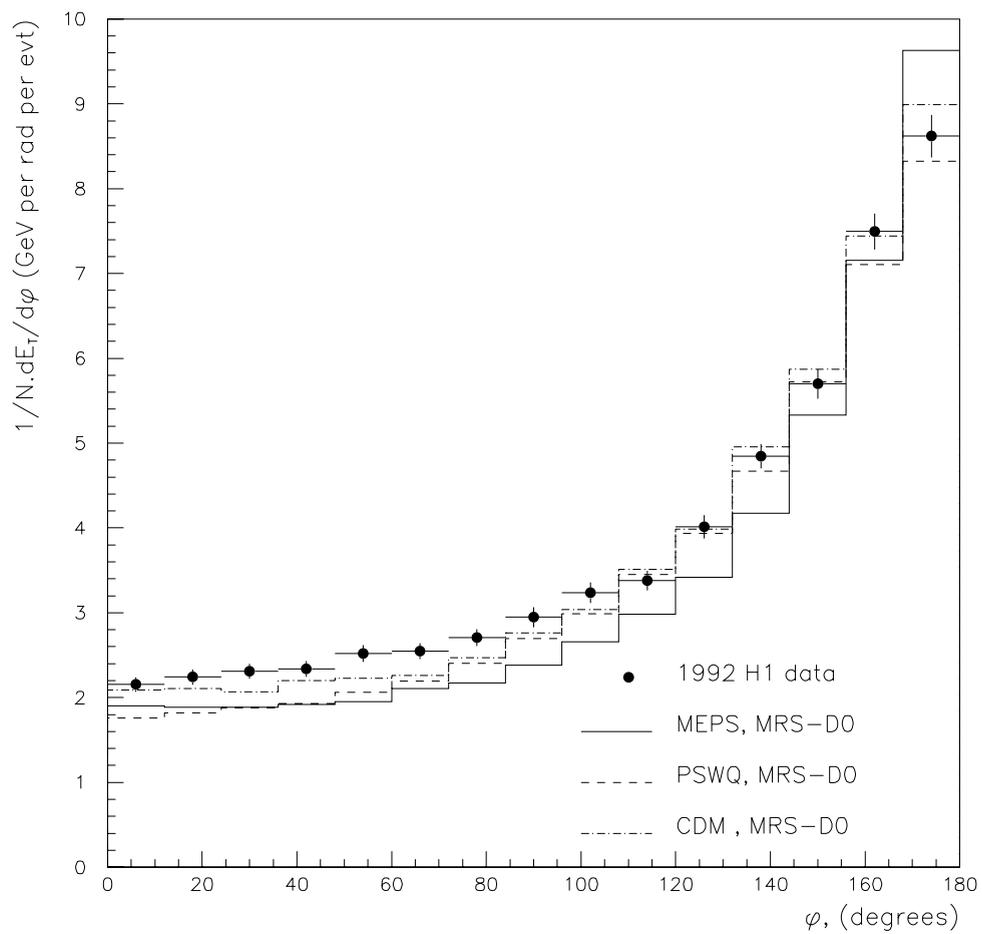
Figure 5.7: Transverse energy flow per radian in azimuth per event for H1 data and for Monte Carlo predictions based on three different models of perturbative QCD radiation in DIS events.

simulation, where the greatest uncertainty lies in the calibration of the liquid argon calorimeter, which is known to within 5% [30, 31], and the BEMC, which is known to within 2% [32]. Possible mis–calibration would produce a linear systematic shift and could not change the qualitative result.

The proton structure function affects both the kinematic distribution of events and the evolution of the initial state parton shower in the PS(WQ) and MEPS models. Figure 5.8 shows the distributions of events in the kinematic variables x, Q^2, y and W^2 for the same data samples used to produce figures 5.6 and 5.7, and they agree within the statistical errors. In figure 5.9 the transverse energy flow as a function of pseudorapidity is shown in the MEPS model for two different proton structure functions, MRS–D0 and MRS–D- [66], which have very different extrapolations to the low–x region from the region accessible by previous experiments. MRS–D- predicts a greater parton content of the proton at low–x so that more events would be expected with more backward hadronic energy, so producing a more backward biased energy flow as seen in figure 5.9. Taking these two structure functions as bounds in the new low–x kinematic domain, as suggested by the first measurements of F_2 [8] at HERA, it is clear that lack of knowledge about the proton structure function is not responsible for the inability of the Monte Carlo generators to produce the hadronic energy flow seen in the experiment.

The presence of background in the data sample at the level of less than 7% could not account for the discrepancy. Remaining diffractive events would anyway have the effect of artificially lowering the forward energy flow since these events have a rapidity gap between the proton and the rest of the hadronic final state. A generated sample of photoproduction events corresponding to about 48 nb^{-1} integrated luminosity was subjected to the selection procedure used in this study and the energy flow of the surviving events was plotted, and found not to be inconsistent with that for DIS events, within large statistical errors. A presence of photoproduction would not, therefore, produce a noticeable change in the measured hadronic energy flow.

The above considerations, and the fact that different models for QCD radiation in DIS events produce very different predictions for the distribution of hadronic energy in the final state despite using the same proton structure, detector description and fragmentation model, show that the results of this study are sensitive to perturbative QCD processes. Then figure 5.6 shows that parton shower with maximum virtuality scale WQ can be rejected as unable to produce the correct distribution. More insight
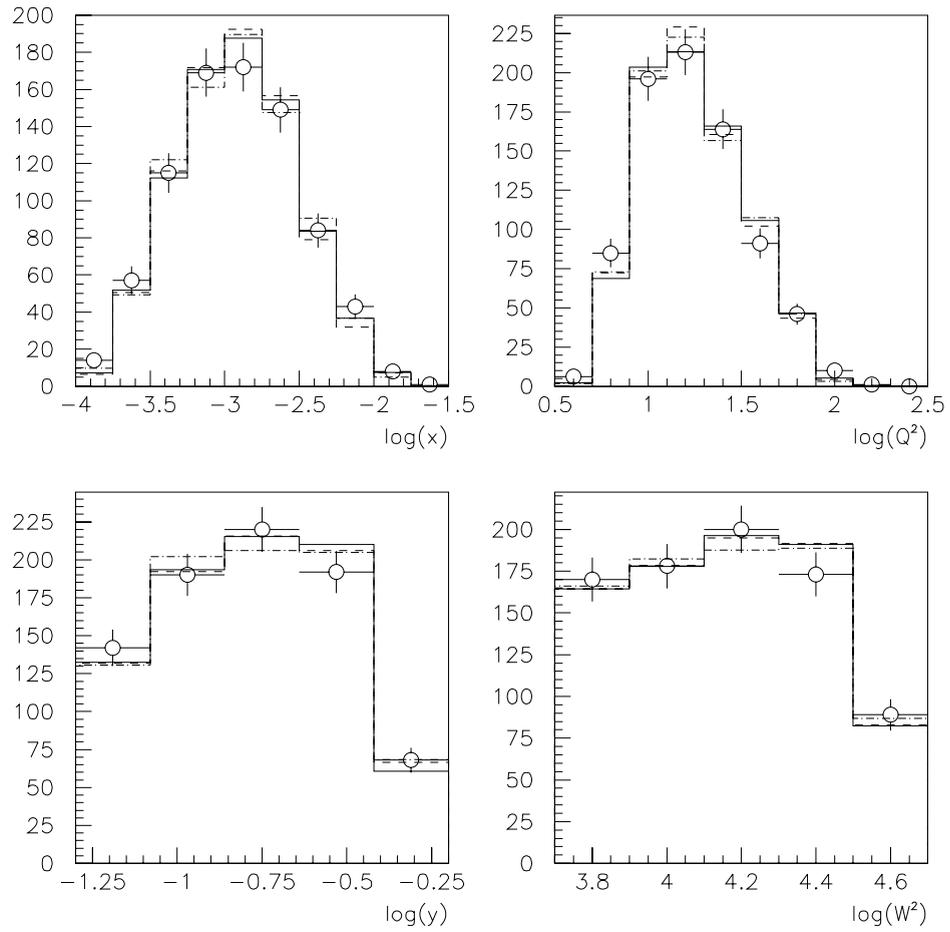
Figure 5.8: Distribution of events in the kinematic variables x, Q^2, y and W^2 for the event samples from H1 data (points), MEPS (full line), PS(WQ) (dashed line) and CDM (dot–dash line).
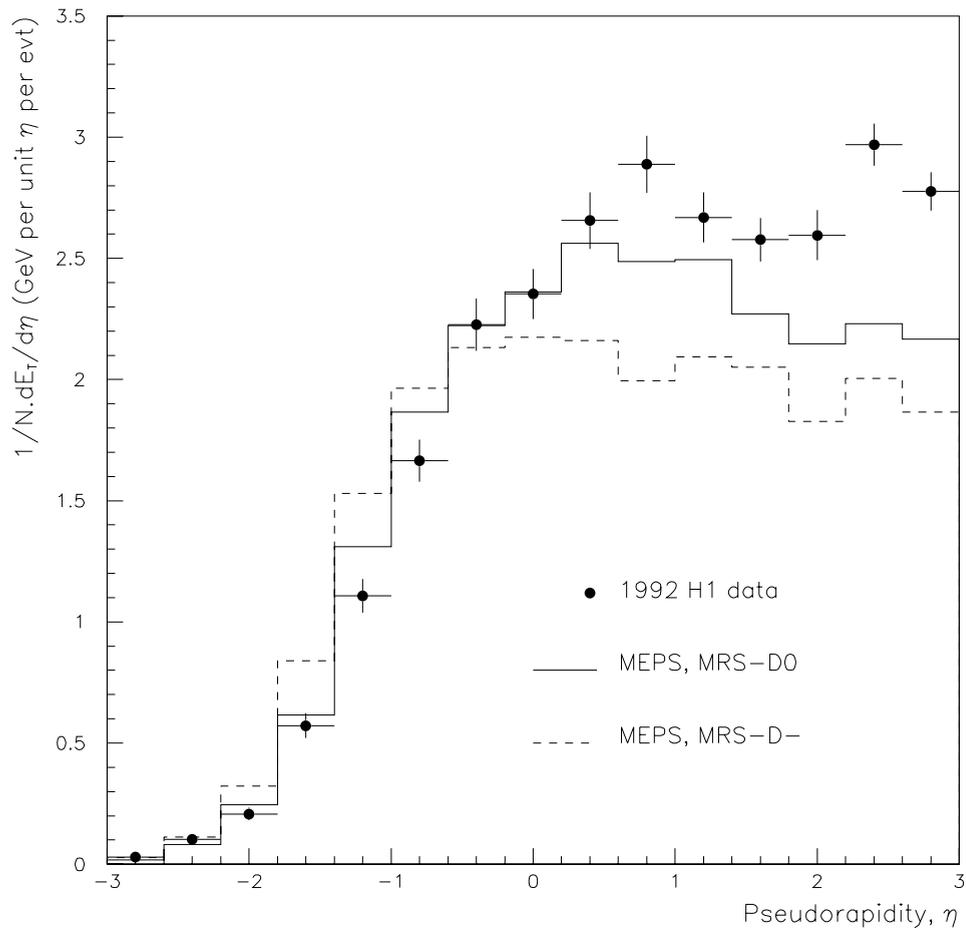
Figure 5.9: Transverse energy flow per unit pseudorapidity per event for experimental data, and for Monte Carlo generated data using the MEPS model and the two structure functions MRS–D0 and MRS–D-.

can be gained into the short–comings of the Colour Dipole Model and the Matrix Element plus Parton Shower model by referring to figure 5.10. Here the hadronic energy flow as a function of pseudorapidity is plotted in slices in the kinematic variable x. Whereas the MEPS model is clearly underestimating forward energy flow at low–x but is more successful at higher x, the performance of the CDM is independent of x and always underestimates the energy at $\eta > 2$.

In conclusion, the measurement of the hadronic energy flow in the final state as made in this study is sensitive to the model of perturbative QCD radiation implemented in Monte Carlo generators for deep inelastic scattering events. A model in which the QCD radiation is modelled by a parton shower with maximum virtuality scale WQ is shown not to be able to reproduce the experimental data. Adding matrix elements calculated exactly to first order in α_s to the parton showers produces a model that successfully reproduces the hadronic energy flow at higher x but underestimates the hadronic energy in the forward part of the detector for events with x less than about 10^{-3}. The Colour Dipole model is reasonably successful at all x but underestimates, to a lesser extent, the energy deposited in the very forward region of the detector.
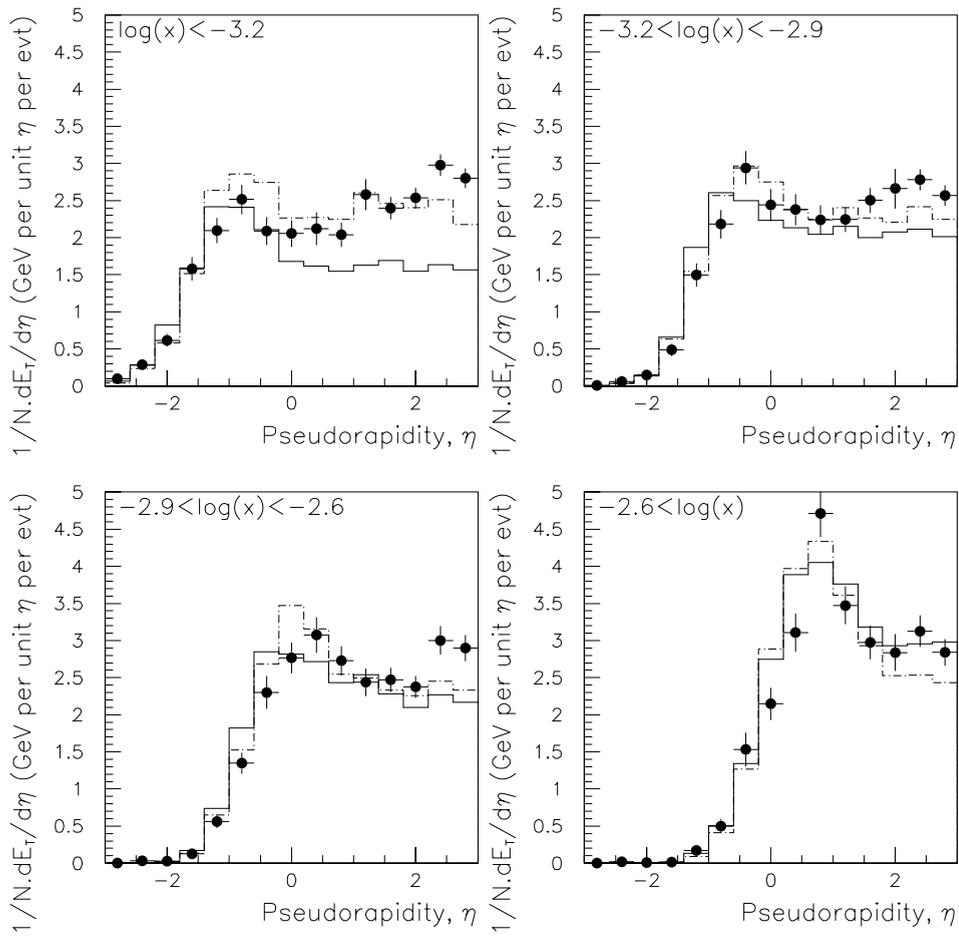
Figure 5.10: Transverse energy flow per unit pseudorapidity per event for four slices in x. H1 data in points, MEPS as solid lines, CDM as dot–dash lines.

Summary and Conclusion

Computer simulation of the forward muon detector has been used to test its potential performance. It has been shown that the detector can fulfill its intended rôle of identifying and providing a momentum measurement of muons in the momentum range from 5 GeV to 200 GeV. The accuracy with which the forward muon system is able to reconstruct the direction and momentum which a muon has on being produced in the vertex region at the centre of H1 has been assessed. It has been found that the resolution in the reconstruction of the direction is limited by the multiple scattering which a muon suffers in the H1 detector before reaching the forward muon system. The momentum measurement is limited in accuracy mainly by multiple scattering in the iron of the toroidal magnet of the forward muon system.

In particular, a study has been made of the importance of the forward muon detector in identifying J/ψ–mesons through their decay into a di–muon pair. A Monte Carlo program which models J/ψ production via the photon–gluon fusion mechanism was used for the study. In the resulting events the forward muon detector was found to be capable of identifying the tracks left by the muons in the forward tracker of H1. The forward muon system can therefore be expected to play an important part in physics studies at H1 which involve the identification of muons.

In a measurement of the hadronic energy distribution in the final state of deep inelastic scattering events, it has been shown that three Monte Carlo programs which try to model such events are unable to reproduce the experimental results. The discrepancy is, at least in part, due to the implementation of perturbative QCD corrections to the basic electroweak interaction.

Future measurements of the hadronic energy flow will be statistically more significant by virtue of the increase in the number of deep inelastic scattering events. However, to draw more meaningful conclusions, such a study will require better

understanding of the detector, of the background levels and of the proton structure function. This can be expected, and will reduce the systematic uncertainties in the results. Then the hadronic energy flow distribution will be a sensitive and rigorous test of the Monte Carlo implementations of QCD radiation.

References

[1] EMC, Nucl. Phys. B259, p.189 (1985).

[2] EMC, Nucl. Phys. B293, p.740 (1987).

[3] BCDMS Collaboration, Phys. Lett. B223, p.485 (1989).

[4] BCDMS Collaboration, Phys. Lett. B237, p.592 (1990).

[5] NMC, Phys. Lett. B294, p.120 (1992).

[6] NMC, Phys. Lett. B295, p.159 (1992).

[7] K.Charchula, M.Krawczyk, H.Abramowicz, A.Levy, *Some Topics in ep Scattering at HERA: I.Parton Distributions in the Nucleon.* DESY preprint, DESY 90–019, Hamburg (1990).

[8] H1 Collaboration, *Measurement of the Proton Structure Function $F_2(x,Q^2)$ in the Low x Region at HERA.* DESY preprint, DESY 93–117, Hamburg (1993).

[9] F.Halzen, A.Martin, *Quarks and Leptons: an Introductory Course in Modern Particle Physics.* John Wiley & Sons (1984).

[10] H.Küster, *Jets in Deep Inelastic Scattering at HERA.* H1 internal report, H1–5/93–295, DESY, Hamburg (1993).

[11] ZEUS Collaboration, *Observation of Events with a Large Rapidity Gap in Deep Inelastic Scattering at HERA.* DESY preprint, DESY 93–093, Hamburg (1993).

[12] J.Smith, *An Experimentalist's Guide to Photon Flux Calculations.* H1 internal report, H1–12/92–259, DESY, Hamburg (1992).

[13] G.Schuler, T.Sjöstrand, Phys. Lett. B300, p.169 (1993).

[14] G.Schuler, Proceedings of the HERA Workshop Vol.1 Hamburg, Oct 29–30, 1991 p.461. ed. W.Buchmüller, G.Ingelman.

[15] P.Bussey, *What HERA Tells Us About the Photon.* DESY preprint, DESY 93–071, Hamburg (1993).

[16] H1 Collaboration, Phys. Lett. B299, p.374 (1993).

[17] H1 Collaboration, Phys. Lett. B297, p.205 (1992).

[18] A.Ali, *Heavy Quark Physics in Photo– and Leptoproduction Processes at HERA and Lower Energies.* DESY preprint, DESY 93–105, Hamburg (1993).

[19] H.Jung, G.Schuler, J.Terron, Proceedings of the HERA Workshop Vol.2 Hamburg, Oct 29–30, 1991 p.712. ed. W.Buchmüller, G.Ingelman.

[20] G.Levman, Proceedings of the HERA Workshop Vol.1 Hamburg, Oct 29–30, 1991 p.623. ed. W.Buchmüller, G.Ingelman.

[21] R.van Woudenberg et al., Proceedings of the HERA Workshop Vol.2 Hamburg, Oct 29–30, 1991 p.739. ed. W.Buchmüller, G.Ingelman.

[22] J.Dainton, *Physics at HERA.* RAL preprint, RAL–90–038, Didcot (1990).

[23] C.Berger, T.Köhler, F.Raupach, K.Rosenbauer, Proceedings of the HERA Workshop Vol.2 Hamburg, Oct 29–30, 1991 p.1103. ed. W.Buchmüller, G.Ingelman.

[24] D.Feeken, *Die Myonsignatur von $b\bar{b}$–Ereignissen im H1–Detektor bei HERA.* Universität Hamburg (1991).

[25] F.Eisele, D.Wegener, *Muon background due to $\pi \rightarrow \mu\nu$ and $K \rightarrow \mu\nu$ decays.* H1 internal report, H1–4/85–15, DESY, Hamburg (1985).

[26] J.P.Sutton, *The H1 Forward Muon Spectrometer at the HERA Collider.* University of Manchester (1993).

[27] H1 Collaboration, *The H1 Detector at HERA.* DESY preprint, DESY 93–103, Hamburg (1993).

[28] M.Aguilar–Benitez et al., *Particle Properties Data Booklet.* (1992).

[29] D.Perkins, *Introduction to High Energy Physics.* Addison–Wesley (1987).

[30] H1 Calorimeter Group, *Results from Pion Calibration Runs for the H1 Liquid Argon Calorimeter and Comparisons with Simulations.* DESY preprint, DESY 93–047, Hamburg (1993).

[31] V.Shekelyan, *Simulation and Reconstruction in H1 Liquid Argon Calorimetry.* H1 note, H1–04/93–288, DESY, Hamburg (1993).

[32] M.Goldberg, *Energy Calibration and Resolution in BEMC.* H1 note, H1–05/93–292, DESY, Hamburg (1993).

[33] A.Mehta, *Investigation of the Drift Velocity of the Forward Muon Drift Chambers of the H1 Detector.* University of Manchester (1992).

[34] F.Sauli, *Principle of Operation of Multiwire Proportional and Drift Chambers.* CERN, Geneva (1977).

[35] W.Zimmerman et al., *A 16 Channel VME Flash ADC System (F1001–FADC).* H1 internal report, DESY, Hamburg (1989).

[36] J.Foster, *QTFMU The Forward Muon QT code.* University of Manchester.

[37] M.Schulz, P.Steffen, *Calibration with Testpulse data.* H1–tracking note 22, DESY, Hamburg (1990).

[38] A.Mehta, *Determination of Drift Velocity, Tzero and Resolution of the Forward Muon Spectrometer.* University of Manchester (1992).

[39] D.M.Gillespie, *A Radial Drift Chamber Combining Tracking and Transition Radiation Detection for Use in the H1 Experiment at HERA.* University of Liverpool (1992).

[40] C.D.Hilton, *Investigations Concerning the Forward Muon Drift Chambers of the H1 Detector at HERA.* University of Manchester (1991).

[41] J.Meyer (Ed.), *Guide to Simulation Program H1SIM.* DESY Central IBM, 'HERA01.H1SIM', Hamburg (1991).

[42] R.Brun et al., *GEANT 3 User's Guide.* CERN DD/EE/84–1 (1987, revised 1992).

[43] I.Duerdoth, *A Pointing Theorem for Tracks in a Cylindrically Symmetric Magnetic Field.* University of Manchester, MAN/HEP/91/03 (1991).

[44] A.Martin, C.–K.Ng, W.Stirling, Phys. Lett. B191, p.200 (1987).

[45] S.Tkaczyk, W.Stirling, D.Saxon, Proceedings of the HERA Workshop Vol.1
      Hamburg, Oct 12–14, 1987 p.265. ed. R.D.Peccei.

[46] G.Schuler, J.Terron, *Elastic and Diffractive Photoproduction of J/ψ Mesons.*
      DESY preprint, DESY 92–017, Hamburg (1992).

[47] Z.Kunszt, W.Stirling, Phys. Lett. B217, p.563 (1989).

[48] M.Drees, C.Kim, *Associate J/ψ + γ Production: a Clean Probe of Gluon Den-
      sities.* DESY preprint, DESY 91–085, Hamburg (1991).

[49] E.Berger, D.Jones, Phys. Rev. D23, p.1521 (1981).

[50] H.Jung, D.Krücker, C.Greub, D.Wyler, *Relativistic Corrections to Photopro-
      duction of J/ψ.* DESY preprint, DESY 93–072, Hamburg (1993).

[51] P.Landshoff, *Soft Hadronic Physics.* CERN preprint, CERN–TH.6277/91,
      Geneva (1991).

[52] S.Baranov, N.Zotov, *On the Diffractive Dissociation in Hard Scattering Model
      at HERA Energies.* DESY preprint, DESY 92–145, Hamburg (1992).

[53] H.Jung, Proceedings of the HERA Workshop Vol.3 Hamburg, Oct 29–30, 1991
      p.1488. ed. W.Buchmüller, G.Ingelman.

[54] M.Bengtsson, G.Ingelman, T.Sjöstrand, Proceedings of the HERA Workshop
      Vol.1 Hamburg, Oct 12–14, 1987 p.149. ed. R.D.Peccei.

[55] G.Ingelman, K.Meier, B.R.Webber, Proceedings of the HERA Workshop Vol.1
      Hamburg, Oct 29–30, 1991 p.255. ed. W.Buchmüller, G.Ingelman.

[56] R.Brun et al., *GEANT Detector Simulation Program.* CERN Program Library.

[57] G.Ingelman, Proceedings of the HERA Workshop Vol.3 Hamburg, Oct 29–30,
      1991 p.1366. ed. W.Buchmüller, G.Ingelman.

[58] G.A.Schuler, H.Spiesberger, Proceedings of the HERA Workshop Vol.3 Ham-
      burg, Oct 29–30, 1991 p.1419. ed. W.Buchmüller, G.Ingelman.

[59] L.Lönnblad, Proceedings of the HERA Workshop Vol.3 Hamburg, Oct 29–30,
      1991 p.1440. ed. W.Buchmüller, G.Ingelman.

[60] T.Sjöstrand, Computer Physics Commun. 39, p.347 (1986);
T.Sjöstrand, M.Bengtsson, Computer Physics Commun. 43, p.367 (1987).

[61] G.Grindhammer, Proceedings of the HERA Workshop Vol.3 Hamburg, Oct 29–30, 1991 p.1153. ed. W.Buchmüller, G.Ingelman.

[62] N.Magnussen et al., Proceedings of the HERA Workshop Vol.3 Hamburg, Oct 29–30, 1991 p.1167. ed. W.Buchmüller, G.Ingelman.

[63] A.Kwiatkowski, H.Spiesberger, H.–J.Möhring, Proceedings of the HERA Workshop Vol.3 Hamburg, Oct 29–30, 1991 p.1294. ed. W.Buchmüller, G.Ingelman.

[64] N.Brook, G.Ingelman, L.Lönnblad, Proceedings of the HERA Workshop Vol.3 Hamburg, Oct 29–30, 1991 p.275. ed. W.Buchmüller, G.Ingelman.

[65] H1 Collaboration, Phys. Lett. B298, p.469 (1993).

[66] A.D.Martin, R.G.Roberts, W.J.Stirling, *New Information on Parton Distributions.* Phys. Rev. D47, p.867 (1993).

Acknowledgements

The work associated with producing this thesis has only been possible through the endeavours of many people, most of whom are not mentioned here by name. Amongst these I am particularly grateful to my colleagues in Manchester, Birmingham, Lund and at DESY who have worked with me and the forward muon detector.

During my three years as a PhD student I have had the benefit of the unfailingly helpful support of my supervisor, Mike Ibbotson, for which I am very grateful.

J.Paul Sutton deserves particular thanks for some fine pioneering work in the field of producing theses about the forward muon detector, and for many other things besides.

Also Phill Biddulph for help and support beyond the call of duty and more generally for doing a great deal of excellent work towards getting the forward muon detector working at DESY.

Many thanks also to the following people who have all directly helped me to produce this thesis: Roland Martin, Andy Mehta, Gareth Noyes, Hywel Phillips, Lee West, Nick Brook, Julian Phillips, Alison Wright, Joe Foster, Ray Thompson and undoubtedly others.

Finally I would like to mark my appreciation of the friendship and general helpfulness of many persons who have been in Hamburg over the last two years, and regret not mentioning their names explicitly for fear of leaving some out.